ISSN 1883 - 0315

TOHOKU UNIVERSITY

IMR KINKEN Research Highlights 2023

Institute for Materials Research, Tohoku University

Research

KINKEN

Research Highlights

2023

Institute for Materials Research, Tohoku University

KINKEN Research Highlights 2023

Contents

Research Centers

International Collaborative Research

Research

Preface

Dear Colleagues,

We are delighted to present “KINKEN Research Highlights 2023,” our annual report that showcases research findings from the Institute for Materials Research (IMR) at Tohoku University for the past year. KINKEN is the abbreviation for “Kinzoku Zairyo Kenkyusho,” the Japanese name for IMR, and is well known in the materials science community.

IMR has a rich history spanning over one hundred years since its establishment in 1916. Initially, the focus was on iron and steel materials, but as times changed and research progressed, its scope expanded to include the fundamentals and applications of various materials, including non-metals such as semiconductors and ceramics. With these changes, the institute changed its name from the Research Institute for Iron, Steel and Other Metals (RIISOM) to the current one in 1987. Ever since Dr. Honda, its first director, invented the world’s first artificial permanent magnet called KS magnet steel, the institute has developed many new materials for practical use, including Sendust alloy, SiC fibers, and soft magnetic amorphous alloys, and has also conducted not only fundamental research, but also pioneering research in the search for new materials and the elucidation of physical properties such as magnetism and superconductivity. It has become a global center in materials science.

A key feature of IMR is its fusion of fundamental and applied research, as well as science and engineering fields. Additionally, the institute stands out for its joint research with both domestic and international researchers, utilizing world-class facilities for experiments (high-energy irradiation testing, high magnetic fields, supercomputers, etc.) and for the creation and evaluation of new materials. In

Takahiko Sasaki

Director Prof. Takahiko Sasaki

2018, IMR was certified as the International Joint Usage/Research Center for Materials Science, known as “Global Institute for Materials Research Tohoku” (GIMRT). IMR is committed to further promoting research and fostering the next generation of researchers, and putting into practice Dr. Honda’s words, “Industry is the training ground of academics,” it also focuses on the likes of industry-academia collaboration and engineer training.

IMR is committed to creating a sustainable society, a goal shared by the global community. Its materials science research has the power not only to solve issues but also to positively transform society. The institute is dedicated to supporting the international competitiveness of Japan’s materials manufacturing and engaging in global endeavors to create academic intellectual property shared by humankind. IMR will continue to work on innovative materials science research that will bring about a paradigm shift with a long-term vision and contribute to developing human resources who will lead the future.

We hope KINKEN Research Highlights will provide insights into our recent research activities and help encourage worldwide collaboration with IMR. We value your continued support and welcome any suggestions.

Infrastructural Materials

IMR KINKEN Research Highlights 2023

Strengthening of Low-Carbon Steel using Nano-Sized Vanadium Carbide in Ferrite and Tempered Martensite

Precipitation behaviors and strengthening mechanisms of a vanadium-microalloyed low-carbon steel, produced by either tempering of martensite or ferrite transformation with interphase precipitation, were comparatively studied. The yield strength of the steel can be satisfactorily explained by cumulatively considering various strengthening factors, whereas the higher yield strength of tempered martensite can be attributed to its finer grain size and higher dislocation density, although its dispersion of precipitates is relatively coarser.

The precipitation of nano-sized alloy carbides, which induces a large strengthening effect in commercial ferritic steels microalloyed with strong carbide-forming elements can be generally obtained using two different methods. One is precipitation by aging in the conventional quenching and tempering process, which corresponds to the secondary hardening of martensitic structures [1]. The other method is the newly developed interphase precipitation technique, which occurs as a result of nucleation at the migrating interphase boundary during ferrite transformation [2]. In this study, the microstructural features in a vanadium-microalloyed low-carbon steel produced by these two treatments were systematically investigated via various characterization techniques, to directly compare their effects on the precipitation behaviors and strengthening mechanisms under the same conditions.

An Fe-0.1C-0.4V-1.5Mn (mass%) alloy was used. After austenitization at 1473 K for 0.6 ks, the alloy was either quenched and tempered, or isothermally transformed at 923 K multiple times for up to 172.8 ks. Subsequently, electron backscattering diffraction, X-ray diffraction, and a three-dimensional atom probe were used to quantify the grain size, dislocation density, and dispersion of VC, respectively, whereas tensile tests were performed to analyze the mechanical properties of the specimens.

Figure 1 shows the dispersion of VC formed in ferrite and tempered martensite [3]. The number density of VC gradually increases initially and later decreases because of the coarsening of tempered martensite, whereas the size of VC simply becomes larger with holding time. The dispersion of VC is always relatively coarser in tempered martensite than in ferrite. Conversely, the grain size of tempered martensite was confirmed to be relatively finer in tempered martensite than in ferrite, with a higher dislocation density.

Figure 2 shows the strength contributions of various microstructural features in ferrite and tempered martensite, which were calculated using the proposed models [3]. The experimentally measured yield strength shows good agreement with the summation of various factors. When compared to ferrite, tempered martensite is characterized by its higher yield strength, which can be attributed to its finer grain size and higher dislocation density, regardless of its coarser dispersion of VC precipitates.

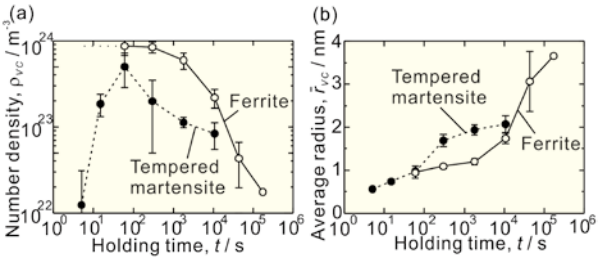

Fig. 1 Variation in (a) number density and (b) average radius of VC in steel with isothermal holding time at 923 K [3].

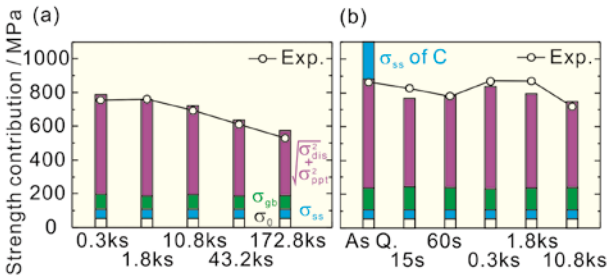

Fig. 2 Contributions of various factors to yield strength of steel that is (a) isothermally transformed and (b) tempered at 923 K [3]. σ_0: friction stress; σ_{ss}: solid solution strengthening; σ_{gb}: grain boundary strengthening; σ_{ppt}: precipitation strengthening; σ_{dis}: dislocation strengthening.

References

[1] Y.-J. Zhang, C. Zhao, M. Sato, G. Miyamoto, and T. Furuhara, ISIJ Int. **61**, 1641 (2021).

[2] Y.-J. Zhang, E. Chandiran, H.-K. Dong, N. Kamikawa, G. Miyamoto, and T. Furuhara, JOM **73**, 3214 (2021).

[3] Y.-J. Zhang, M. Sato, G. Miyamoto, and T. Furuhara, ISIJ Int. **62**, 2016 (2022).

Yongjie Zhang (Microstructure Design of Structural Metallic Materials Research Laboratory)
E-mail: yongjie.zhang.a5@tohoku.ac.jp
URL: http://www.st-mat.imr.tohoku.ac.jp/en/index.html

Computational Design of High-Functional and Durable Materials Based on Molecular Dynamics Simulation

The computational design of high-functional and durable materials requires a deep understanding of multi-physics phenomena including chemical reactions, friction, stress, and fluid dynamics. We applied our developed molecular-dynamics-based multi-physics simulator to revealing the multi-physics phenomena, contributing materials design in fields related to mechanical engineering, such as automobile engineering, aerospace instrumentation, and tribology.

High-functional and highly durable materials are required in a wide variety of research fields such as power plants, electronics, and tribology for achieving a safe and secure society. Recently, researchers have recognized that a deep understanding of multi-physics phenomena including chemical reactions, friction, stress, and fluid dynamics is required for the computational design of materials. However, the traditional simulation methods such as first-principles calculation and fluid mechanics cannot simulate the above multi-physics phenomena. Thus, we applied our developed multi-physics simulator based on methods such as coarse-grained molecular dynamics (CGMD) and reactive molecular dynamics method. for pioneering next-generation material design [1-3].

Slide-ring (SR) gels with slidable cross-linked cyclic molecules exhibit considerably higher fracture toughness than conventional fixed cross-link (FC) gels. To elucidate the reason for the higher fracture toughness of SR gels, we conducted tensile strain simulations of FC and SR gels using the CGMD method (Fig. 1) [1]. In FC gels, the axis chains break under a low strain because the FCs constrain the polymer chain, resulting in stress concentration at the axis chains (Fig. 1c). Conversely, in SR gels, the axis chains did not break until a high strain, and the cross-linked cyclic molecules can slide without stress concentration (Fig. 1d). This is because the cross-linked and un-cross-linked cyclic molecules slide on the axis chains and are stacked around the chain-ends, resulting in stress concentration around the chain-ends without breaking of the axis chain.

We conducted a reactive molecular dynamics sliding simulation of an amorphous SiC (a-SiC)/water system to elucidate the formation mechanism of a self-forming tribolayer, which contributes to the low friction of the SiC/water interface [2]. We determined that the selective oxidation of the a-SiC substrate by water generates colloidal silica, which forms a layer of silica hydrate on the a-SiC substrate (Fig. 2). Moreover, carbon atoms remained at the a-SiC surface and formed a C-rich layer. Then, further friction caused the

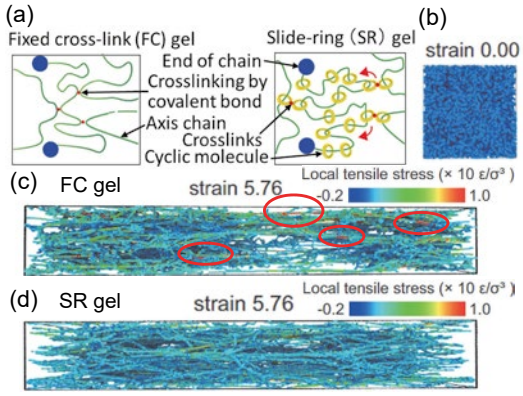

Fig. 1 (a) Schematic of fixed cross-link (FC) and slide-ring (SR) gels. (b) Initial structure of tensile strain simulation of FC gels. Local mechanical stress distribution of (c) FC and (d) SR gels at strain of 5.76.

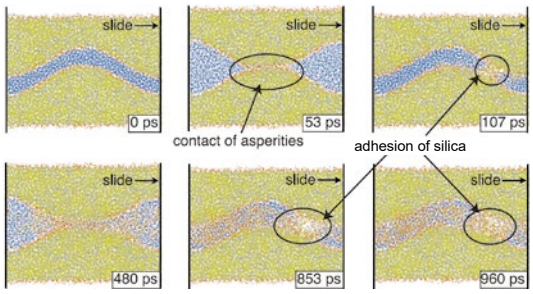

Fig. 2 Time variation of the interface structure between a-SiC/water system during sliding simulation.

C-rich layer to change to an amorphous carbon layer that exhibits low friction. We propose that colloidal silica, silica hydrate, and amorphous carbon can act as tribolayers to reduce friction.

References

[1] S. Uehara, Y. Wang, Y. Ootani, N. Ozawa, and M. Kubo, Macromolecules **55**, 1946 (2022).

[2] Y. Ootani, J. Xu, F. Nakamura, M. Kawaura, S. Uehara, K. Kanda, Y. Wang, N. Ozawa, K. Adachi, and M. Kubo, J. Phys. Chem. C **126**, 2728 (2022).

[3] Q. Chen, J. Xu, Y. Su, S. Uehara, S. Bai, Y. Wang, Y. Ootani, N. Ozawa, and M. Kubo, Comput. Mater. Sci. **208**, 111354 (2022).

Momoji Kubo (Materials Design by Computer Simulation Research Laboratory)
E-mail: momoji@tohoku.ac.jp
URL: https://www.simulation.imr.tohoku.ac.jp/eng/index.html

Irradiation-Induced Growth and Precipitation of Metallic Materials Elucidated via In Situ Electron Microscopy

Atomic-scale thermal structural changes strongly influence the mechanical properties in metallic alloys. We visualized two atomic-scale behaviors in metals based on in situ heating transmission electron microscopy: a hardening mechanism by asymmetric growth of Frank loops in Al–Cu alloy and precipitation behavior with vacancy diffusion in Fe–Si ordered alloy.

The in situ heating transmission electron microscopy (TEM) is a promising method for elucidating atomic-scale behaviors, which combines the effects of electron irradiation-induced displacement and heating-induced diffusion enhancement. Here, we show the advanced dynamical observation results of a solid-solution alloy, Al–Cu [1], and an ordered alloy, Fe–Si [2], as fundamental metallic materials.

Figures 1(a), (b) show high-resolution TEM images that were captured at room temperature at 540 and 640 s after starting electron irradiation. Before observation, the initial defects that generated during sample preparation were removed by annealing in vacuum. The electron-beam-irradiation-induced vacancies were clustered on the {111} plane and formed flank-type dislocation loops. The flank loops expanded by climbing the edge dislocations (red) to <112> with increasing irradiation duration, while the edge dislocations (blue) were stabilized. These stable dislocations are connected to a strain contrast area, which would be a cluster of Cu atoms (Guinier–Preston (G.P.) zone), as shown in Fig. 1 (c). The molecular dynamics simulation suggests that this behavior is caused by the repulsive interactions between G.P. zones and edge dislocations.

Figures 2(a), (b) show the TEM images of Fe–15 at% Si $D0_3$-ordered alloy at 650 °C captured from a movie file at 0 and 670 s. The nano-sized α-Fe particles, which is unpredictable on the phase diagram, were precipitated and grew in the ordered matrix phase, as shown by the energy dispersive X-ray spectroscopy results (Figs. 2 (c)-(e)). This phenomenon occurs because of the selective formation of irradiation vacancies at Si sites and the difference in diffusion rates of Fe and Si atoms in the $D0_3$ structure. Conversely, an Fe-depleted layer was formed around α-Fe particles of approximately 20 nm diameter, suggesting that the diffusion of Fe atoms and further coarsening of the particles were suppressed.

Our results indicate that in situ TEM enables the dynamic visualization of microstructural changes, as well as the elucidation of mechanisms related to the appearance of functions and microstructural formation in practical materials by using TEM environments such as high vacuum and electron irradiation, and using thin samples.

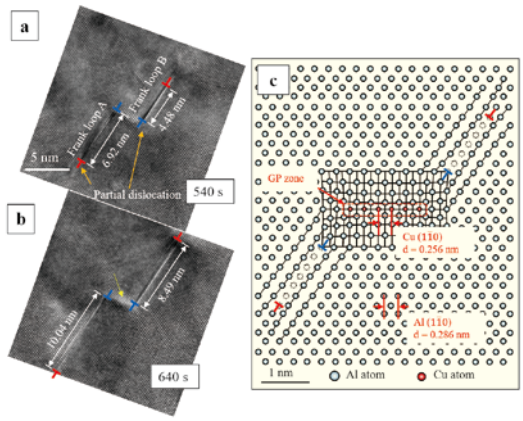

Fig. 1 In situ high-resolution transmission electron microscopy (TEM) images of the Al–1.7Cu captured at 540 s (a), 640 s (b); the arrow shows the strain contrast. (c) Schematic diagram showing coherent Cu precipitate sandwiched between two Frank loops.

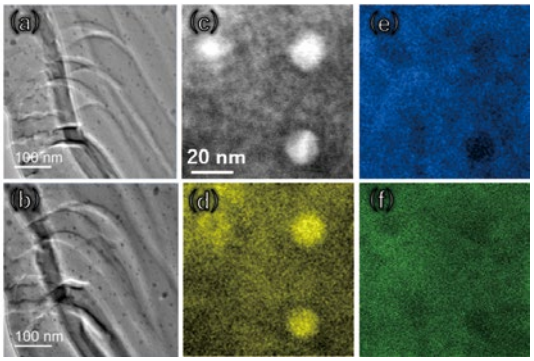

Fig. 2 TEM images for 0 s (a) and 670 s (b) after reaching a temperature of 650 °C. (c) shows magnified high-angle annular dark field –scanning TEM image of the α-Fe nanoparticles, and elemental maps of Fe (d), Si (e), and O (f).

References

[1] J. Chen, K. Yoshida, T. Suzudo, Y. Shimada, K. Inoue, T. J. Konno, and Y. Nagai, Mater. Trans. **63**, 468 (2022).

[2] Y. Shimada, Y. Ikeda, K. Yoshida, M. Sato, J. Chen, Y. Du, K. Inoue, R. Maaß, Y. Nagai, and T. J. Konno, J Appl. Phys. **131**, 16902 (2022).

Yusuke Shimada (Irradiation Effects in Nuclear and Their Related Materials Research Laboratory)
E-mail: yusuke.shimada.e1@tohoku.ac.jp
URL: http://www.imr.tohoku.ac.jp/en/about/divisions-and-centers/research-division/11.html

Real-Time 2D Imaging of Atomic-State Hydrogen in Metals Using an Ultrasensitive Hydrogenochromic Sensor

Hydrogen atoms cause the embrittlement of metals. Observing the behavior of hydrogen in metals is crucial for elucidating the embrittlement mechanisms; however, hydrogen imaging remains challenging. In this study, we succeeded in real-time hydrogen visualization using a polymeric sensor. The sensor paves the way for analyzing hydrogen behaviors in metals owing to its high sensitivity and high spatial resolution.

A small amount of hydrogen in metallic materials causes plasticity-induced cracking, which is called hydrogen embrittlement. Observing the hydrogen behaviors in metals is essential for elucidating the mechanism of hydrogen embrittlement. However, real-time visualization of the large area of the hydrogen distribution in metals remains a challenge.

Thus, we developed a hydrogenochromic sensor consisting of Ni interfacial layer and polyaniline (PANI) layers and successfully visualized the atomic-state hydrogen in a metal with high sensitivity. Figure 1 shows the hydrogen visualization mechanism using a hydrogenochromic sensor [1]. Hydrogen atoms are introduced from an aqueous solution and diffuse to the other side of the specimen where PANI is polymerized on the Ni interfacial layer. As the color of PANI changes because of the hydrogenation reaction, the hydrogen distribution can be visualized based on the color distribution of PANI. Figure 2 shows the optical images of the hydrogenochromic sensor before and after hydrogen charging. The green area inside the O-ring is PANI. The left and right halves of the polyaniline layer correspond to the hydrogen-uncharged and hydrogen-charged areas, respectively. Figure 2(b) shows that only the hydrogen-charged area was brightened, indicating that PANI changed its color owing to the reaction with the atomic-state hydrogen that permeated through the metal. The hydrogenochromic reaction of PANI was observed to be catalyzed by the Ni interfacial layer, achieving a high sensitivity of 2 mol·m^{-2} and high spatial resolution of hundreds of micrometers [1].

In an actual environment, hydrogen embrittlement is often caused by a significantly small amount of hydrogen introduced by corrosion. Therefore, the mechanism of hydrogen entry under corrosion conditions is of significant interest. The hydrogenochromic sensor was then applied to visualize the hydrogen distribution in an Fe sheet under corrosion conditions. Owing to its high sensitivity to hydrogen, the sensor visualized the corrosion-induced hydrogen entry and elucidated the correlation between the hydrogen entry and corrosion reactions [2,3]. This hydrogenochromic sensor paves the way for analyzing hydrogen behaviors in metals, leading to the development of next-generation materials for the hydrogen energy society.

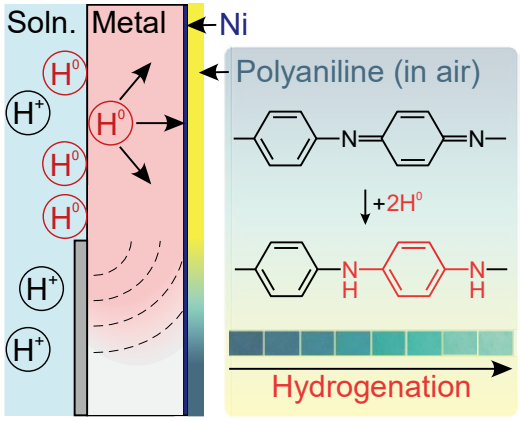

Fig. 1 Mechanism of visualizing hydrogen in a metal using the hydrogenochromic sensor [1].

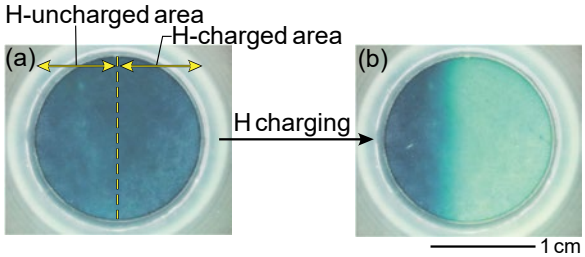

Fig. 2 Optical images of the hydrogenochromic sensor (a) before and after (b) 1 h of hydrogen charging [1].

References

[1] H. Kakinuma, S. Ajito, T. Hojo, M. Koyama, and E. Akiyama, Adv. Mater. Interfaces **9**, 2101984 (2022).

[2] H. Kakinuma, S. Ajito, T. Hojo, M. Koyama, S. Hiromoto, and E. Akiyama, Corros. Sci. **206**, 110534 (2022).

[3] H. Kakinuma, S. Ajito, T. Hojo, M. Koyama, S. Hiromoto, and E. Akiyama, Int. J. Hydrog. Energy **47**, 38468 (2022).

Hiroshi Kakinuma (Environmentally Robust Materials Research Laboratory)
E-mail: hiroshi.kakinuma.a1@tohoku.ac.jp
URL: http://akiyamaimr-e.amebaownd.com/

Ball-Milling Treatment of Gas-Atomized Ti–48Al–2Cr–2Nb Powder and its Effect on Preventing Smoking in Powder Bed Fusion Electron Beam Melting Process

Smoking, which is an unexpected and explosive splashing of powder caused by electrostatic force, is one of the main obstacles hindering the stability and applicability of the powder bed fusion electron beam technology. In this study, the effectiveness of mechanical ball milling to suppress powder bed smoke in the powder bed fusion electron beam melting process was investigated using gas-atomized Ti–48Al–2Cr–2Nb powder.

Powder bed fusion electron beam (PBF-EB), an additive manufacturing technique, has attracted considerable attention in the fabrication of non-weldable or brittle materials because of its high preheating temperature. However, unexpected powder scattering (also known as "smoking") during the preheating process degrades the stability of the manufacturing process and applicability of the PBF-EB technique. The aim of this study was to investigate the effectiveness of mechanical stimulation using ball milling on smoke suppression in the PBF-EB process.

The gas-atomized Ti–48Al–2Cr–2Nb powder was mechanically ball-milled under rotating speeds of approximately 200–400 rpm for 30 min in an air atmosphere. The electrical resistance of the powders was characterized using a tailored impedance spectroscopy system.

Figure 1 shows the schematic of the PBF-EB process with the corresponding equivalent electrical circuit (EEC). In the EEC model for the PBF-EB process, I_{EB} is the amount of irradiated electron beam current, R_{PB} and C_{PB} are parallel resistors and capacitors of the powder bed, respectively, R_{BP} is the resistor of the base plate, and I_G is the discharged current through the ground wire. Thus, the electrical charging of the powder bed is predominantly affected by the resistor–capacitor circuit in the PBF-EB process (Fig. 1c). In the impedance test using the powder, the EEC of the powder bed was predominantly affected by their oxide film states (Fig. 1d).

Figure 2 shows the Nyquist plots of the virgin and ball-milled powders. A semi-circular arc shape indicating capacitive response was observed for BM200, BM250, and BM300 powders. The diameter of the semicircle (R_{oxide}) decreased with the increasing milling velocities up to 300 rpm (Fig. 2a). Conversely, the imaginary component of the impedance in the BM350 and BM400 powders changed to a positive value associated with the inductive response (Fig. 2b). This result indicates that the capacitive oxide film of raw powder was transitioned to a conductive oxide film via mechanical stimulation using the ball-milling process with a velocity above 350 rpm [1,2].

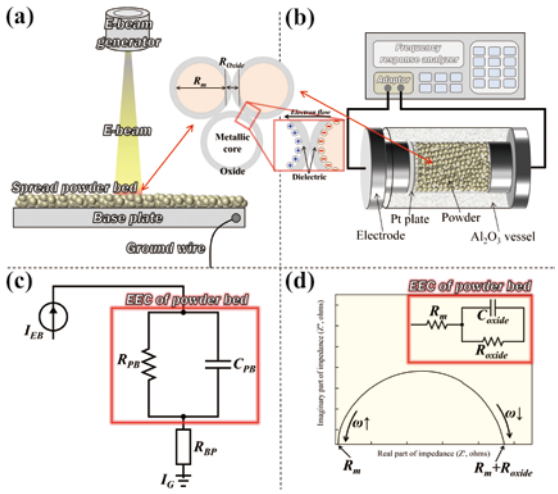

Fig. 1 Schematics of the (a) powder bed fusion electron beam (PBF-EB) process, (b) impedance spectroscopy, (c) equivalent electrical circuit (EEC) in the PBF-EB process, and (d) Nyquist plot with the corresponding EEC.

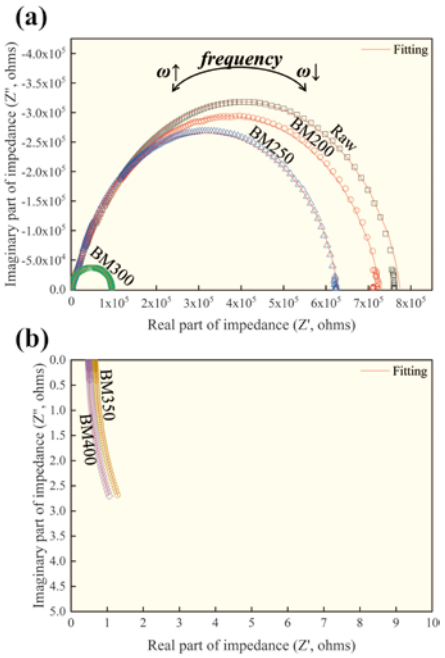

Fig. 2 Nyquist plots of Ti–48Al–2Cr–2Nb powders; (a) gas-atomized, BM200, BM250, BM300, (b) BM350, BM400. (Number indicates ball-milling velocity)

References

[1] S. Yim, K. Aoyagi, K. Yamanaka, and A. Chiba, Addit. Manuf. **51**, 102634 (2022).

[2] S. Yim, K. Aoyagi, and A. Chiba, J. Mater. Sci. Technol. **137**, 36 (2023).

Kenta Aoyagi (Deformation Processing Research Laboratory)
E-mail: kenta.aoyagi.e7@tohoku.ac.jp
URL: http://www.chibalab.imr.tohoku.ac.jp/english/index.html

Functionality in N-Doped Ti Under Visible-Light Irradiation

Ti and its alloys are frequently used as biomaterials because of their good biocompatibility and high corrosion resistance. In this study, N-doped TiO_2 was formed on a Ti substrate, and the antibacterial activity and reactive oxygen species resulting from the visible-light-induced photocatalytic activity of the N-doped TiO_2 were investigated.

TiO_2 is often formed on Ti surfaces, which is responsible for the biocompatibility of Ti. Numerous studies have reported that anatase-type TiO_2 exhibits high photocatalytic activity; when it is irradiated with ultraviolet light, it reacts with the surrounding water or O_2 and generates reactive oxygen species (ROS). Moreover, hydrogen peroxide and OH radicals are known to be generated as ROS on TiO_2 photocatalysts. N-doped TiO_2 also exhibits visible-light-induced photocatalytic activity. When N-doped TiO_2 is subjected to NaOH and hot water and heated in an atmosphere of gaseous NH_3, visible-light-induced antimicrobial activity and biocalcification ability were exhibited [1, 2]. Conversely, as a related study, we also conducted a study on TiNbSn alloys using sodium tartrate electrolyte [3].

The objective of this study was to investigate the antibacterial activity and the OH radicals generated via visible-light-induced photocatalytic activity on N-doped TiO_2.

To prepare the N-doped TiO_2, we polished commercial-grade pure Ti (cp Ti) plates and soaked them in NaOH solution and hot water. These plates were subsequently heated at 500 °C for 3 h under an NH_3 gas atmosphere in a tubular electric furnace. Measurements confirmed the formation of OH radicals. Electron-spin resonance spectroscopy was performed to quantify the OH radicals.

Figure 1 shows the measurement results of OH radicals generated by the visible-light photocatalysis of cp Ti or N-doped TiO_2 (500 °C, 3 h). The results show that more OH radicals were generated with an N-doped TiO_2 plate than with a cp Ti plate.

Figure 2 shows the antibacterial effect of the samples of cp Ti and N-doped TiO_2 plates (500°C, 3 h) on *Escherichia coli* (*E. coli*) and *Staphylococcus aureus* (*S. aureus*) when subjected to visible-light irradiation. The count of viable *E. coli* and *S. aureus* were lower after the treatment in the N-doped TiO_2 plate than in the cp Ti plate.

The N-doped TiO_2 prepared in this study exhibited photocatalytic activity under visible-light irradiation, and OH radicals were generated. The results suggested that ROS generated by the photocatalytic reaction contributed to the antibacterial effects.

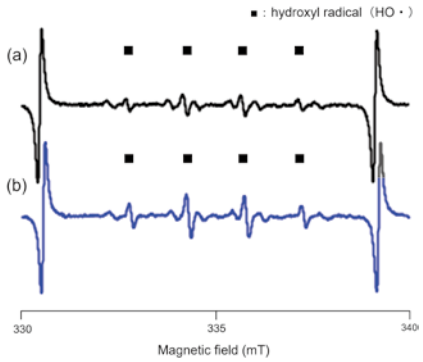

Fig. 1 Electron-spin resonance spectra under visible-light irradiation of (a) a pure Ti plate (cp Ti) and (b) an N-doped Ti plate (500 °C, 3 h).

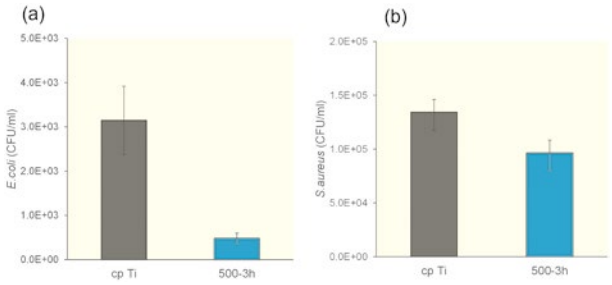

Fig. 2 Viable count of (a) *Escherichia coli* and (b) *Staphylococcus aureus* on cp Ti and N-doped TiO_2 plates (500 °C, 3 h) under visible-light irradiation (mean ± standard deviation; n = 3).

References

[1] M. Kawashita, N. Endo, T. Watanabe, T. Miyazaki, M. Furuya, K. Yokota, Y. Abiko, H. Kanetaka, and N. Takahashi, Colloids and Surf. B **145**, 285 (2016).

[2] M. Iwatsu, H. Kanetaka, T. Mokudai, T. Ogawa, M. Kawashita, and K. Sasaki, J. Biomed. Mater. Res Part B Appl. Biomater. **108(2)**, 451 (2020).

[3] H. Kurishima, Y. Mori, K. Ishii, H. Inoue, T. Mokudai, S. Fujimori, E. Itoi, S. Hanada, N. Masahashi, and T. Aizawa, Front Bioeng. Biotechnol. **10**, 883335 (2022).

Takayuki Mokudai (Design & Engineering by Joint Inverse Innovation for Materials Architecture)
E-mail: tmokudai@tohoku.ac.jp
Hidemi Kato (Project Leader of Design & Engineering by Joint Inverse Innovation for Materials Architecture)
E-mail: hidemi.kato.b7@tohoku.ac.jp
URL: http://www.imr.tohoku.ac.jp/en/about/divisions-and-centers/research-division/29.html

Recent Trend of Fostering PhD Candidates and Doctoral Degree Holders in Computational Materials Science: Wave of Integration of Data Science and Materials Science

Professional development Consortium for Computational Materials Scientists (PCoMS) supports young researchers in computational materials science (CMS) to develop a broader view and extensive knowledge of interdisciplinary areas in the fields of materials science (MS), condensed matter physics, molecular science, and materials design. This article introduces a recent activity carried out by a key member of PCoMS, Prof. Terada, who analyzed the trend of human resource development in PhD candidates and doctoral degree holders in CMS in Japan.

In recent years, the demand for researchers who are knowledgeable in computational materials science (CMS), materials informatics, and materials integration, connecting CMS and experimental materials science with data science, has increased. As proposed by the Cross-ministerial Strategic Innovation Promotion Program (SIP), materials integration is a comprehensive materials technology tool that aims to support materials research and development by utilizing the results of materials science (MS) and integrating all the scientific technologies, including theory, experiment, analysis, simulation, and databases.

We have analyzed the titles of approximately 150,000 doctoral dissertations in engineering and science (ES) from domestic universities over the past 50 years and approximately 10,000 doctoral dissertations of several research-oriented universities in the USA and Europe over the past 20–50 years as references. Using text data mining techniques with keywords in the field of CMS, we estimated the number of doctoral degree holders in the CMS and related fields, including materials informatics and materials integration.

Our recent research revealed how materials informatics and materials integration in Japan has encouraged doctoral degree holders in ES.

In the 1990s, many doctoral dissertations in fundamental fields such as statistical physics had titles that included the keywords of the basic research methods of data science, such as "neural network" and "inverse problem". Subsequently, after the 2000s, although the variety of keywords from other data science fields in the title increased, the number of dissertations including basic concepts such as “neural network” and “inverse problem” decreased, and the number of dissertations related to data science did not increase in the MS field. In the 2010s, the number of doctoral degrees related to data science in MS increased, and the variety of keywords in dissertation titles diversified further.

Our previous analysis about CMS has shown that when a new research method is proposed, new material is produced, or major research breakthrough is made, the number of doctoral dissertations containing the related new keywords increases rapidly for some time immediately after the breakthrough. However, as the new concepts related to the keywords become more generalized, they tended to disappear from the doctoral dissertation titles.

In this case, after the basic research methods and concepts such as “neural network” and “inverse problems" were actively studied, they became extremely common, and frequency of these terms in doctoral dissertation topics had increased for a period of time, then decreased; subsequently, various related keywords appeared. Our analysis suggested the spread of materials informatics in MS from the 1990s to 2010s; however, the ratio of the number of doctoral degree holders in materials informatics and materials integration to the total number of doctoral degree holders in ES was still small until 2020.

Our updated analysis results also suggest that the ratio of the number of doctoral degree holders in CMS to that in “science and engineering” in Japan had been continuously increasing until 2020, up to nearly 10%. However, it is still lesser than that of research-oriented universities in the USA and Europe. Moreover, the proportion of the doctoral degree holders in CMS who oriented toward fundamental research in Japan is also lesser than that in the USA and Europe.

These results suggest that the number of the doctoral degree holders in CMS, materials informatics, and materials integration in Japan needs to increase [1].

References

[1] Y. Terada, “Recent change of number of doctors in computational materials science: Widespread of integration of data science, experimentation, and computation”, JIM Annual Fall Meeting 2022, Sep 22, 2022.

Yayoi Terada (Professional development Consortium for Computational Materials Scientists)
E-mail: yayoi.terada.b8@tohoku.ac.jp
Momoji Kubo (Project Leader of Professional development Consortium for Computational Materials Scientists)
URL: http://pcoms.imr.tohoku.ac.jp/index_e.html

Energy-Related Materials

IMR KINKEN Research Highlights 2023

In Situ Observation of Solidification and Subsequent Evolution of Ni–Si Eutectic Alloys

Eutectic growth in Ni–Si alloy with a composition of $Ni_{44}Si_{56}$ was observed in situ during directional solidification. Two intermetallic phases, NiSi and $NiSi_2$, were formed behind the solidifying interface, generating a lamellar, regular eutectic. Continuous migration of the phase boundaries occurred during the cooling stage, resulting in a myriad patterns.

Eutectic solidification creates various morphologies with multiple phases. A regular eutectic system exhibits the simultaneous, side-by-side solidification of two non-faceted solid phases from a melt, resulting in a lamellar microstructure of two participating phases. Eutectic growth can produce in situ composite materials, and a better knowledge of its growth kinetics allows scientists and engineers to explain the myriad patterns in the as-grown materials. In this study, we performed in situ observations of the formation and subsequent evolution of eutectic alloys solidified from a binary melt of Ni and Si.

Experiments were performed using an in situ observation system that consisted of an optical microscope and a crystal growth furnace. Two graphite heaters were installed in the furnace for controlling the temperature gradient during solidification. High-purity Si (Czochralski-grown wafer) and Ni (6N) raw materials were melted in a quartz crucible under an argon atmosphere and the temperature gradient was tuned to achieve directional solidification. The composition of Ni and Si in this study was 44:56 at%, which is the lowest eutectic point in the Ni–Si binary system. Without seeds, the solidification started from the inner wall of the crucible. The crystal growth process was recorded using an optical microscope. After solidification, the as-grown samples were analyzed via scanning electron microscopy and energy-dispersive X-ray spectroscopy (EDS) to determine the microstructure and elemental composition.

Figure 1 shows a series of snapshots recorded during directional solidification of the Ni–Si eutectic at a cooling rate of –2 °C min^{-1}. The temperature gradient across the crucible was approximately 3.66 °C mm^{-1}. Lamellae were formed at the solid/melt interface, as shown in the snapshot captured at 1 s. The average phase widths of the primary (bright) and secondary (dark) phases measured from the snapshot were 5.75 and 4.36 μm, respectively. After solidification for several seconds, the lamellar spacing widened marginally (refer the snapshot at 10 s), and the average phase widths of primary and secondary phases grew to 6.73 and 5.30 μm, respectively. During the subsequent cooling process, the lamellae developed into a rough pattern (refer the snapshot at 180 s) and average phase widths enlarged to 23.62 and 16.52 μm for primary and secondary phases, respectively. According to the EDS results, the primary phase was $NiSi_2$ and the secondary phase was NiSi, and both phases were intermetallic. The results indicate that the two intermetallic phases are non-faceted during solidification, and the phase boundaries of the eutectic alloy continuously migrated even in the solid state at a temperature near melting point. This study revealed a valuable point that the actual lamellae spacing can be measured in situ despite subsequent microstructural evolution during the cooling process.

References

[1] L.-C. Chuang, K. Maeda, H. Morito, and K. Fujiwara, Scr. Mater. **211**, 114513 (2022).

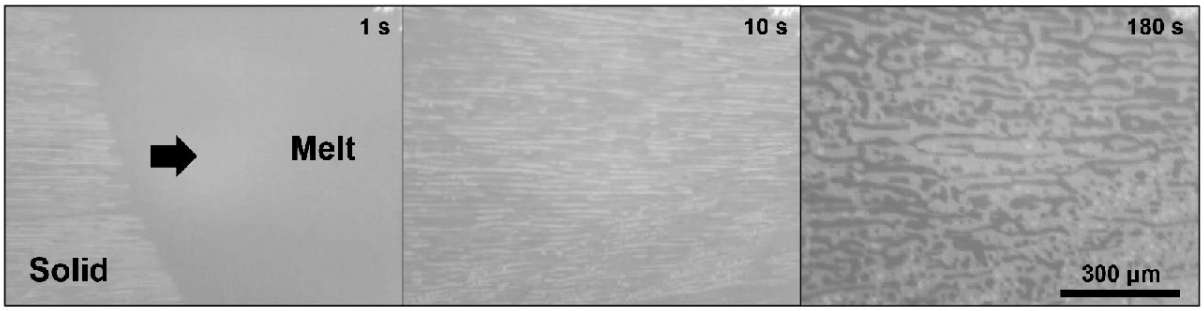

Fig. 1 Snapshots of solid/melt interface during directional solidification of $Ni_{44}Si_{56}$ alloy and the subsequent microstructure evolution at a cooling rate of 2 °C min^{-1}, recorded using an optical microscope at different times. The growth direction is toward the right [1].

Lu-Chung Chuang (Crystal Physics Research Laboratory)
E-mail: chuang.lu.chung.e8@tohoku.ac.jp
URL: http://www.imr.tohoku.ac.jp/en/about/divisions-and-centers/research-division/02.html

New-Grade Oxide dispersion strengthened Cu Alloy and Ultra-Small Testing Technologies

Oxide dispersion strengthened (ODS) alloys and high-temperature ceramics are used in advanced nuclear fission and fusion reactor systems because of their superior irradiation tolerance and high-temperature strength. We developed a new-grade ODS Cu alloy with superior strength and thermal diffusivity through nano-dispersion of Y–Zr complex oxide particles. Furthermore, we developed and applied ultra-small testing technologies for evaluating the mechanical strength of nuclear materials.

Materials resistant to extreme environments such as oxide dispersion strengthened (ODS) alloys [1,2] and ceramics [3] are crucial for achieving advanced nuclear systems.

Cu alloys with their superior thermal conductivity and strength are essential materials in high-efficiency energy transportation and conversion equipment, and even in a fusion reactor divertor heat sink. However, to use Cu alloys at high temperatures, the precipitates or dispersoids that strengthen the material must be stable at high temperatures. We developed a new-grade ODS Cu alloy with Zr addition that is strengthened by nano-sized dispersion particles of Y–Zr complex oxides obtained by mechanical alloying [1]. This new alloy was 1.5 times stronger than the conventional ODS Cu alloy with yttrium oxide dispersion particles (Fig.1). Moreover, guidelines were obtained regarding the conditions for alloy fabrication and heat treatment to suppress the decrease in thermal conductivity properties, which is tradeoff with the increase in strength.

SiC and its composites exhibit several advantageous properties as a future nuclear material, such as superior high-temperature properties, high corrosion resistance, and low radioactivation. Oxidation of SiC fibers is a potential factor limiting the service temperature of SiCf/SiC composites. Ultra-small testing technologies, such as nanoindentation and micro-pillar compression tests, are crucial for estimating the mechanical properties of nuclear materials after high-energy particle irradiation under harsh environments. Micro-pillar compression tests of pillars with a diameter of 1 μm fabricated at the center of the SiC fiber cross section revealed that the fiber strength may have been reduced by the internal oxidation reaction between residual C and O (Fig. 2).

Moreover, we suggest a simple and powerful method to measure the indentation hardness of materials with less uncertainty at the zero-point of indentation depth on the surface [4,5].

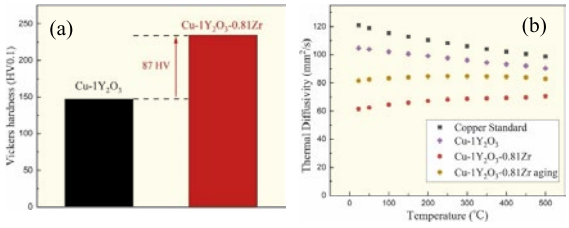

Fig.1 (a) Vickers hardness in oxide dispersion strengthened (ODS) Cu and Zr-added ODS Cu. (b) Temperature dependence of thermal diffusivity of ODS Cu alloys.

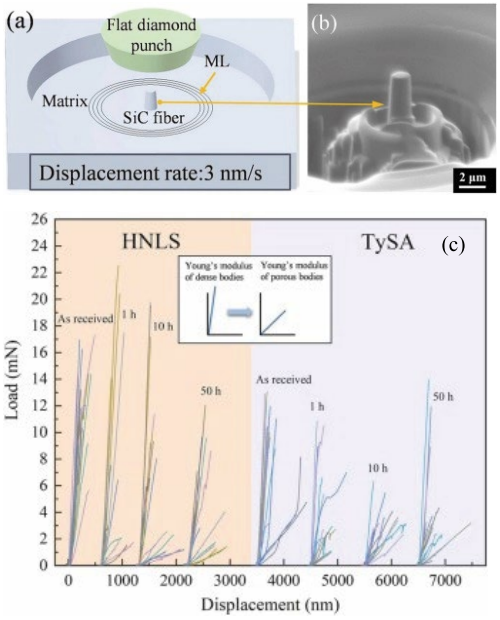

Fig.2 (a) Schematic view of micro-pillar compression test, (b) a micro-pillar fabricated in SiC fiber, and (c) load-displacement curve obtained by the micro-pillar compression tests.

References

[1] Z. Gao, H. Yu, D. Geng, Y. Liu, S. Kondo, Y. Okuno, and R. Kasada, J. Alloys & Comp. **899**, 163328 (2022).

[2] H. Wang, H. Yu, J. Liu, S. Kondo, N. Okubo, and R. Kasada, Corros. Sci. **209**, 110818 (2022).

[3] X. Yuan, S. Kondo, K. Shimoda, H. Yu, Y. Okuno, and R. Kasada, J. Eur. Ceram. Soc. **42**, 5334 (2022).

[4] D. Geng, H. Yu, Y. Okuno, S. Kondo, and R. Kasada, Sci. Rep. **12**, 6391 (2022).

[5] D. Geng, H. Yu, S. Kondo, and R. Kasada, J. Mater. Sci. **57**, 13736 (2022).

Ryuta Kasada, Sosuke Kondo, Hao Yu, and Yasuyuki Ogino (Nuclear Materials Engineering Research Laboratory)
E-mail: ryuta.kasada.e7@tohoku.ac.jp
URL: http://www.imr.tohoku.ac.jp/en/about/divisions-and-centers/research-division/13.html

Orientational Ordering of Hydroxy Groups in Kulanite

Single-crystal X-ray diffraction experiments on kulanite [Ba(Fe^{2+}, Mn, Mg)$_2$(Al, Fe^{3+})$_2$(PO$_4$)$_3$(OH)$_3$] were performed to investigate the orientational ordering of its hydroxyl groups. Structural refinements did not show a phase transition between 120 and 353 K. The orientation of the hydroxyl groups was uniquely determined along the *c*-axis in this temperature range [1].

Kulanite is a barium iron aluminum phosphate belonging to the Bjarebyite group characterized by the co-existence of heavy elements (i.e., Ba, Sr, Pb, and transition metals). This mineral also contains oxygen atoms in the form of hydroxyl groups; their orientational disorder is one of the structural characteristics of kulanite. Single-crystal X-ray diffraction of kulanite at low temperatures was performed to investigate the orientational ordering of the OH groups in kulanite.

A kulanite sample was extracted from Rapid Creek (Yukon Territory, Canada). A single crystal specimen of size 0.05×0.07×0.08 mm was attached to a glass fiber, and its diffraction intensities were measured using a Rigaku XtaLAB Synergy–S system. The temperature was controlled using a liquid nitrogen cryo-stream. The cell volumes and corresponding unit cell parameters monotonically decreased at lower temperatures, and no phase transition was detected. The results of the structural refinement were similar to those of kulanite refined at room temperature [2], except for the spatial distribution of the free OH group (O8-H1). Figure 1 shows the structure of kulanite and the difference Fourier maps obtained from structural refinement, indicating the hydrogen atom distribution. Contrarily to previous reports, our results showed that the free OH group lies on the mirror plane and does not present a disordered orientation. This spatial distribution did not change within the measured temperature range (120–353 K).

Previous Raman and infrared spectra measurements of kulanite focused on the 2600–4000 cm^{-1} region, highlighting a sharp peak at 3530 cm^{-1} and a broad peak at 3200 cm^{-1} [3]. Their shapes resembled those of solvents with free and hydrogen-bonded OH groups. Additionally, free OH stretching vibrations appear at a higher frequency than that of hydrogen-bonded OH, suggesting weakening of the covalent bond with hydrogen-bond formation. Thus, kulanite contained both free and hydrogen-bonded OH groups. The difference in the bond strengths of O8-H1 and O9-H2 was reflected in the magnitude of the decrease in the O8-O6 and O9-O3 distances with thermal expansion: from 2.668(2) Å and 3.367(2), at 120 K, to 2.680(2) Å and 3.377(2) Å, at 353 K, respectively.

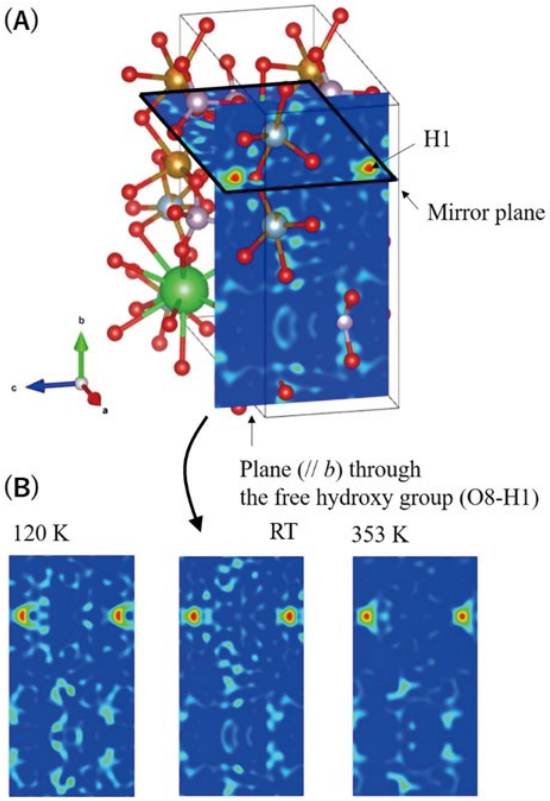

Fig. 1 (A) Difference Fourier maps in the mirror plane and the plane through the free OH group (O8-H1), at RT. (B) Difference Fourier maps in the plane through the free OH group at 120, RT, and 353 K.

References

[1] R. Yamane, M. Tokuda, and K. Sugiyama, J. Min. Petrol. Sci. **118**, 220701 (2023).
[2] M. Cooper and F. C. Hawthorne, Can. Mineral. **32**, 15 (1994).
[3] R. L. Frost, S. J. Palmer, Y. Xi, J. Čejka, J. Sejkora, and J. Plášil, Spectrochim. Acta A Mol. Biomol. Spectrosc. **103**, 431 (2013).

Ryo Yamane (Chemical Physics of Non-Crystalline Materials Research Laboratory)
E-mail: ryo.yamane.c2@tohoku.ac.jp
URL: http://www.imr.tohoku.ac.jp/en/about/divisions-and-centers/research-division/15.html

Fabrication of Ultrafine Nanoporous Intermetallic Catalysts via High-Temperature Liquid Metal Dealloying for Electrochemical Hydrogen Production

Intermetallic compounds formed from nonprecious transition metals are promising cost-effective and robust catalysts for electrochemical hydrogen production. Herein, we report the fabrication of nanoporous Co_7Mo_6 intermetallic compounds via liquid metal dealloying. The fabricated nanoporous Co_7Mo_6 exhibited high catalytic activity and durability in electrochemical hydrogen evolution reactions, demonstrating its potential as an advanced electrocatalyst.

Electrochemical hydrogen production through water splitting has emerged as a promising strategy for the effective utilization and storage of intermittent renewable energy. Crucial to this technology is the development of high-efficiency electrocatalytic hydrogen evolution reactions (HERs), particularly in alkaline media [1]. When compared to solid-solution alloys, intermetallic compounds with ordered atomic structures have homogeneous and intensified active sites, as well as the capability to form unique crystal structures to enhance geometric and electronic effects [2]. Accordingly, non-noble nanoporous intermetallics with sufficiently high HER activity and robustness have not yet been developed.

We report a liquid metal dealloying (LMD) strategy conducted at elevated temperatures to fabricate 3D nanoporous Mo-based intermetallic compounds as electrocatalysts to promote HERs [3]. Coupled with the simultaneous evolution of the 3D bicontinuous open porosity during the dealloying of single-phase precursors, the high-temperature LMD process overcomes the energy barrier, driving the direct formation of chemically ordered intermetallic phases. Combined experimental analyses and molecular dynamics simulations uncovered an intermetallic effect; consequently, high-temperature chemical ordering during nanopore formation suppressed dealloyed nanostructure coarsening (Fig. 1).

The ultrafine 3D nanoporous μ-Co_7Mo_6, with a large accessible surface area and abundant active sites, exhibits catalytic activity that is close to yet inferior to that drop-casted electrodes of Pt/C; however, the catalytic activity is improved in nanoporous μ-Co_7Mo_6 sheet electrodes (Figs. 2a-b). Along with superior electrocatalytic activity, the nanoporous μ-Co_7Mo_6 electrodes exhibited superior durability after 5000 cycles of accelerated degradation testing, showing a negligible shift in the HER polarization curves and negligible change in its porous structure (Fig. 2c), and delivered a high current density of ~170 mA cm^{-2} at an overpotential of 150 mV, without significant current decay over a long-term chronoamperometry test for 48 h (Fig. 2d). This study sheds light on the development of advanced nanoporous intermetallic electrocatalysts.

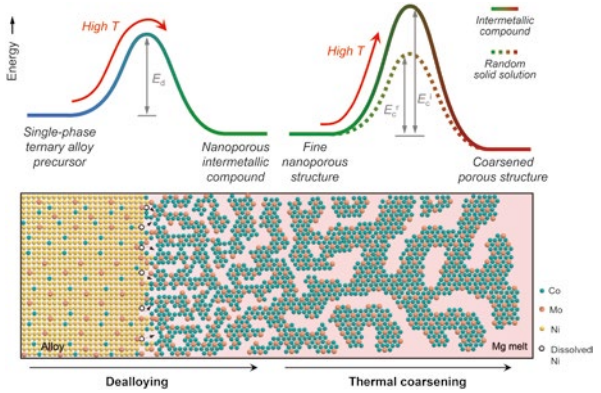

Fig. 1 Schematic illustrations of the fabrication of ultrafine nanoporous μ-Co_7Mo_6 intermetallic compound via liquid metal dealloying.

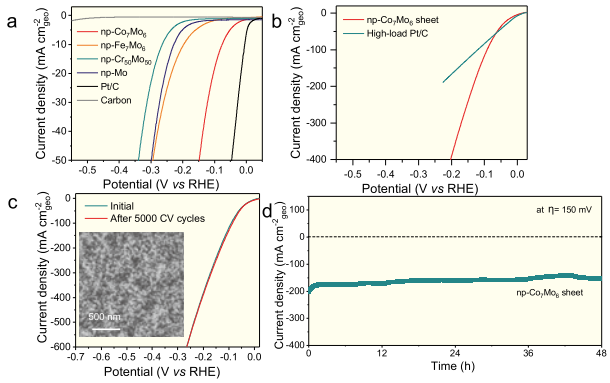

Fig. 2 iR-corrected hydrogen evolution reaction polarization curves of nanoporous μ-Co_7Mo_6 (a) compared with the reference materials on a disk electrode, (b) compared to a high-load Pt/C catalyst, and (c) collected before and after the accelerated degradation test for 5000 cycles. Inset: Scanning electron microscopy image of the np-Co7Mo6 sheet after the stability measurement. (d) Long-term stability measurements for 48 h at 150 mV overpotential.

References

[1] J. Kibsgaard and I. Chorkendorff, Nat. Energy **4**, 430 (2019).

[2] Y. Yan, J. S. Du, K. D. Gilroy, D. Yang, Y. Xia, and H. Zhang, Adv. Mater. **29**, 1605997 (2017).

[3] R. Song, J. Han, M. Okugawa, R. Belosludov, T. Wada, J. Jiang, D. Wei, A. Kudo, Y. Tian, M. Chen, and H. Kato, Nat. Commun. **13**, 5157 (2022).

Hidemi Kato (Non-Equilibrium Materials Research Laboratory)
E-mail: hidemi.kato.b7@tohoku.ac.jp
URL: http://www.nem2.imr.tohoku.ac.jp/index-e.html

Heteroepitaxial Fabrication of Binary Colloidal Crystals by Balancing Interparticle Interaction and Lattice Spacing

The colloidal epitaxy utilizing a patterned substrate is used to fabricate colloidal crystals with the same structure and lattice spacing with the substrate. However, this technique has been primarily limited to a single-component system. We show that the heteroepitaxial growth technique enables the fabrication of complex multicomponent colloidal crystals that significantly facilitate versatile applications of the colloidal crystals.

When compared to single-component colloidal crystals, binary colloidal crystals (b-CCs) have gained considerable attention owing to their various structures, which are critical for versatile applications such as biosensors [1] and photonic crystals [2]. However, controlling the growth and structures of the b-CCs is still challenging because of their complex structures. Recently, we reported that one-dimensional (1D) heteroepitaxy occurs when growing b-CCs [3]. The b-CCs grow epitaxially at the edge of previously formed single-component colloidal crystals. In this study, based on the availability of 1D heteroepitaxy, we demonstrated two-dimensional (2D) heteroepitaxial growth of b-CCs [4].

The heteroepitaxial growth for the binary system is achieved by the following procedure. A convective assembly technique utilizes solution evaporation to gather and arrange particles into thin colloidal crystal layers. Colloidal suspensions that are dropped on cover glass gradually evaporate to form a thin colloidal crystal as the substrate. Epitaxially grown colloidal crystals that were observed from the bottom using inverted optical microscopy and stacking structures were identified using a confocal laser scanning microscope. Various types of b-CCs were created by adjusting the particle size ratio and polymer concentration, as shown in Fig. 1. This is the first time that various types of b-CCS are created by heteroepitaxial growth. Our heteroepitaxial growth technique can be used in a new approach for structure-controlled colloidal self-assembly in multicomponent systems such as fabricating photonic bandgap materials.

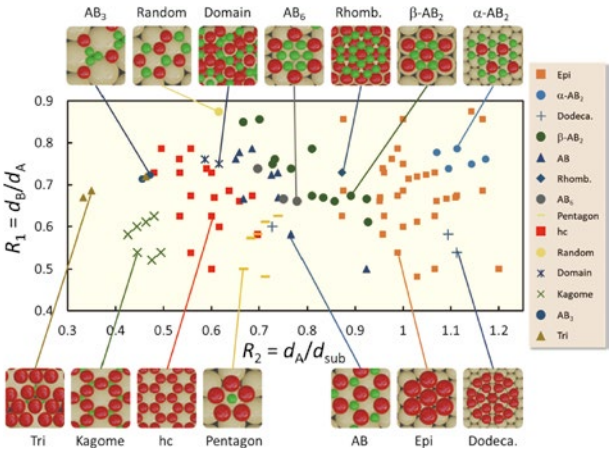

Fig. 1 Various binary colloidal crystals formed via heteroepitaxial growth are plotted with respect to the particle size ratio of $R1$ (dB/dA) and $R2$ (dA/$d$sub), where d_A, d_B, and d_{sub} are the particle sizes of large, small, and substrate particles, respectively. Epitaxially grown unary colloidal crystals (Epi), a-AB2-phase (a-AB2), b-AB2-phase (b-AB2), dodecagonal structure (Dodeca), AB6-structure (AB6), AB-structure (triangular) (AB), rhombic structure (Rhomb.), domain structure (Domain.), pentagon structure (pentagon), random structure (Random), AB3-structure (AB3), honeycomb structure (hc), triangular structure (tri), and kagome lattice structure (Kagome) are plotted.

References

[1] G. Singh, H.J. Griesser, K. Bremmell, and P. Kingshott, Adv. Funct. Mater. **21**, 540 (2011).

[2] A.P. Hynninen, J.H. Thijssen, E.C. Vermolen, M. Dijkstra, and A. van Blaaderen, Nat. Mater. **6**, 202 (2007).

[3] J. Nozawa, S. Uda, A. Toyotama, J. Yamanaka, H. Niinomi, and J. Okada, Cryst. Growth Des. **20**, 3247 (2020).

[4] J. Nozawa, S. Uda, A. Toyotama, J. Yamanaka, H. Niinomi, and J. Okada, J. Colloid Interface Sci. **608**, 873 (2022).

Junpei Okada (Crystal Chemistry Research Laboratory)
E-mail: jun.nozawa.e3@tohoku.ac.jp
URL: http://www.imr.uda-lab.imr.tohoku.ac.jp/index-e.html

Pseudorotating Hydride Complexes with Ninefold Hydrogen Coordination at Temperatures Far Below Room Temperature

Solid-state materials containing rotatable polyanions constitute a peculiar class of ionic conductors because of their unique transport mechanism, where the reorientational motions induce phase transitions with several orders of magnitude enhancement in counterion conductivities. A major drawback is the high temperature required to activate rotation; consequently, low conductivities are observed at room temperature. In this regard, we have theoretically demonstrated a novel strategy of drastically reducing the temperature by utilizing "pseudorotation" of hydride complexes with high hydrogen coordination as a new class of rotatable polyanions. Here, we provide experimental evidence of the low-temperature activation of the rotational motion of hydride complexes with ninefold hydrogen coordination.

Currently, there is a strong demand to replace organic liquid electrolytes used in conventional batteries with solid-state electrolytes owing to their multiple advantages, such as better safety and higher energy density. Considerable effort has been devoted to identifying materials with superior transport properties.

Among the diverse solid-state electrolytes, those containing rotatable polyanions constitute a peculiar class of materials owing to their unique transport behavior, i.e., polyanions rotate at an elevated temperature, thereby promoting phase transitions with several orders of magnitude enhancement in counterion conductivities. However, a major drawback is the high temperature required to activate rotation, resulting in low conductivities at room temperature (RT). Thus, we recently proposed a novel approach to significantly reduce the temperature based on the use of hydride complexes with high hydrogen coordination, wherein hydrogen is the sole ligand species that can be covalently bound to single transition metals. The essence of the approach is that, unlike other polyanions, the rotation only requires small displacements of highly mobile hydrogen and therefore occurs with low activation energy. We applied this approach to an existing hydride Li_5MoH_{11} containing a ninefold hydrogen coordination hydride complex MoH_9^{3-} [1], and theoretically demonstrated the use of this material as a novel RT lithium superionic conductor [2].

In this study, we conducted quasielastic neutron scattering (QENS) measurements of Li_5MoH_{11} to experimentally demonstrate the low-temperature activation of pseudorotation.

Figure 1 shows the dynamic structure factor $S(Q,E)$ of Li_5MoH_{11} measured in a temperature range of 10–300 K. We observed that a QENS signal appeared at a temperature >150 K because of the relaxation of hydrogen atoms. The intermediate scattering functions derived from the QENS spectra

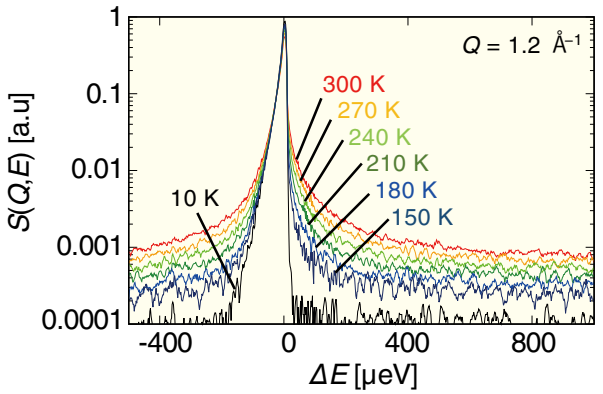

Fig. 1 Quasielastic neutron scattering spectra of Li_5MoH_{11} measured at various temperatures at Q = 1.2 Å^{-1}.

were satisfactorily fitted using a stretched exponential function called the Kohlrausch–Williams–Watts function with an anomalously small stretching exponent $\beta \approx 0.3$–0.4, suggesting a wide relaxation time distribution. The Q dependence of the elastic incoherent structure factor was reproduced by the rotational diffusion of MoH_9^{3-}. The results were satisfactorily supported by a van Hove analysis of the motion of hydrogen atoms obtained using first-principles molecular dynamics calculations. We conclude that the wide relaxation time distribution of the MoH_9^{3-} rotation is due to the positional disorder of the surrounding Li ions that arise because of the significant Li^+ diffusion and deformation of MoH_9 unit by pseudorotation [3].

References

[1] S. Takagi, Y. Iijima, T. Sato, H. Saitoh, K. Ikeda, T. Otomo, K. Miwa, T. Ikeshoji, and S. Orimo, Sci. Rep. **7**, 44253 (2017).

[2] S. Takagi, T. Ikeshoji, T. Sato, and S. Orimo, Appl. Phys. Lett. **116**, 173901 (2020).

[3] Y. Ohmasa, S. Takagi, K. Toshima, K. Yokoyama, W. Endo, S. Orimo, H. Saitoh, T. Yamada, Y. Kawakita, K. Ikeda, T. Otomo, H. Akiba, and O. Yamamuro, Phys. Rev. Res. **4**, 033215 (2022).

Shigeyuki Takagi and Shin-ichi Orimo (Hydrogen Functional Materials Research Laboratory)
E-mail: shigeyuki.takagi.c5@tohoku.ac.jp
URL: http://www.hydrogen.imr.tohoku.ac.jp/en/index.html

Hole Doping in Cu-Based Semiconductors with an Isovalent Cation

P-type doping in Cu(I)-based semiconductors is pivotal for various applications as semiconductors. Impurity doping is a fundamental technology to overcome the intrinsic limits of hole concentration controlled by native defects. Recently, we reported that alkali metal impurities are prominent p-type dopants for the Cu(I)-based cation-deficient hole conductors. When the size mismatch with Cu^+ in the host lattice is increased, these isovalent impurities are preferentially located at interstitial positions to form stable impurity–defect complexes. We demonstrate that the Cs impurity in γ-CuI semiconductors enhances hole concentration controllability for both single crystals and thin films. Our first-principles calculations indicate that the Cs impurity forms impurity–defect complexes that act as shallow acceptors. This isovalent doping provides an approach for controlled doping into cation-deficient semiconductors through an interaction of impurities with native defects.

Adding impurities with acceptor or donor properties, known as impurity doping, is the benchmark method for bolstering the transport properties of semiconductors and device performance. Conventionally, ions with lower valency than the constituent atoms have been used as such impurities. However, in Cu(I)-based semiconductors, which have multiple applications, e.g., hole transport layer in perovskite solar cells, ions with a valence lower than that of monovalent Cu ions do not exist, and thus the p-type doping has not been established so far [1].

To propose a new carrier doping design for the p-type doping, we focused on the alkali impurity effect, which has been empirically used for hole doping in Cu monovalent semiconductors, Cu_2O and Cu(In,Ga)Se_2. First, we experimentally demonstrated that p-type doping with alkali-ion impurities, which has the same valence as Cu but a larger size, can improve conductivity in Cu(I)-based semiconductors. Our theoretical analyses show that the complex defects composed of alkali-ion impurity and vacancies of Cu ions, are an origin of the p-type conductivity (Fig. 1).

Based on the p-type doping mechanism to form acceptor-type Cu vacancy defect complex, we investigated larger alkaline ions, such as Na, Rb, and Cs, as acceptor impurities in γ-CuI. Among them, the Cs ions could bind more Cu vacancies, leading to a greater concentration of stable charge carriers (10^{13} – 10^{19} cm^{-3}) both in single crystals and thin films prepared from the solution. This suggests that the method can be used to fine-tune carrier concentrations under low-temperature processing for specific applications and devices. This would allow a whole new range of applications for these p-type materials.

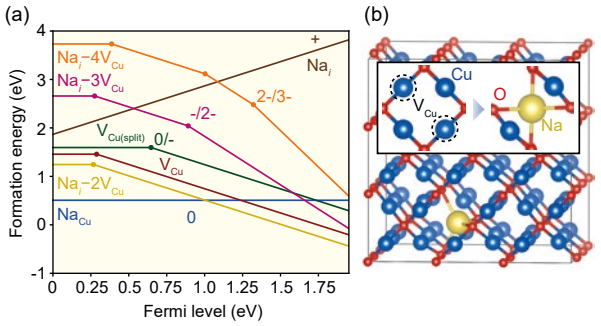

Fig. 1 (a) Theoretical point defect energetics of native point defects, isovalent Na dopants, and their defect complexes in Cu_2O as a function of the Fermi level. (b) Atomic structure of the Na-related complex defect.

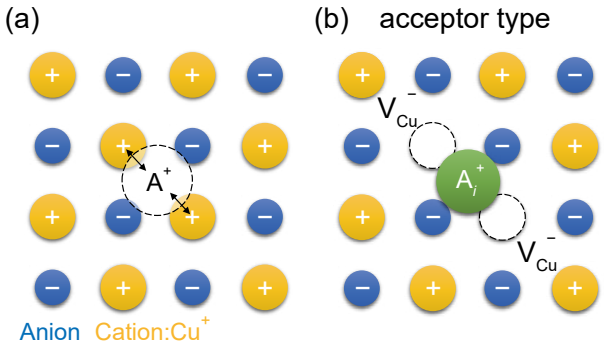

Fig. 2 Schematic defect formation models for isovalent cation dopants. If the ionic radius of the impurity is sufficiently large against the interstitial vacant space to push away the nearest neighboring Cu cations, multiple Cu vacancies are generated.

References

[1] T. Matsuzaki, N. Tsunoda, Y. Kumagai, Y. Tang, K. Nomura, F. Oba, and H. Hosono, J. Am. Chem. Soc. **144**, 16572 (2022).

Yu Kumagai (Multi-Functional Materials Science Research Laboratory)
E-mail: yukumagai@tohoku.ac.jp
URL: https://kumagailab.imr.tohoku.ac.jp/en/

Laser-Induced Breakdown Spectroscopy for Quantitative Three-Dimensional Hydrogen Mapping

For the development and maintenance of materials and infrastructures that enable the achievement of "hydrogen society," an analytical technique capable of determining hydrogen distribution is highly desirable. We present a method for obtaining a three-dimensional quantitative hydrogen distribution in an Ni–metal hydride (MH) battery cathode using laser-induced breakdown spectroscopy (LIBS) and demonstrate that the reaction distribution in the cathode can be interpreted based on a state-of-charge distribution converted from the hydrogen distribution. In this method, we measured the hydrogen emission-line intensities at 656.28 nm for a commercial Ni–MH battery cathode cycled 1000 times at 1 C under a 3000 Pa helium atmosphere. The proposed LIBS method allows us to understand the deterioration mechanism of an Ni–MH battery and improve its cycle life and capacity.

"Hydrogen society," which refers to the use of hydrogen in daily life and industrial activities, has recently attracted attention owing to a worldwide effort to achieve net-zero emissions of greenhouse gases [1]. For achieving a hydrogen society, the development of materials related to hydrogen production, hydrogen storage, hydrogen transportation, and electric power generation using hydrogen is crucial. Accordingly, efficient analytical techniques for mapping hydrogen with a spatial resolution in tens of micrometers along the planar and depth directions are essential for the fabrication and maintenance of such materials. To satisfy this requirement, we focused on laser-induced breakdown spectroscopy (LIBS) and developed a LIBS-based method to quantitatively acquire the three-dimensional hydrogen distribution using an Ni–metal hydride (MH) battery cathode as an analyte.

Quantitative hydrogen and state-of-charge (SOC) distributions for a commercial Ni–MH battery cathode cycled 1000 times at 1 C were acquired by measuring the hydrogen emission intensity at 656.28 nm under a 3000 Pa helium atmosphere. This measurement condition was established in our previous study [2, 3].

For determining the hydrogen and SOC distributions, Ni–MH battery cathodes were discharged or charged once at a C-rate of 0.1 C, which was considered as reference samples. The SOC distributions were obtained based on the assumption that the SOCs of the discharged and charged Ni–MH battery cathodes were 0 and 100%, respectively, and the SOC decreased linearly with an increase in hydrogen emission intensity at 656.28 nm. SOC maps of the commercial Ni–MH battery cathode after the 1000th charging at 1 C exhibited an inhomogeneous distribution (Fig. 1), demonstrating that the degradation of the commercial Ni–MH battery occurred uniformly in the planar and depth directions of the cathode. This SOC distribution can be explained on the basis of proton transfer in the cathode. The average SOC of the layer that was 75 μm deep from the surface is 21%, as shown in Fig. 1, which is nearly consistent with the SOC evaluated from the charge–discharge curves (37%). These results indicate that the present LIBS measurement system can provide three-dimensional quantitative SOC maps of Ni–MH battery cathodes.

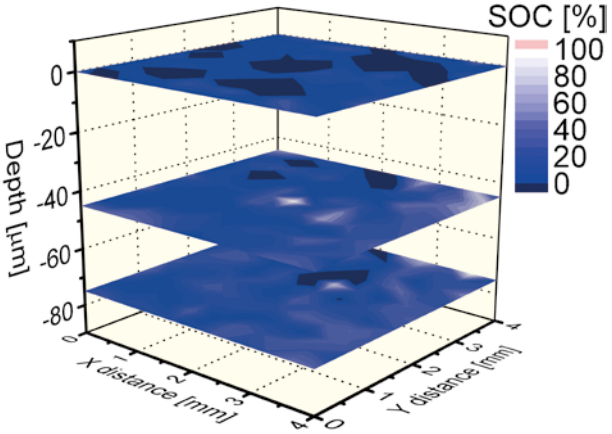

Fig. 1 Three-dimensional state-of-charge maps of the commercial Ni–metal hydride battery cathode after the 1000th charging at 1 C [4].

References

[1] I. Staffell, D. Scamman, A. Velazquez Abad, P. Balcombe, P. E. Dodds, P. Ekins, N. Shah, and K. R. Ward, Energy Environ. Sci. **12**, 463 (2019).

[2] S. Imashuku, T. Kamimura, S. Kashiwakura, and K. Wagatsuma, Anal. Chem. **92**, 11171 (2020).

[3] S. Imashuku, T. Kamimura, T. Kawaguchi, and T. Ichitsubo, e-J. Surf. Sci. Nanotechnol. **20**, 7 (2022).

[4] S. Imashuku, T. Kamimura, T. Ichitsubo, and K. Wagatsuma, Analyst **147**, 5161 (2022).

Susumu Imashuku (Analytical Science Research Laboratory)
E-mail: susumu.imashuku.e8@tohoku.ac.jp
URL: http://www.imr.tohoku.ac.jp/en/about/divisions-and-centers/research-division/27.html

Structural Quantum Criticality—Broken Translational Symmetry by Controlling the Chemical Composition

Quantum criticality, where symmetry breaking is suppressed to absolute zero, induces exotic phenomena. By combining x-ray, neutron, calorimetry measurements, and first-principle calculation, we show complete suppression of the structural transition by controlling the chemical composition. Near the structural quantum critical point, crystalline and amorphous characteristics with partially broken translation symmetry are realised.

Symmetry breaking is a fundamental concept in condensed matter physics. In solids, exotic quantum phases with broken spatial- or time-reversal symmetries have been extensively studied over the past decades. These broken symmetries always accompany phase transitions. A typical phase transition involves a change in the crystal structure. Such structural phase transitions usually occur at finite temperatures. However, certain perturbations can lower the transition temperature to absolute zero. The transition point at absolute zero is called the structural quantum critical point.

We aimed to demonstrate that chemical composition can lead to structural quantum criticality, where a translation symmetry, an essential component of crystal symmetry, is partially broken by complete suppression of a structural phase transition [1].

$BaAl_2O_4$ is a dielectric compound, showing a structural phase transition at T_C = 450 K from the space group $P6_322$ to $P6_3$ on cooling (Fig.1(a)). This structural phase transition is driven by the acoustic soft phonon mode owing to the tilting of AlO_4 tetrahedra, whose vibration is similar to that of sound waves. The soft mode is tunable by chemical composition as $Ba_{1-x}Sr_xAl_2O_4$. Figure 1(a) shows that T_C is rapidly suppressed by substituting Sr for Ba atoms and disappears near x = 0.1. For the composition regime of $0.1 \le x \le 0.5$, diffuse scattering can be observed in electron diffraction, which indicates that the soft mode exists at significantly low or nearly zero frequencies. A further increase in x induces another structural phase transition to the space group $P2_1$ at $x > 0.55$.

To investigate phonons from microscopic views, an inelastic neutron scattering experiment was performed on powder samples. Figure 1(b) shows the intensities observed for different values of x. The sample with x = 0 shows crystalline characteristics, i.e., peak formations. A shoulder (filled triangle) near the peak at approximately 5 meV originates from the acoustic phonons. The experimental findings are well accounted for by our first-principle calculation.

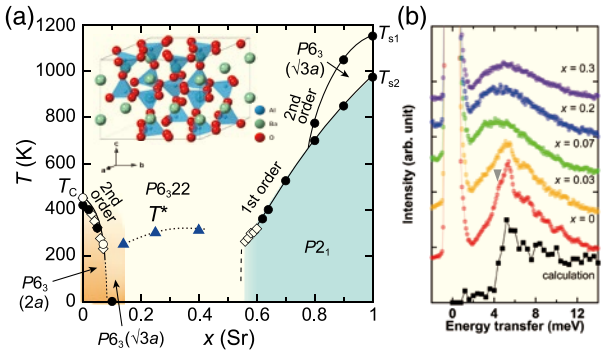

Fig. 1 (a) Phase diagram of $Ba_{1-x}Sr_xAl_2O_4$ and inset shows the crystal structure of $BaAl_2O_4$ ($P6_3$). (b) Inelastic neutron scattering spectra integrated over $|Q|$ = 2–4 $Å^{-1}$, with E_i = 17.255 meV. Profiles are shifted vertically for clarity.

With increasing x, the peaks started broadening, and they entirely disappeared at $x \ge 0.07$ and formed a broad peak, reflecting amorphous characteristics.

We also determined that when x was greater than the structural quantum critical point, $Ba_{1-x}Sr_xAl_2O_4$ exhibited the thermal characteristic of amorphous materials, i.e., low thermal conductivity comparable to that of glassy materials. This indicates that a part of the crystal structure loses periodicity because of the incoherently stopped acoustic soft phonon mode. When combined with the pair distribution function analysis, a combination of a glassy AlO_4 network and a periodic Ba/Sr arrangement is realised.

Thus, we succeeded in creating hybrid materials that combine crystalline and amorphous characteristics, and elucidated the physics related to structural quantum criticality [1]. This research can lead to further development of high-heat-resistance materials, that can be utilised for insulation materials in harsh environments such as outer space.

References

[1] Y. Ishii, A. Yamamoto, N. Sato, Y. Nambu, S. Ohira-Kawamura, N. Murai, K. Ohara, S. Kawaguchi, T. Mori, and S. Mori, Phys. Rev. B **106**, 134111 (2022).

Yusuke Nambu (Exploratory Research Laboratory)
E-mail: nambu@tohoku.ac.jp
URL: http://nambu.imr.tohoku.ac.jp/en/

Electronic Materials

IMR KINKEN Research Highlights 2023

Determination of Exchange Coupling in Heterometal Ring Cluster using High-Frequency Electron Paramagnetic Resonance

We investigated a series of heterometallic ring clusters {Sc_nGd_n} (n=4, 6, and 8) with the aim of controlling spin-wave excitations. While Gd^{3+} has S=7/2 spin, an Sc^{3+} ion has no magnetic moment and works as a magnetic linker between the Gd^{3+} ions. High-frequency electron paramagnetic resonance measurements revealed a nontrivial resonance peak with a shift via antiferromagnetic exchange coupling caused by the mixing between the f-state of Gd and the d-states of Sc.

Recently, the possibility of controlling spin waves for future device applications and information science has been intensively studied. Various ferromagnetic and antiferromagnetic compounds have been used as target systems for engineering spin-wave excitations. Bulk magnetic materials or thin films are composed of boundaries or interfaces, and the formation of these broken symmetries causes difficulties in the handling of spin waves. Moreover, the size of the system cannot be scaled down to the nanometer scale.

A ring cluster complex is a new breakthrough in the field of "spintronics" because of its inherent advantages. First, a spin wave can be excited within a nanoscale cluster in a ring shape with a perfect cyclic boundary condition. The coupling between clusters is negligibly small. Owing to the ring shape, a series of spin waves can be excited as higher-order excitations. However, to utilize these advantages, we must overcome two challenges: 1) synthesis of ideal ring compounds and 2) control of spin waves.

Using amino-polyalcohol ligands with both N and O donors, we obtained a series of Sc–Gd heterometallic rings with ring topologies. As a basic unit, we used cyclic compounds and regulated the reaction conditions for a self-assembling cluster synthesis [1]. When n=8, Sc_8Gd_8 exhibits a saddle-shaped cluster and the crystal packing is tetragonal with S_4 symmetry. The average Sc–Gd distance is 3.51 Å and the small distribution results in a magnetic ring with a single exchange coupling parameter. When n=6, Sc_6Gd_6 exhibits a wheel-like cluster with C_3 symmetry, and the crystal packing is trigonal. The average Sc–Gd distance is 3.52 Å. When n=4, Sc_4Gd_4 also exhibits a wheel-like cluster with a monoclinic crystal. The average Sc–Gd distance is 3.71 Å.

The spin-wave excitations are dominated by the magnetic interactions between the Gd spins. There are two types of interactions: exchange and dipole–dipole interactions. The latter type of interaction is usually significantly weak, but is important for magnetic anisotropy.

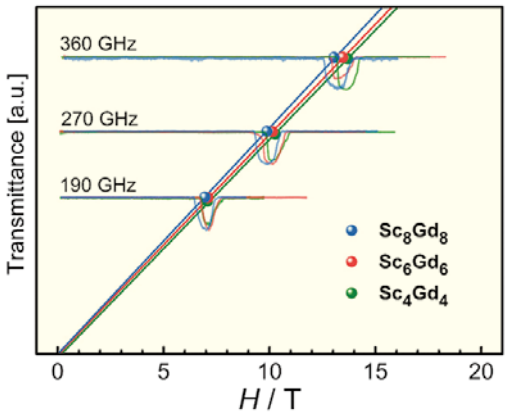

Fig. 1 High-frequency electron spin resonance shows the spectra of different shifts for three compounds. The exchange coupling parameter can be determined by the high resolution of TESRA-IMR [3].

The key experiment involved determining the Gd–Sc exchange coupling via high-frequency electron paramagnetic resonance (EPR). We observed the systematic frequency dependence of the EPR spectra at frequencies between 190 and 360 GHz using a terahertz electron spin resonance (ESR) system called Terahertz ESR Apparatus-Institute of Materials Research (IMR) developed by the magnetism division of IMR [2]. The spectra show the linear frequency-field relations with small zero-field gaps. The gaps are attributed to the exchange constants of −0.01, −0.01, and −0.03 cm^{-1} for n=8, 6, and 4 compounds, respectively. These values are consistent with the variations in Sc–Gd distances.

References

[1] H. L Zhang, Y. Q. Zhai, H. Nojiri, C. Schröder, H. K. Hsu, Y. T. Chan, Z. Fu, and Y. Z. Zheng, J. Am. Chem. Soc. **144**,15193 (2022).

[2] H. Nojiri, Y. Ajiro, T. Asano, and J.-P. Boucher, New J. Phys. **8**, 218 (2006).

[3] Reprinted with permission from {/doi.org/10.1021/jacs.2c05421}. Copyright 2022 American Chemical Society.

Hiroyuki Nojiri (Magnetism Research Laboratory)
E-mail: hiroyuki.nojiri.e8@tohoku.ac.jp
URL: http://www.hfpm.imr.tohoku.ac.jp

Electronic Functionality Sensitive to Crystalline Ordering in Ferromagnetic Alloy Thin Films

We fabricated ferromagnetic thin films of a full-Heusler alloy Co_2FeSn, which is theoretically proposed to have a topological band structure in the $L2_1$-type ordered phase. By establishing an annealing method to promote the $L2_1$-type crystalline ordering, we examined the changes in the electrical and thermoelectric transport properties. Our results highlight the critical importance of controlling the crystalline ordering when exploring the topological electronic states and exotic functionality in full-Heusler alloy thin films.

Ordered alloys have been investigated intensively in the field of spintronics because there are several useful ferromagnetic materials with high Curie temperatures and spin polarization. Of particular interest is a ternary system called the $L2_1$-type full-Heusler alloy, which is an intermetallic compound with the stoichiometric composition of X_2YZ (in general, X and Y are transition elements, and Z is a typical element). In the past decade, the research on full-Heusler alloys has been expanded to topological physics focusing on the investigations on nontrivial electronic states emerging in solids. Specific crystal lattices, symmetries, and spin-orbit coupling play a role in yielding topological features. The feasibility of incorporating various elements and controlling the degree of the crystalline ordering (and consequently, the lattice symmetry) in X_2YZ alloys makes this system particularly appealing to study the structure-topological property relationship.

Motivated by this point, we attempted to fabricate thin films of a nodal line semimetal candidate, Co_2FeSn [1]. The nodal line semimetal is a class of topological materials in which finite contributions of Berry curvature arise near the energy of the nodal lines produced by band crossing, resulting in giant anomalous Hall and Nernst effects. Despite the possible superior transport properties, methods to promote the crystalline ordering of the Co–Fe–Sn ternary alloy in a thin-film form have not yet been established. By combining the co-sputtering deposition at a low temperature (150 °C) and annealing at a high temperature (600–700 °C), we successfully promoted the crystalline ordering from the less-ordered $B2$-type (Fig. 1(a)) to the $L2_1$-type (Fig. 1(b)) in Co_2FeSn thin films on MgO(001) [2]. Moreover, by launching a measurement system capable of evaluating electrical and thermoelectric transport properties in thin films, we revealed the strong and qualitatively different influences of the crystalline ordering on the anomalous Hall effect. As shown in Fig. 1(c), the Hall conductivity becomes almost

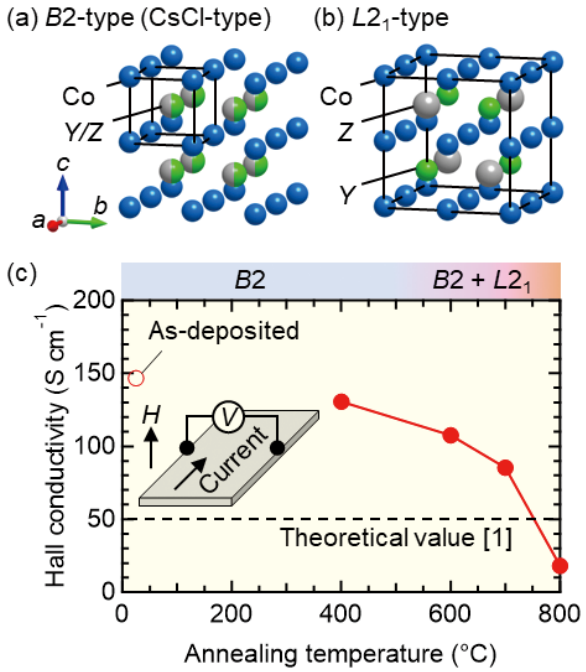

Fig. 1 Crystal structures of (a) $B2$-type and (b) $L2_1$-type Co_2YZ. (c) Annealing temperature dependence of anomalous Hall conductivity. For comparison, the theoretical value [1] is included.

equal to the theoretical value by performing the high-temperature annealing that induces the $L2_1$-type ordering. This result provides a platform for exploring giant magnetic responses in Co_2FeSn by Fermi-energy tuning. Boosted by these newly added aspects of topological physics, the interest in metallic alloys will continue to be inexhaustible.

References

[1] J. Noky, J. Gooth, C. Felser, and Y. Sun, Phys. Rev. B **98**, 241106(R) (2018).

[2] K. Fujiwara, K. Shibata, S. Nishimura, J. Shiogai, and A. Tsukazaki, AIP Adv. **12**, 065030 (2022).

Kohei Fujiwara (Low Temperature Physics Research Laboratory)
E-mail: kohei.fujiwara@tohoku.ac.jp
URL: http://mu.imr.tohoku.ac.jp/index_en.html

Understanding the Mechanism of Quantum Spin-Liquid State in Organic Materials

Inelastic neutron scattering measurements have revealed an abrupt change in the phonon damping at the 6 K anomaly in the quantum spin-liquid candidate κ-(BEDT-TTF)$_2$Cu$_2$(CN)$_3$. This is interpreted as a phase transition to the valence-bond solid state on the basis of an effective model describing the spin-charge coupling in the dimer-Mott system.

Experimental observation of lattice vibrations by inelastic neutron scattering experiments has been limited to a few exceptional materials because large single crystals are required for these experiments. An international collaborative research group has recently succeeded in observing lattice vibrations coupled with electronic dielectricity and antiferromagnetic ordering in the molecular organic Mott insulator κ-(BEDT-TTF)$_2$Cu[N(CN)$_2$]Cl, where BEDT-TTF is bis-(ethylenedithio)tetrathiafulvalene [1]. Such couplings and the inter-correlated degrees of freedom among charge, spin, and lattice states in a strongly correlated electron system are important for the possible quantum liquid state.

We succeeded in obtaining a clear lattice vibration signal from the quantum spin-liquid candidate κ-(BEDT-TTF)$_2$Cu$_2$(CN)$_3$ via inelastic neutron scattering experiments [2]. This experiment was conducted as an international remote experiment through online remote operation and online meetings between Japan and Europe because overseas travel was not possible owing to the global spread of the coronavirus infection at the time of the experiments.

In the inelastic neutron experiment, we observed that the optical mode at E = 4.7 meV, which is considered to be the breathing mode of the BEDT-TTF molecular dimer, is strongly over-damped above 6 K. Below 6 K, the line width rapidly narrows to the instrumental resolution and changes to a normally decaying state. The breathing mode of the BEDT-TTF molecular dimer is common to both κ-(BEDT-TTF)$_2$Cu[N(CN)$_2$]Cl and κ-(BEDT-TTF)$_2$Cu$_2$(CN)$_3$ and is closely related to the change in the π-electron state. The coupling between the π-electron and the breathing mode is a common property of the dimer-Mott-type molecular organic conductors. Comparison of this temperature change in the breathing mode with a theoretical model that considers the π-electron charge disproportionation within the BEDT-TTF dimer suggests that a spin singlet state, in which BEDT-TTF molecules form a tetramer, i.e., a valence-bond-solid (VBS) state, is expected below 6 K, rather than the quantum spin-liquid state in which the geometrical frustration in the triangular lattice has been discussed as the origin so far (Fig. 2).

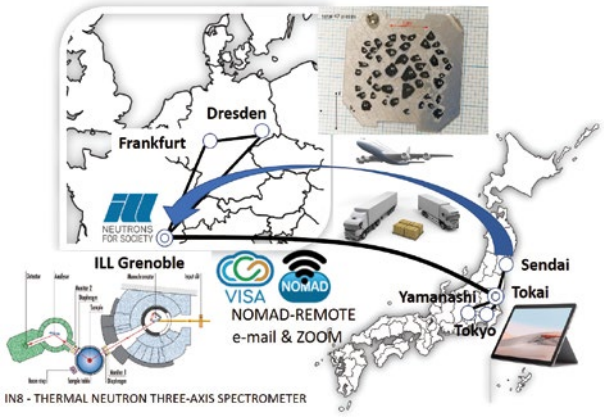

Fig. 1 International remote inelastic neutron scattering experiment conducted between France, Germany, and Japan.

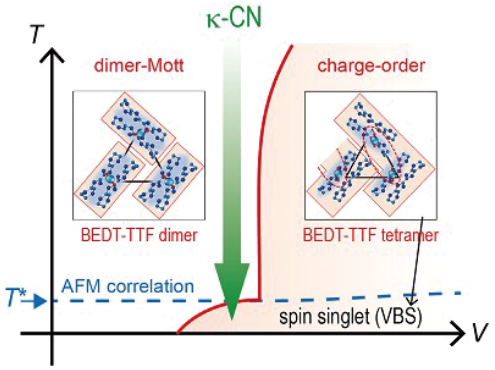

Fig. 2 Conceptual diagram of electronic state of κ-(BEDT-TTF)$_2$Cu$_2$(CN)$_3$. Transition from molecular dimer state (paramagnetic state) to molecular tetramer state (spin singlet state) with the development of antiferromagnetic correlations

References

[1] M. Matsuura, T. Sasaki, S. Iguchi, E. Gati, J. Mueller, O. Stockert, A. Piovano, M. Bohm, J. T. Park, S. Biswas, S. M. Winter, R. Valenti, A. Nakao, and M. Lang, Phys. Rev. Lett. **123**, 027601 (2019).

[2] M. Matsuura, T. Sasaki, M. Naka, J. Mueller, O. Stockert, A. Piovano, N. Yoneyama, and M. Lang, Phys. Rev. Research **4**, L042047 (2022).

Takahiko Sasaki (Low Temperature Condensed State Physics Research Laboratory)
E-mail: takahiko.sasaki.d3@tohoku.ac.jp
URL: http://cond-phys.imr.tohoku.ac.jp/index_e.html

Low-Energy Spin Dynamics Coupled with Hole Mobility in T*-Type $La_{0.86}Eu_{0.86}Sr_{0.28}CuO_4$

The interplay between low-energy spin dynamics and the mobility of doped holes in a T*-type $La_{0.86}Eu_{0.86}Sr_{0.28}CuO_4$ (LESCO) was investigated via ^{139}La-nuclear magnetic resonance and electrical resistivity measurements. We clarified the reduction in the spin fluctuations due to the localization of the holes with decreasing temperature. The result suggests a coupling between the spin and charge degrees of freedom in LESCO.

The magnetic properties of CuO_2 layers in high-temperature superconducting (SC) materials are significantly dependent on the charge mobility. Therefore, the evolution of spin correlation with doping has been extensively studied. It is well known that a small amount of hole doping into La_2CuO_4 having distorted K_2NiF_4-type crystal structure containing CuO_6 octahedral tilts destroys the antiferromagnetic order. Sufficient number of hole carriers induces incommensurate spin structure, which is concomitant with the emergence of the SC phase. However, such doping-dependent evolution of magnetism is recently thought to be influenced by the local structure around the CuO_2 plane and Cu coordination through the modification of the electronic state.

Our study on T^*-type $La_{1-x/2}Eu_{1-x/2}Sr_xCuO_4$ (LESCO) having CuO_5 coordination with one site of apical oxygen revealed the appearance of an SC phase with marginal hole doping with $x \leq 0.20$. The phase diagram of LESCO shows a possibility for the emergence of superconductivity in an Sr-free compound, similar to the SC phase for T'-type $La_{2-x}(Sr,Ca)_xCuO_4$ with planer coordination. Therefore, we investigated the low-energy spin dynamics via ^{139}La-nuclear magnetic resonance measurements of LESCO.

In Fig. 1, the spin-lattice relaxation rate ($1/T_1$) and the electrical resistivity (ρ) are plotted for the as-sintered compound as a function of inverse temperature [1]. The compound was a non-superconductor and exhibited spin-glass behavior at low temperatures. Similar temperature dependence can be observed for two parameters. Considering the relations of $\rho \propto \exp(E_g/k_BT)$ and $1/T_1 \propto \exp(2J/k_BT)$, we evaluated that $2J/k_BT = 7.8 \pm 0.7$ and $E_g/k_BT = 6.0 \pm 0.1$. The comparable values of $2J$ and E_g suggest that the energy of the transport gap (E_g) and the characteristic energy of the spin dynamics ($2J$) in the as-sintered compound is nearly the same. Therefore, the charge and spin dynamics could be coupled with each other.

A comparable energy scale of E_g and $2J$ are reported for the lightly doped $La_{2-x}Sr_xCuO_4$ (LSCO). The low-energy spin dynamics is governed by hole mobility; that is, the spin fluctuations slow down owing to the localization of mobile carriers when the temperature is lowered. The inset in Fig. 1 shows two values for the LESCO located nearly the extrapolated positions for LSCO, suggesting a similar mechanism in suppressing low-energy spin dynamics. This spin fluctuations disappear when superconductivity emerges owing to oxidation annealing, indicating a drastic variation in spin correlations associated with metal-insulator transition.

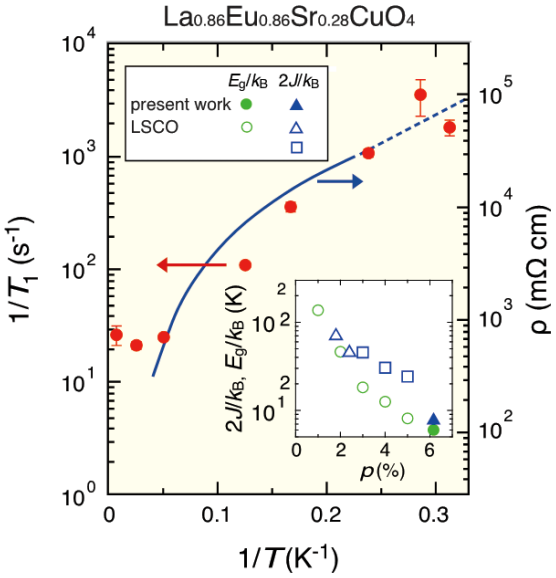

Fig. 1 $1/T$ dependence of $1/T_1$ (red circles: spin-lattice relaxation rate) and ρ (blue line: electrical resistivity) in as-sintered $La_{0.86}Eu_{0.86}Sr_{0.28}CuO_4$ (LESCO). Inset represents $2J/k_B$ and E_g/k_B for LESCO and $La_{2-x}Sr_xCuO_4$.

References

[1] T. Taniguchi, S. Kitagawa, K. Ishida, S. Asano, K. Kudo, M. Takahama, P. Xie, T. Noji, and M. Fujita, J. Phys. Soc. Jpn. **91**, 074710 (2022).

Masaki Fujita (Quantum Beam Materials Physics Research Laboratory)
E-mail: fujita@tohoku.ac.jp
URL: http://qblab.imr.tohoku.ac.jp/index-e.html

Electric Quadrupolar Correlation in the Frustrated Quantum Magnet $Tb_2Ti_2O_7$

Geometrically frustrated systems have been serving as a fertile ground for studying nontrivial magnetic phenomena. The pyrochlore lattice is a prototypical structure having geometrical frustration. Among the various pyrochlore materials, $Tb_2Ti_2O_7$ shows unique magnetic properties because Tb^{3+} ions have an electric quadrupole. Here, we investigated the quadrupole correlation in Tb-rich $Tb_2Ti_2O_7$ by measuring the elastic constant and magnetostriction.

In $Tb_2Ti_2O_7$, Tb^{3+} ions have a total angular momentum J = 6. The trigonal crystalline electric field partially lifts the degeneracy and produces a low-energy level scheme, that consists of ground-state and first-excited doublets separated by an energy gap of only ≈ 18 K. In addition to a magnetic dipole moment, these doublets carry a large electric quadrupolar moment, which couples to the local strain. Recently, the quadrupole order was determined to be approximately 0.5 K for Tb-rich $Tb_2Ti_2O_7$ crystals. These findings imply that the quadrupolar moment plays an important role in this system. Thus, this system can be viewed as a frustrating system with electric quadrupole degree of freedom. To probe the correlation of the electric quadrupole, we measured the elastic constant and magnetostriction and compared the experimental results with the calculation based on a single-ion model [1].

Figure 1 shows the experimentally observed and calculated magnetostriction based on a single-ion model at various temperatures. Although the calculation reproduced experimental data above 10 K, a discrepancy was observed between the calculated and experimental data in the lower temperature region. This observation implies the evolution of electric quadrupole correlation below 10 K. A similar conclusion was obtained for the elastic constant experiment.

Figure 2 shows the magnetic phase diagram in Tb-rich $Tb_2Ti_2O_7$. While the orbital ordering is observed at the low-temperature (T<0.4 K) and low-magnetic-field region, a strong quadrupole correlation exists in the higher temperature and higher magnetic-field region (the cyan-colored region in Fig. 2). The evolution of correlation seems to be induced by the geometrical frustration in this system.

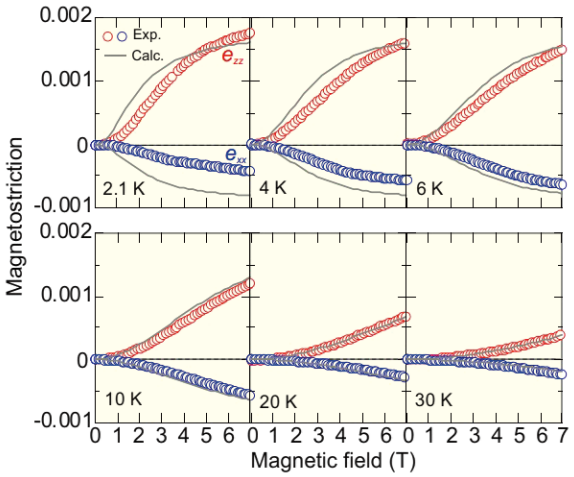

Fig. 1 Magnetostriction at various temperatures [1]. The calculations based on a single-ion model are also plotted for comparison.

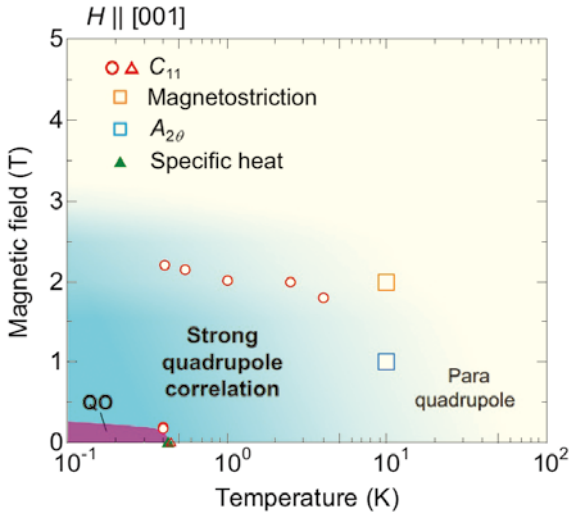

Fig. 2 Magnetic phase diagram in Tb-rich $Tb_2Ti_2O_7$ [1].

References

[1] Y. Nii, Y. Hirokane, S. Nakamura, N. Kabeya, S. Kimura, Y. Tomioka, T. Nojima, and Y. Onose, Phys. Rev. B **105**, 094414 (2022).

Yoshinori Onose (Quantum Functional Materials Physics Research Laboratory)
E-mail: yoshinori.onose.b4@tohoku.ac.jp
URL: http://www.imr.tohoku.ac.jp/en/about/divisions-and-centers/research-division/08.html

Development of Optical-Guiding Crystal Scintillators for High-Resolution Radiation Imaging

A novel optical-guiding crystal scintillator and its fabrication method were developed. The scintillator consists of a halide single-crystal scintillator core and glass clad. The scintillation light generated in the core with an angle greater than the critical angle is completely reflected at the interface with the glass, thereby functioning as an optical waveguide such as an optical fiber. Owing to the light guiding system, the optical-guiding crystal scintillator shows high sensitivity and high spatial resolution for radioactive particles.

Scintillators coupled with photodetectors are widely used in radiation imaging applications such medical imaging, security, high-energy physics, astrophysics, and oil-well logging. In X-ray imaging applications, radiation imaging sensors are composed of photodetector arrays coupled with a scintillator plate. Here, we propose a novel optical-guiding crystal scintillator (OCS). It consists of a halide single-crystal scintillator core such as Tl-activated CsI (Tl:CsI), Eu-doped SrI_2 (Eu:SrI_2) scintillators with a borosilicate glass clad. The scintillation light that is generated with an angle greater than the critical angle is completely reflected at the interface with the glass, functioning as an optical waveguide such as optical and scintillating fibers (Fig.1-left). Here, the critical angles of Tl:CsI (nD=1.78) and Eu:SrI_2 (nD=2.05) with borosilicate glass-type (nD=1.47) OCSs were calculated to be as small as 55.7° and 45.8°, respectively. Figure 1-right shows the photograph of OCS fiber scintillators under ultraviolet (UV) irradiation at an edge that was cut from the side of a fabricated fiber with a total length of approximately 200–300 m. The light generated after UV irradiation is light guided to the other side of the fibers. Figure 2 shows micrographs of an OCS fiber. The central scintillator crystal fiber was covered by glass. An OCS fiber with a minimum core diameter of 15.4 μm with 5.1 μm thick clad was obtained. Figure 3 shows the photographs and backscattered electron image (BEI) of a 1 mm thick bundled OCS plate. The image from the top shows several fiber scintillators of 30 μm diameter bundled together. Figure 4 shows a BEI of the bundled OCS plate and corresponding electron backscattered diffraction images. The scintillator cores were single grains. Position resolution was evaluated using the plate and α-ray. The full width at half maximum (spatial resolution) was 37.2 μm. The obtained spatial resolution was equivalent to that of the core diameter. Owing to the light guiding system, the bundled OCS plate exhibited high spatial resolution for radioactive particles.

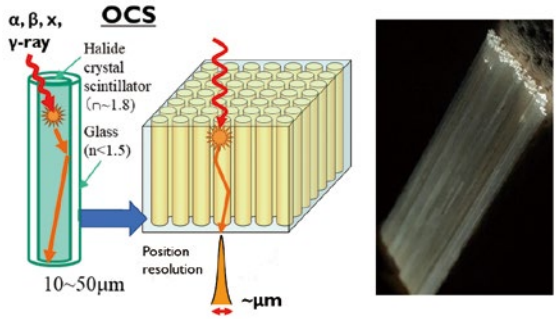

Fig. 1 Schematic of optical-guiding crystal scintillator (OCS) (left) and the photograph of OCS fibers under ultraviolet excitation (right).

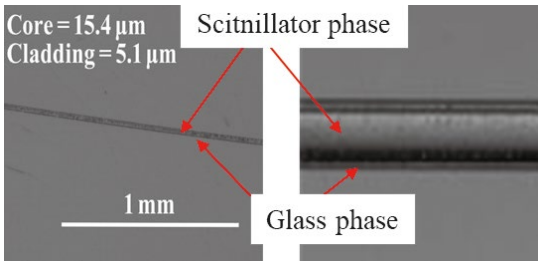

Fig. 2 Micrographs of OCS fibers

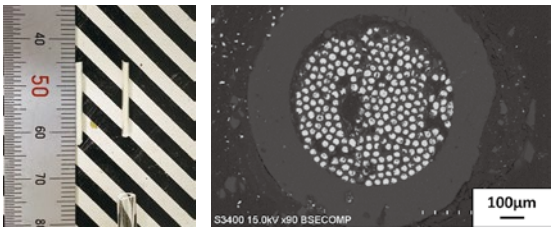

Fig. 3 Photograph of bundled OCS (left), 1 mm thick bundled OCS plate (right)

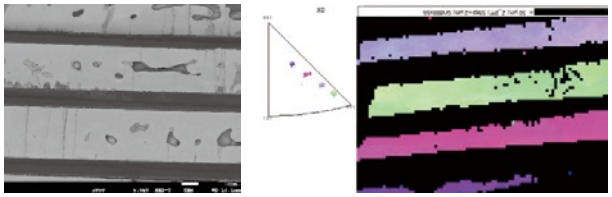

Fig. 4 Backscattered electron mage of the bundled OCS plate and corresponding electron backscatter diffraction.

References

[1] R. Yajima *et al.*, Ceramic International (2023) in press.

Akira Yoshikawa (Advanced Crystal Engineering Research Laboratory)
E-mail: akira.yoshikawa.d8@tohoku.ac.jp
URL: http://yoshikawa-lab.imr.tohoku.ac.jp/index-e.html

Nonthermal Melting of Charge Density Wave Order in VTe_2

Ultrafast phase control of materials by femtosecond laser pulses is expected to be a significantly crucial technique for future photonic devices such as phase change materials. In this work, the ultrafast optical response of VTe_2, a typical transition-metal dichalcogenide showing the charge density wave (CDW), was investigated. We clarified the mechanism and timescale of photoinduced phase transition in VTe_2 originating from the melting of the CDW order.

Photoexcitation of semiconductor materials using femtosecond lasers can induce a nonthermal ultrafast phase transition, which is primarily dominated by electron excitations [1]. This process is called as photoinduced phase transition (PIPT). In the research field of PIPT, transition-metal dichalcogenides (TMDCs) are fascinating targets owing to their distorted crystal structure originating from a charge density wave (CDW). The PIPT from a CDW to non-CDW phase is called "CDW melting," and researchers have reported CDW melting in several TMDCs so far [2,3].

In this work, we investigated the mechanism of CDW melting in VTe_2, a typical TMDC, which exhibits a CDW phase below 480 K, using ultrafast optical spectroscopy (UOS) [5]. UOS generally enables us to investigate the ultrafast optical response of materials by measuring a transient reflectivity change as a function of elapsed time. A unique feature of our measurement system is the use of white light as the probe light, using which we can simultaneously observe the reflectivity changes over a wide range of wavelengths. The wavelength of pump light used here was 800 nm. A single-crystal sample was grown using the Bridgman method. A clean (110) surface was prepared using the Scotch-tape method, and it was mounted on a thermo/cryostat. UOS was performed at a sample temperature of 78 K.

Figure 1 shows the UOS responses after pumping different excitation fluences (F), which was monitored using a 500 nm probe. At each fluence, the reflectivity decreased just after photoexcitation, and the degree of decrease was greater at a higher F. The oscillation during reflectivity change is called "coherent optical phonon" (COP), originating from nonthermal atomic oscillations induced by electron excitation. As the frequencies of COP coincide with those of the all-symmetric Raman active modes of substances, the oscillation analysis enables us to identify the (CDW or non-CDW) phases of VTe_2. The inset of Figure 1 shows the fast Fourier transforms of the time derivative of reflectivity changes. At the lower F range (F < 1.21 mJ cm^{-2}), two modes are observed at around 1.6 and 2.5 THz; these are attributed to the CDW phase, indicating that the CDW phase of VTe_2 remained even after the lower fluence excitation. At a higher F range (F ≧1.21 mJ cm^{-2}), a new mode can be observed at approximately 4.4 THz. This mode can be attributed to the A_{1g} mode of the non-CDW phase. A simple evaluation of the sample temperature after excitation on the adiabatic condition indicated that the temperature did not exceed the transition temperature in the F range used in this study. Thus, we clearly observed that the CDW melting of VTe_2 proceeds in a nonthermal manner within an ultrashort time duration (picosecond order). In addition to the previous literature employing ultrafast electron diffraction method for VTe_2 [4], our recent UOS study [5] has accumulated more detailed information on the transformation mode and time scale of PIPT in VTe_2.

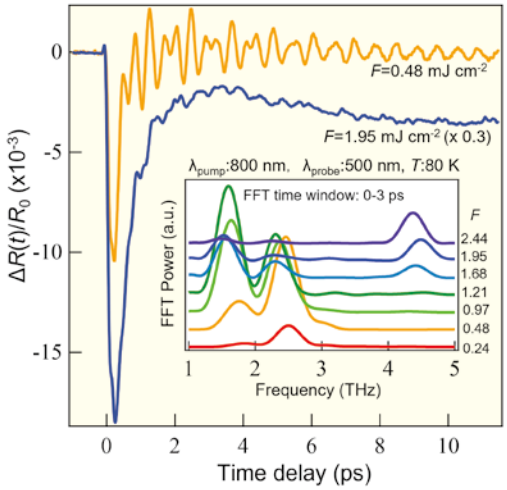

Fig. 1 Transient reflectivity changes after photoexcitation as functions of elapsed time monitored by 500 nm probe. The inset indicates fast Fourier transform (FFT) results of time derivative of reflectivity change. The FFT time range is from 0 to 3 ps.

References

[1] S. K. Sundaram and E. Mazur, Nat. Mater. **1**, 217 (2002).
[2] E. Möhr-Vorobeva, S. L. Johnson, P. Beaud, U. Staub, R. De Souza, C. Milne, G. Ingold, J. Demsar, H. Schaefer, and A. Titov, Phys. Rev. Lett. **107**, 036403 (2011).
[3] J. Lee, J. Bang, and J. Kang, J. Phys. Chem. Lett. **13**, 5711 (2022).
[4] A. Nakamura, T. Shimojima, Y. Chiashi, M. Kamitani, H. Sakai, S. Iwashita, H. Li, and K. Ishizaka, Nano Lett. **20**, 4932 (2020).
[5] H. Tanimura, N. L. Okamoto, T. Homma, Y. Sato, A. Ishii, H. Takamura, and T. Ichitsubo, Phys. Rev. B **105**, 245402 (2022).

Hiroshi Tanimura (Structure-Controlled Functional Materials Research Laboratory)
E-mail: hiroshi.tanimura.b7@tohoku.ac.jp
URL: http://ilab.imr.tohoku.ac.jp/

Host–Guest Electron Transfer Mechanism for Magnetism Manipulation

In porous materials, the host–guest electron transfer (HGET) mechanism, which affects both the electronic structure and spin states of the host framework, is an effective tool for manipulating physical properties. We successfully demonstrated a reversible magnetic phase change between an antiferromagnet and a paramagnet by exposing or evacuating I_2 as a guest molecule, which is based on the HGET mechanism in a charge-variable layered porous magnet.

Host–guest electron transfer (HGET) in molecular framework systems, such as metal–organic frameworks (MOFs), is a critical trigger for implementing drastic changes in both the host framework and the guest, and can enable the possible modulation of the electronic and magnetic properties of frameworks. Post-synthetic incorporation of redox-active guests into redox-active MOFs is a fascinating strategy for achieving guest-driven reversible HGET. However, demonstrating a reversible phase change related to magnetic and electronic long-range ordering is a significant challenge [1].

In this study, a porous magnetic MOF, [{Ru_2(2,6-F_2PhCO_2)$_4$}$_2$(BTDA-TCNQ)] (**1**), where 2,6-$F_2PhCO_2^-$ and BTDA-TCNQ represent 2,6-difluorobenzoate and bis[1,2,5]dithiazolotetracyanoquinodimethane, respectively, was synthesized, which showed a HGET-induced magnetic phase change using I_2 as a redox-active guest [2]. Pristine porous compound **1** was post-synthetically transformed into [{Ru_2(2,6-F_2PhCO_2)$_4$}$_2$(BTDA-TCNQ)]I_3 (**1-I_3**) via I_2 vapor treatment. Notably, compound **1** was recovered reversibly via a crystal-to-crystal transformation upon evacuation of the I_2-adsorbed solid sample **1-I_3** at 100 °C (Fig. 1). The pristine guest-free compound **1** was an antiferromagnet with a Néel temperature of 90 K (= T_N) (Fig. 2) due to the presence of interlayer antiferromagnetic interactions between ferrimagnetically ordered layers with a [{$Ru_2^{II,III}$}$^+$–(BTDA-TCNQ)$^{\bullet-}$–{$Ru_2^{II,II}$}^{0}]$_\infty$ composition (Fig. 1), in which [$Ru_2^{II,III}$]$^+$, [$Ru_2^{II,II}$], and BTDA-TCNQ$^{\bullet-}$ possess spin states of S = 3/2, 1, and 1/2, respectively, whereas the I_2-exposed **1-I_3** compound transformed into a paramagnet with the formula of [{$Ru_2^{II,III}$}$^+$–(BTDA-TCNQ)^0–{$Ru_2^{II,III}$}](I_3^-) (Fig. 1), demonstrating the occurrence of HGET expressed as BTDA-TCNQ$^{\bullet-}$ + 3/2(I_2) → BTDA-TCNQ^0 + I_3^-. This HGET in the MOF pores resulted in the paramagnetic behavior of **1-I_3** (Fig. 2) with isolated spin sets of S = 3/2 and 1 for [$Ru^{II,III}_2$]$^+$ and [$Ru^{II,II}_2$], respectively.

Notably, the **1-I_3** paramagnet, despite containing a neutral BTDA-TCNQ moiety, exhibited

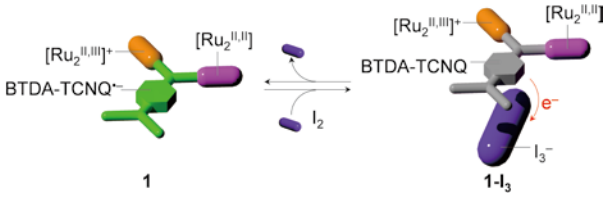

Fig. 1 Formula units schematics for the guest-free compound **1** and I_2-adsorbed compound **1-I_3**.

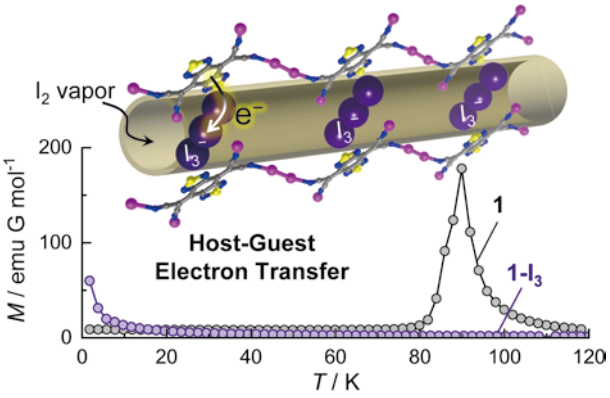

Fig. 2 Temperature dependence of field-cooled magnetization curves measured at 100 Oe for **1** (gray) and **1-I_3** (purple).

a hundred-fold increase in electrical conductivity when compared to that of compound **1** after I_2 adsorption. This could be due to the hopping electronic transfer between partially charge-delocalized [Ru_2] units ([Ru(1)$_2$]$^{(1-\delta)+}$ and [Ru(2)$_2$]$^{\delta+}$ units ($\delta \approx 0.2$)) via the neutral BTDA-TCNQ moiety, as confirmed by theoretical calculations. This work demonstrates the first investigation of magnetic phase switching and electronic modulation via HGET in a porous magnetic MOF. The proposed HGET strategy will not only pave a new path toward the development of chemo-responsive magnets, but will also facilitate extensive applications as a new class of memories, sensors, and switches.

References

[1] H. Miyasaka, Bull. Chem. Soc. Jpn. **94**, 2929 (2021).
[2] J. Zhang, W. Kosaka, Y. Kitagawa, and H. Miyasaka, Angew. Chem. Int. Ed. **61**, e202115976 (2022).

Jun Zhang and Hitoshi Miyasaka (Solid-State Metal-Complex Chemistry Research Laboratory)
E-mail: zhangjun@imr.tohoku.ac.jp, hitoshi.miyasaka.e7@tohoku.ac.jp
URL: http://www.miyasaka-lab.imr.tohoku.ac.jp/cn5/HOME-Eng.html

Observation of Large Antisymmetric Interlayer Exchange Coupling in Synthetic Antiferromagnet with Wedge-Shaped Layers

Antisymmetric interlayer exchange coupling (AIEC) plays pivotal roles in the magnetization switching of a synthetic antiferromagnet by inducing magnetization canting. We observed a large AIEC for perpendicularly magnetized Pt/Co/Ir/Co/Pt with wedge-shaped layers. The effective field of the AIEC is related to the symmetric interlayer exchange coupling, providing guides to enhance the AIEC. We also demonstrated that perpendicular magnetization can be switched solely by applying an in-plane magnetic field owing to a large AIEC.

Interlayer exchange coupling (IEC) has been widely studied since the 1980s in various metallic superlattices. The symmetric IEC energy is expressed as $J_{AF}(\mathbf{m}_1 \cdot \mathbf{m}_2)$, where J_{AF} denotes the antiferromagnetic coupling strength, and $\mathbf{m}_1$ and $\mathbf{m}_2$ represent the magnetization vectors of two ferromagnets separated by a nonmagnet. The symmetric IEC aligning $\mathbf{m}_1$ and $\mathbf{m}_2$ in antiparallel provides a synthetic antiferromagnet.

Recently, antisymmetric IEC (AIEC) was reported in metallic superlattices when the in-plane spatial inversion symmetry was broken [1,2]. The AIEC energy is expressed as $\mathbf{D}_{AIEC} \cdot (\mathbf{m}_1 \times \mathbf{m}_2)$, where $\mathbf{D}_{AIEC}$ is the AIEC vector determined by the system symmetry. Thus, the AIEC cants the magnetizations in the two ferromagnetic layers, which leads to chiral magnetic configurations. However, the controllability and applicability of AIEC have not yet been examined, and the systematic experiments exploiting well-controlled in-plane structural asymmetry are indispensable.

We exploited the wedge-shaped layers to intentionally break the in-plane spatial inversion symmetry, and investigated the AIEC for the perpendicularly magnetized Pt/Co/Ir/Co/Pt with wedge-shaped layers to clarify the nature of AIEC [3]. A double-wedged sample (DWS) of Ta (1)/Pt (2)/Co (t_{Co})/Ir (t_{Ir})/Co (0.5)/Pt (2)/Ta (1) (thickness in nanometers) was deposited on a SiO_x substrate. The values of t_{Co} and t_{Ir} were continuously varied from 0.6 to 1.6 nm and from 0 to 1.5 nm, respectively. The wedge direction of the Ir layer was orthogonal to that of the wedged Co layer at the bottom, as illustrated in Fig. 1a. DWS was patterned into Hall-bar-shaped devices, and the magnetic properties were investigated by exploiting the anomalous Hall effect (AHE). The AHE curves exhibited the periodic variation in the saturation field ($\mu_0 H_s$) against t_{Ir}, indicating a symmetric IEC between two Co layers. The AHE curves were significantly shifted by applying an additional in-plane magnetic field ($\mu_0 H_{ip}$) of 50 mT (Fig. 1b), indicating the existence of

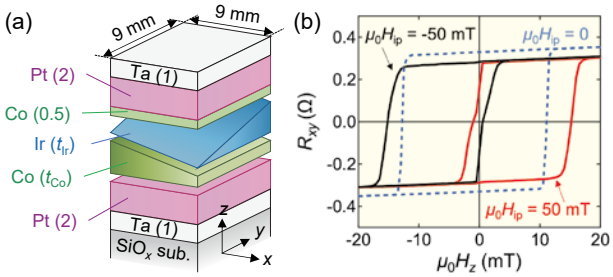

Fig. 1 (a) Illustration of double-wedged sample (DWS). (b) Anomalous Hall effect curves without $\mu_0 H_{ip}$ (blue) and with $\mu_0 H_{ip}$ (red and black) for DWS at t_{Co} ~ 0.80 nm and t_{Ir} ~ 0.27 nm.

AIEC. The largest switching field shift ($\mu_0 \Delta H_{sw}$) was 14.8 mT at t_{Co} = 0.80 nm and t_{Ir} = 0.27 nm, which was an order of magnitude larger than the values reported previously (0.7–1.7 mT [1,2]). Similar to the t_{Ir} dependence of $\mu_0 H_s$, $\mu_0 \Delta H_{sw}$ showed the oscillatory change against t_{Ir}, suggesting that the effective field of AIEC is related to the symmetric IEC. Moreover, we experimentally demonstrated the perpendicular magnetization switching solely induced by $\mu_0 H_{ip}$ via the AIEC. This study provides crucial information to manipulate three-dimensional chiral magnetic structures utilizing the AIEC.

References

[1] D.-S. Han, K. Lee, J.-P. Hanke, Y. Mokrousov, K.-W. Kim, W. Yoo, Y. L. W. van Hees, T.-W. Kim, R. Lavrijsen, C.-Y. You, H. J. M. Swagten, M.-H. Jung, and M. Kläui, Nat. Mater. **18**, 703 (2019).

[2] A. Fernández-Pacheco, E. Vedmedenko, D. Petit, and R. P. Cowburn, Nat. Mater. **18**, 679 (2019).

[3] H. Masuda, T. Seki, Y. Yamane, R. Modak, K. Uchida, J. Ieda, Y. C. Lau, S. Fukami, and K. Takanashi, Phys. Rev. Appl. **17**, 054036 (2022).

Takeshi Seki (Magnetic Materials Research Laboratory)
E-mail: takeshi.seki@tohoku.ac.jp
URL: http://magmatelab.imr.tohoku.ac.jp/

Fermi Surfaces of Spin-Triplet Superconductor UTe_2 Unveiled by Quantum Oscillations

Quantum oscillations (de Haas–van Aphen oscillations) were successfully observed for the first time in the spin-triplet superconductor UTe_2 using ultra-clean single crystals grown by the flux method. Two types of cylindrical Fermi surfaces with strong corrugations were detected. The experimental results were in good agreement with those of band calculations considering the onsite Coulomb repulsion U. The detected cyclotron effective masses were significantly large, ranging from 32 to 57 m_0, revealing the heavy electronic states that play a dominant role in unusual superconducting properties.

UTe_2 is one of the hottest materials in condensed matter physics [1]. Superconductivity was observed at 1.6-2 K without magnetic ordering at very low temperatures. The most remarkable feature is the field-robust superconductivity, revealing field-reentrant superconductivity up to 35 T, when the field is applied along the hard-magnetization b-axis in an orthorhombic structure. Another spectacular event is the multiple superconducting phases that can be observed under pressure and a magnetic field, indicating the different superconducting order parameters [2]. These properties are consistent with a scenario for spin-triplet superconductivity, which is also an informative field of research for studying topological superconductivity.

To understand this fascinating superconducting mechanism, the electronic states must be experimentally clarified. We succeeded in growing ultra-clean single crystals of UTe_2 using the NaCl/KCl-flux method, and clearly detected the quantum oscillations, that is, the de Haas–van Alphen (dHvA) oscillations for the first time [3]. Figure 1(a) shows the dHvA oscillations when the field is tilted from the c- to a-axis. Clear dHvA oscillations appeared above the superconducting upper critical field, H_{c2}, which are denoted by the arrows pointing upward. The angular dependence of the dHvA frequencies are shown in Fig. 1(b). The frequencies increase with field angle, indicating two types of corrugated cylindrical Fermi surfaces, as shown in the inset of Fig.1(b). The experimental results are in good agreement with the results of band calculations with the Coulomb repulsion U (U=2eV). The detected cyclotron effective masses were significantly large, ranging from 32 to 57 m_0, where m_0 is the rest mass of electron, which is in agreement with the heavy electronic states as well as the mixed valence states of UTe_2.

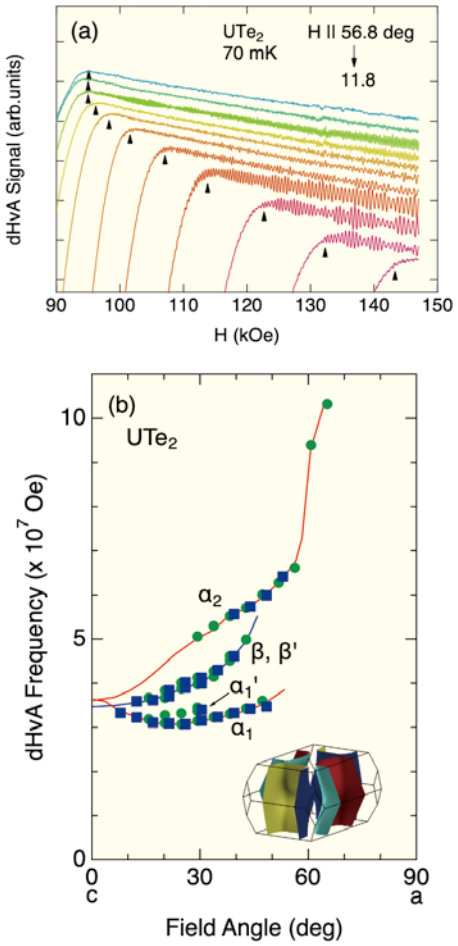

Fig.1 (a) de Haas–van Alphen (dHvA) oscillations at different field angles tilted from H II c to a-axes in UTe_2. (b) Angular dependence of dHvA frequencies and the calculated Fermi surfaces in UTe_2.

References

[1] D. Aoki, J. P. Brison, J. Flouquet, K. Ishida, G. Knebel, Y. Tokunaga, and Y. Yanase, J. Phys. Condens. Matter **34**, 243002 (2022).

[2] H. Fujibayashi, G. Nakamine, K. Kinjo, S. Kitagawa, K. Ishida, Y. Tokunaga, H. Sakai, S. Kambe, A. Nakamura, Y. Shimizu, Y. Homma, D. Li, F. Honda, and D. Aoki, J. Phys. Soc. Jpn. **91**, 043705 (2022).

[3] D. Aoki, H. Sakai, P. Opletal, Y. Tokiwa, J. Ishizuka, Y. Yanase, H. Harima, A. Nakamura, D. Li, Y. Homma, Y. Shimizu, G. Knebel, J. Flouquet, and Y. Haga, J. Phys. Soc. Jpn. **91**, 083704 (2022).

Dai Aoki (Actinide Materials Science Research Laboratory)
E-mail: dai.aoki.c2@tohoku.ac.jp
URL: http://www.imr.tohoku.ac.jp/en/about/divisions-and-centers/research-division/25.html

Building of Si and Si/SiC Composite Materials by Electron Beam Additive Manufacturing

We successfully fabricated Si and Si/SiC composite materials for the first time using electron beam additive manufacturing (EBM). As Si and Si/SiC are non-metals and have high electrical resistance, manufacturing these materials has been challenging. This successful case is a result that expands the possibilities of EBM.

Si and Si/SiC composite materials are primarily used in the field of semiconductor production equipment, the use of additive manufacturing is desired for the development of these materials.

Electron beam additive manufacturing (EBM) is a high-temperature vacuum process that enables manufacturing with less defect formation and oxidation contamination, and is suitable for manufacturing Si-based materials, which are brittle and require high purity. However, the biggest problem is the phenomenon called "smoking," in which the powder bed can scatter and disappear similar to smoke owing to the charge-up of electrons.

The smoking phenomenon is related to the bulk properties of the powder, dielectric properties of the surface oxide film [1], and number of contact points between the powders (coordination number [2]). As Si-based materials are semi-metallic materials and have high electrical resistance, manufacturing them using EBM is considered to be difficult.

Our research team measured the electrical resistance of the powder and confirmed that the electrical properties of the Si powder are at a level that can be built. Moreover, by adding Si to the SiC powder to create a Si/SiC composite material powder, the electrical properties of the Si/SiC composite material were confirmed to be at the same level as that of Si (Fig. 1).

We built the above material and succeeded in producing a cylindrical sample of 10 mm ϕ×10 mm. These samples exhibited significantly few internal defects and were composed of high-density objects with a relative density (which is the ratio of the measured density to the theoretical density) close to 100%. In the Si/SiC composite material, SiC particles were uniformly dispersed in the Si matrix, which is considered to be a structure obtained by the rapid solidification characteristic of the EBM (Fig. 2).

This result is a breakthrough that modifies the conventional wisdom that the EBM method can only be used for metal powders, and is considered to be a successful case that is expected to significantly contribute to technological progress.

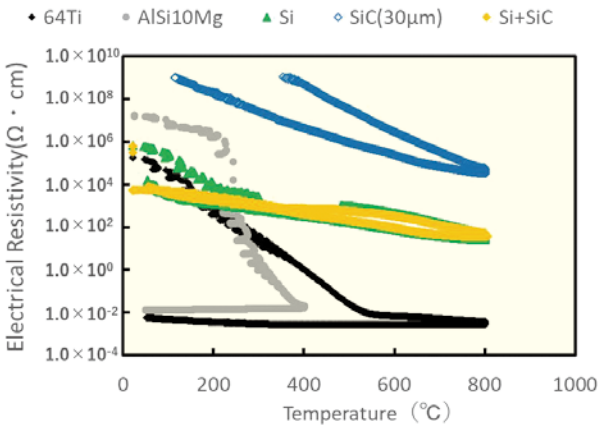

Fig. 1 Plot of electrical resistivity of powder for electron beam additive manufacturing versus time.

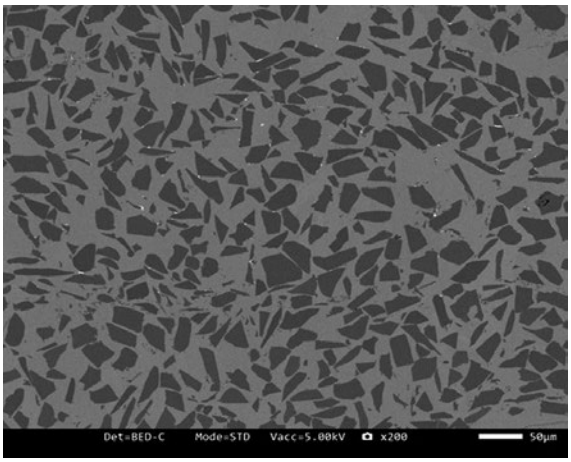

Fig. 2 Scanning electron microscopy-backscattered electron image of Si/SiC composite material.

References

[1] A. Chiba, Y. Daino, K. Aoyagi, and K. Yamanaka, Materials **14**, 4662 (2021).

[2] S. Yim, H. Bian, K. Aoyagi, K. Yamanaka, and A. Chiba, Addit. Manuf. **51**, 102634 (2022).

Takayuki Ishii and Akihiko Chiba (Tokyo Electron Additive Manufacturing for Multimaterials Research Laboratory)
E-mail: takayuki.ishii.q4@dc.tohoku.ac.jp, akihiko.chiba.d3@tohoku.ac.jp
URL: http://www.imr.tohoku.ac.jp/en/about/divisions-and-centers/research-division/31.html

Research Centers

IMR KINKEN Research Highlights 2023

High Thermal Conductivity in Wafer-Scale Cubic Silicon Carbide Crystals

International Research Center for Nuclear Materials Science

An isotropic high thermal conductivity exceeding 500 W/m·K at room temperature in high-quality wafer-scale cubic SiC (3C-SiC) crystals was reported, which is the second highest among large crystals (only surpassed by diamond). Furthermore, the thermal conductivity of 3C-SiC films was even higher than that of diamond thin films of equivalent thickness.

SiC plays a fundamental role in power electronics, optoelectronics, and quantum computing. In the field of power electronics, SiC-based power devices demonstrate significant potential for replacing Si-based technology owing to its fast-switching speeds, low losses, and high breakdown voltage. SiC can be in the form of multiple types of crystals with different atomic arrangements, such as hexagonal (4H, 6H, etc.) and cubic (3C) structures. The hexagonal 4H-SiC and 6H-SiC have been widely developed and commercialized. Cubic-structured 3C-SiC has a relatively simple crystal structure; therefore, it is expected to exhibit high thermal conductivity. However, the reported thermal conductivity (90 W/m·K) of 3C-SiC is lower than that of the structurally more complex 6H and 4H phases (320 W/m·K) and the theoretically predicted intrinsic thermal conductivity of 3C-SiC.

Here, we report a high isotropic thermal conductivity exceeding 500 W/m·K at room temperature in a high-purity wafer-scale free-standing 3C-SiC bulk crystal grown via low-temperature chemical vapor deposition [1]. The measured thermal conductivity agrees well with the intrinsic thermal conductivity of a perfect single-crystal 3C-SiC that was predicted using first-principles calculations. The in- and cross-plane thermal conductivities of the corresponding 3C-SiC thin films are measured using a beam-offset method based on time-domain thermoreflectance. The crystal structure analysis was performed via transmission electron microscopy (TEM) and X-ray diffraction.

Figures 1(a) and (b) show a high-resolution TEM image and the selected-area electron diffraction pattern of 3C-SiC, respectively. The fast Fourier Transform of the TEM image is shown in the inset of Fig. 1(a). These results confirmed the cubic phase of the 3C-SiC crystal.

Figure 1(c) shows a comparison of the measured thermal conductivity of 3C-SiC at room temperature with that of other high-thermal-conductivity crystals as a function of wafer size. The recently reported boron-based crystals exhibit high thermal conductivity;

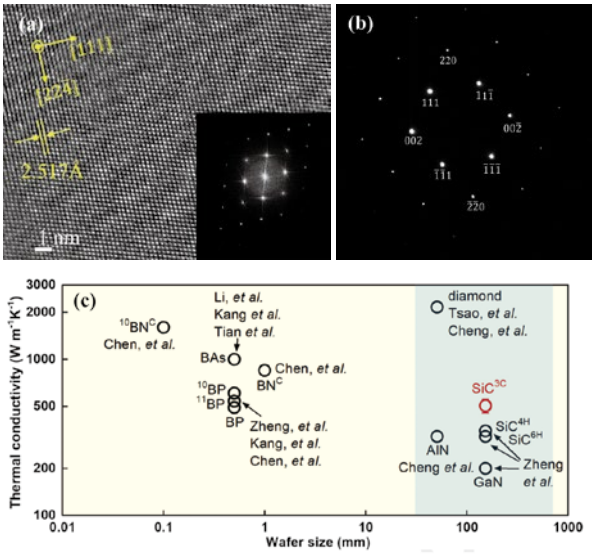

Fig. 1 (a) High-resolution transmission electron microscopy image and (b) selected-area electron diffraction pattern of cubic SiC (3C-SiC), and (c) measured thermal conductivity of 3C-SiC at room temperature is compared with those of other high-thermal-conductivity crystals as a function of wafer size.

however, only millimeter-scale or smaller crystal sizes are achievable.

The 3C-SiC wafer reported in this work can reach up to 6 inch in size with a high isotropic thermal conductivity exceeding 500 W/m·K. The measured thermal conductivity of 3C-SiC was higher than that of all other metals and the second highest among all large crystals (only surpassed by that of single-crystal diamond). The thermal conductivity of 3C-SiC at room temperature was 50% higher than that of the 6H-SiC and AlN, and 40% higher than that of the 4H-SiC.

References

[1] Z. Cheng, J. Liang, K. Kawamura, H. Zhou, H. Asamura, H. Uratani, J. Tiwari, S. Graham, Y. Ohno, Y. Nagai, T. Feng, N. Shigekawa, and D. Cahill, Nat. Comm. **13**, 7201 (2022).

Jianbo Liang (Corresponding Author, Graduate School of Engineering, Osaka Metropolitan University)
E-mail: liang@omu.ac.jp
Yasuyoshi Nagai (Head of International Research Center for Nuclear Materials Science)
E-mail: yasuyoshi.nagai.e2@tohoku.ac.jp
URL: http://www.imr-oarai.jp/en/

Fabrication and Properties of Functional Spherical Powders

Cooperative Research and Development Center for Advanced Materials

Researchers at the Cooperative Research and Development Center for Advanced Materials have studied various fabrication processes for advanced materials and explored the possibility of the application of these materials as multifunctional materials for future technologies in collaboration with global universities and research institutes. Here, the recent research and development status of the creation of spherical metallic powders and related technologies for industrial applications are highlighted.

Gas atomization involves spraying a high-pressure cooling medium, such as inert gas or water, on a molten-metal stream that is pulverized into small droplets. This technique allows the preparation of powders with spherical particles and high flowability. Gas atomization using an inert gas facilitates the synthesis of high-quality powders with superior flowability because of their clean surface [1]. However, gas atomized powders contain internal pores, and the volume of the pores is higher than that in powders formed via other techniques such as the plasma rotating electrode process, which may degrade various properties of the final product.

The Cooperative Research and Development Center introduced a new gas atomization apparatus in FY2022, as shown in Fig. 1, which is capable of higher output in the high-frequency melting section than conventional systems, enabling powder preparation of metals with high melting points of up to approximately 1600 °C.

Figures 2(a) and (b) show 3D images of particles and changes in the volume ratio of internal pores in Fe-based powders prepared via gas atomization using Ar and Ar+H_2 gas, respectively; these results were captured using synchrotron X-ray computed tomography method. The obtained particles exhibited an average diameter of 50 μm and a spherical morphology (Fig. 2(a)); moreover, we identified that mixing a small amount of hydrogen gas in an inert gas reduces the internal pores in the powder by inhibiting the formation of an oxide layer (Fig. 2 (b)) [2]. This result indicates that the possibility of using the powder as a raw material for additive manufacturing was obtained by controlling the composition of the mixed gas.

Moreover, as an example for the evaluation of supersaturated solid solution powders obtained via gas atomization, observation of nanoscale structural changes due to in situ heat treatment using transmission electron microscopy for the investigation of the aging behavior of atomized powder [3] is also in progress.

Fig. 1 Gas atomization apparatus (RQP1, MAKABE R&D Co., Ltd.)

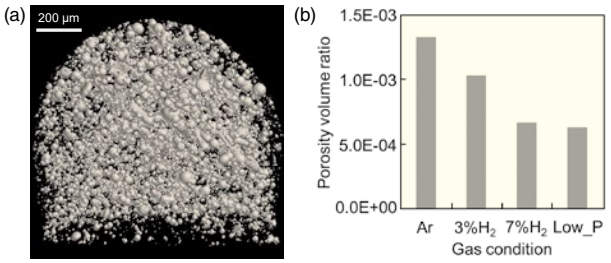

Fig. 2 (a) Three-dimensional image of atomized powder and (b) porosity volume ratio in the powders as captured using synchrotron X-ray computed tomography.

By combining these methods, the research and development of Cu-, Fe- and Ti-based functional metal powders will continue advancing.

References

[1] N. Ciftci, N. Ellendt, E. S. Barreto, L. Madler, and V. Uhlenwinkel, Adv. Powder Technol. **29**, 380 (2018).

[2] N. Yodoshi, T. Endo, and N. Masahashi, Mater. Trans. **62**, 1549 (2021).

[3] Y. Shimada, Y. Ikeda, K. Yoshida, M. Sato, J. Chen, Y. Du, K. Inoue, R. Maaβ, Y. Nagai, and T. J. Konno, J. Appl. Phys. **131**, 164902 (2022).

Mitsutaka Sato (Corresponding Author, Cooperative Research and Development Center for Advanced Materials)
E-mail: mitsutaka.sato.a3@tohoku.ac.jp
Naoya Masahashi (Head of Cooperative Research and Development Center for Advanced Materials)
E-mail: naoya.masahashi.e6@tohoku.ac.jp
URL: http://www.crdam.imr.tohoku.ac.jp/en/index-en.html

Enhancement of the Magnetoelectric Effect Using the Dynamic Jahn-Teller Effect in a Transition-Metal Complex

High Field Laboratory for Superconducting Materials

We developed a new mechanism to enhance the magnetoelectric coupling between magnetism and electric polarization, using the dynamic Jahn-Teller (JT) effect. The electric dipole, generated by the JT distortion, can be aligned by magnetic fields because of the coupling between the JT distortion and spin via the spin-orbit interaction, inducing a large electric polarization. We observed an electric polarization higher than 100 μC/m^2 owing to the second-order magnetoelectric effect in the transition metal complex, [Mn^{III}(taa)].

The magnetoelectric (ME) effect has attracted significant interest because of its potential device applications, including voltage-controllable magnetic memories [1]. The practical application of the ME effect requires improved coupling between electric polarization and magnetism. The electric dipole generated by atomic displacement can be used to improve ME coupling. We propose a new method to achieve a strong ME effect using the dynamic Jahn-Teller (JT) effect, which efficiently couples an electric dipole and spin. The atomic displacements caused by the Jahn-Teller distortion, which generates an electric dipole by lowering the symmetry of the coordination complex, can couple with spin via spin-orbit interactions. Therefore, the spin polarization generated by applying an external magnetic field causes JT distortion to align, leading to field-induced macroscopic electric polarization.

The transition metal complex [Mn^{III}(taa)], where taa is the deprotonated form of tris[1-(2-azolyl)-2-azabuten-4-yl]amine, crystallizes in the T_d point group. The C_3 symmetry of the Mn^{III} ion does not eliminate the degeneracy of the $d\gamma$ orbitals in the high-spin state and leads to JT distortion of the molecule. This JT distortion is dynamically disordered and generates a large fluctuating electric dipole (1.25 D) that reorients one direction to others on [Mn^{III}(taa)]. Its piezoelectric T_d point group allows macroscopic electric polarization (P) with external magnetic fields because of the second-order ME effect. P_z along the [001] axis, induced by a magnetic field applied in the (001) plane, can be expressed as $P_z = \beta \cdot H^2 \cdot \sin(2\theta)$, where β is the second order ME susceptibility, H the magnetic field and θ the angle between the [100] axis and magnetic field. Figure 1 shows the temperature evolution of P_z in a rotating magnetic field [2]. P_z varied with $\sin 2\theta$. The temperature dependence of P_z at $\theta = 45°$, where

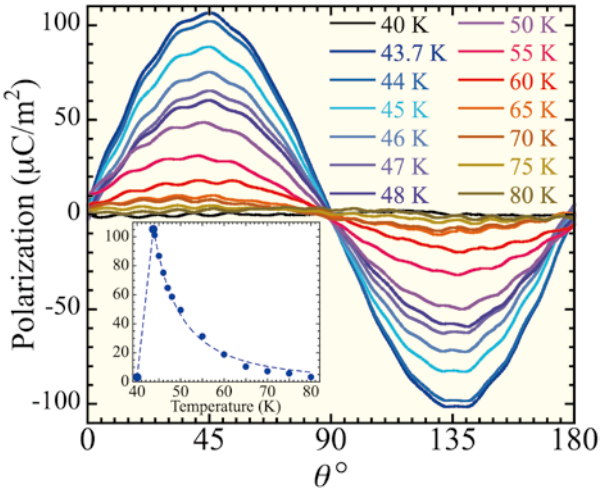

Fig. 1 Temperature evolution of the electric polarization (P_z) along the [001] axis with 15.7 T magnetic fields rotating in the (001) plane. The inset shows the temperature dependence of P_z at $\theta = 45°$.

P_z is maximum, is plotted in the inset in Fig. 1. P_z increases at lower temperatures, reaching more than 100 μC/m^2. However, it drastically decreases below 43 K as the dynamic JT distortion disappears with the spin-state transition to the low-spin state. This provides unequivocal proof that the ME effect is enhanced by the dynamic JT effect. Our procedure for enhancing the ME effect can facilitate the development of new methods for the practical use of the ME effect.

References

[1] Y. Tokura, S. Seki, and N. Nagaosa, Rep. Prog. Phys. **77**, 076501 (2014).

[2] Y. Otsuki, S. Kimura, S. Awaji, and M. Nakano, Phys. Rev. Lett. **128**, 117601 (2022).

Shojiro Kimura (Corresponding Author, High Field Laboratory for Superconducting Materials)
E-mail: shojiro.kimura.b5@tohoku.ac.jp
Satoshi Awaji (Head of High Field Laboratory for Superconducting Materials)
E-mail: satoshi.awaji.e8@tohoku.ac.jp
URL: http://www.hflsm.imr.tohoku.ac.jp/cgi-bin/index-e.cgi

Scientific Breakthrough Toward the Creation of New Industrial Materials

Trans-Regional Corporation Center for Industrial Materials Research

The Institute for Materials Research (IMR) launched the Trans-Regional Corporation Center, a comprehensive IMR-wide effort that pairs the research groups associated with IMR across the innovation spectrum to solve the current industrial challenges and transform the future global energy problems. The center was established in 2016 based on an agreement between the IMR, the Osaka Prefecture Government, and enterprises sponsored by the government, and took control of the Osaka and Kansai center projects.

The Trans-Reginal Corporation Center was established in Osaka as a special unit by the Institute for Materials Rsesearch (IMR), Tohoku University in April 2016 based on an agreement with the Osaka Prefecture Government. The Center is sponsored by the government (Ministry of Education, Culture, Sports, Science and Technology) and took charge over the Kansai Center, which was operational from 2012 to 2016. The Center has three missions. First, the Center aims to solve technical problems that industries have struggled to resolve. Second, the Center introduces academic output to industries, with the aim of applying such output to society. Third, the Center helps in the education of next-generation scientists and researchers in the field of material science. We organized a bimonthly forum named "Monodukuri Kisokoza," which focuses on special topics regarding materials and material processing. Projects are conducted through wide collaborations between the government, universities, research institutions, and other organizations. The Center has four venues to cover the Kansai and Tohoku area: the Osaka office at Osaka Prefecture University, Hyogo office at the University of Hyogo, Sendai office in IMR, and Monozukuri Business Information Center Osaka in the Creation Core Higashi-Osaka.

The Center has developed various materials under collaboration with industries and universities. One of them was the development of a novel bioactive TiNbSn alloy [1]. Figure 1 shows the scanning electron microscopy images of the anodized TiNbSn alloy, showing porous microstructures irrespective of the electrolyte compositions for anodization. The amounts of •OH measured via electron spin resonance analysis increased with ultraviolet (UV) light illumination time. Figure 2 shows the results of an antibacterial test using methicillin-resistant *Staphylococcus aureus*, meticillin-sensitive *Staphylococcus aureus*, and *Escherichia coli*, revealing that the antibacterial activity values increased with UV illumination. The values increased with UV illumination time for the anodized alloy in comparison to that of the reference (glass). The values of the anodized TiNbSn were more than 2.0 and higher than those of the glass. A clear effect of the H_2O_2 addition in the electrolyte on the anodization of the values was not found.

This study revealed that the anodized TiNbSn with a porous microstructure exhibits superior antibacterial activities, and the results correlated well with the number of hydroxyl radicals generated upon UV light illumination.

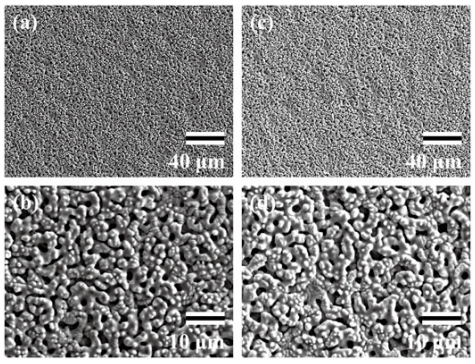

Fig. 1 Scanning electron microscopy images of the anodic oxides prepared in a sodium tartrate electrolyte with H_2O_2 (a,b) and without H_2O_2 (c,d).

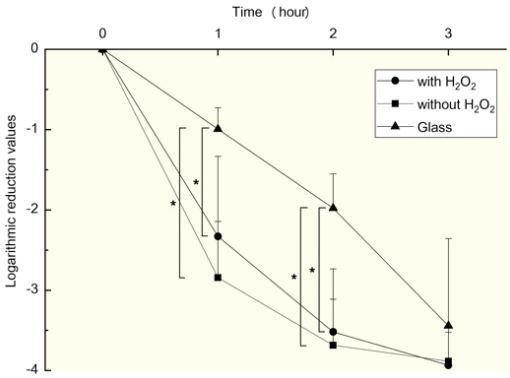

Fig. 2 Plots of logarithmic reduction values in the antibacterial tests conducted using methicillin-resistant *Staphylococcus aureus*, meticillin-sensitive *Staphylococcus aureus*, and *Escherichia coli* on the anodized TiNbSn and glass (n = 5).

Similar collaborative studies have been in progress. The Center will attempt to innovate the metallic material industry through its alliance with the partners, and promote scientific research in materials science.

References

[1] H. Kurishima, Y. Mori, K. Ishii, H. Inoue, T. Mokudai, S. Fujimori, E. Itoi, S. Hanada, N. Masahashi, and T. Aizawa, Front. Bioeng. Biotechnol. **10**, 883335 (2022).

Naoya Masahashi (Head of Trans-Regional Corporation Center for Industrial Materials Research)
E-mail: naoya.masahashi.e6@ tohoku.ac.jp
URL: http://www.imr.tohoku.ac.jp/en/about/divisions-and-centers/facilities/04.html

Gated CO_2 Adsorption Behavior in One-Dimensional Porous Coordination Polymers Based on Paddlewheel-Type Dimetal Complexes: What Determines Gate-Opening Temperatures?

Collaborative Research Center on Energy Materials

Gated CO_2 adsorption behavior was investigated in a series of one-dimensional chains based on paddlewheel diruthenium(II, II) complexes. A newly synthesized compound demonstrated gated behavior at a significantly higher temperature of 385 K under 100 kPa of CO_2 than that reported in previous research for this type of chain compounds, which usually occurred at a temperature range of 200–270 K. This specificity is ascribed to the higher topological dimensionality of pores for CO_2 accommodation that was observed in this chain.

Low-dimensional coordination polymers such as one-dimensional chains often exhibit gated guest sorption accompanying structural transition at a temperature (T_G) [1], which is associated with an external pressure induced by the guest (P_G), which is characteristic to the material and guest used. This phenomenon can be evaluated in the Clausius–Clapeyron (CC) relationship with the equation of $d(\ln P_G)/d(1/T_G) = \Delta H_G/R$, where ΔH_G and R are the transition enthalpy and gas constant, respectively. In this study, the gated CO_2 adsorption behavior was investigated in a one-dimensional chain based on a benzoate-bridged paddlewheel diruthenium(II,II) complex with a phenazine (phz) linker, $[Ru_2(p\text{-}MeOPhCO_2)_4(phz)]$ (**1**), where p-$MeOPhCO_2^-$ represents p-anisate [2].

The gas-adsorption isotherm and isobar of **1** for CO_2 were measured using an automatic volumetric adsorption apparatus connected to a cryostat system (Fig. 1a). Surprisingly, compound **1** underwent gate-opening/closing at a significantly higher T_{GC} of 385 K under P_{CO2} = 100 kPa than those previously reported for such chain compounds, which usually appeared in the temperature range of 200–270 K [3]. CC analysis resulted in a similar ΔH_G value for these compounds (inset of Fig. 1a), indicating that the transition entropy ΔS_G in each system plays a key role in shifting T_G; compound **1** results in a much smaller $|\Delta S_G|$ in the series. In situ powder/single-crystal x-ray diffraction measurement under CO_2 revealed the crystal structure of the CO_2-accommodated phase (**1⊃CO₂**, Fig. 1b). Only compound **1** produced a CO_2-accessible two-dimensional topological pore in its CO_2-adsorbed phase of **1⊃CO₂** (Fig. 1c). In contrast, the others reported previously produced one-dimensional or discrete topological pores for CO_2 accommodation.

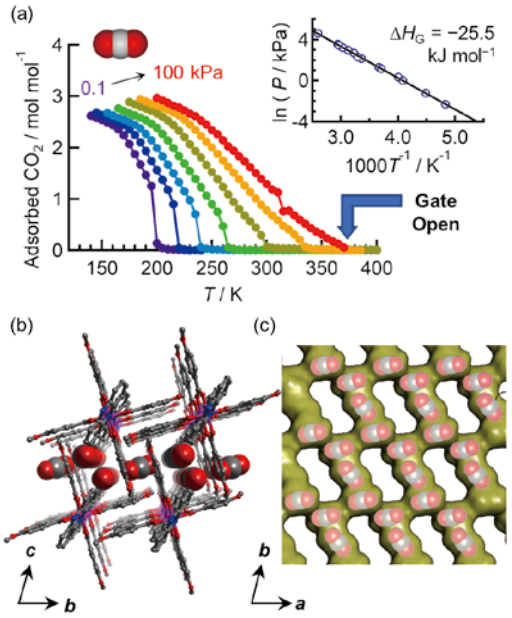

Fig. 1(a) CO_2 adsorption isobars for **1** at several CO_2 pressures measured upon cooling. (inset) Log-scale plots of CO_2 pressure versus the inverse of the gate-opening temperature (Clausius–Clapeyron analyses). (b) Views of the crystal structure of **1⊃CO₂** along a-axis. (c) Connolly surface representation of micropores (probe radius: 1.4 Å) with CO_2 adsorption sites for **1⊃CO₂**.

These findings strongly reflect the degree of freedom of CO_2 molecules in pores, which is related to ΔS_G.

References

[1] J. Zhang, W. Kosaka, and H. Miyasaka, Chem. Lett. **48**, 1308 (2019).

[2] W. Kosaka, J. Zhang, Y. Watanabe, and H. Miyasaka, Inorg. Chem. **61**, 12698 (2022).

[3] W. Kosaka, K. Yamagishi, J. Zhang, and H. Miyasaka, J. Am. Chem. Soc. **136**, 12304 (2014).

Wataru Kosaka and Hitoshi Miyasaka (Corresponding Authors, Solid-State Metal-Complex Research Laboratory)
E-mail: wataru.kosaka.c1@tohoku.ac.jp, hitoshi.miyasaka.e7@tohoku.ac.jp
Tetsu Ichitsubo (Head of Collaborative Research Center on Energy Materials)
E-mail: tichi@tohoku.ac.jp
URL: http://www.imr.tohoku.ac.jp/en/about/divisions-and-centers/facilities/05.html

Thermodynamic Stabilities and Electronic Structures of Nanoalloys

Center for Computational Materials Science

Nanoalloys are attracting considerable attention as an emerging field. Their thermodynamic stabilities and electronic structures are different from those of the bulk phase. Thermodynamic stabilities and electronic structures of nanoalloys have been clarified on the basis of first-principles calculations. The development of a computational scheme is anticipated for rapidly discovering novel nanoalloys with unique properties.

The central focus of alloy studies has been bulk systems. Recently, nanoalloys have been emerging, especially, in the field of catalysis. The thermodynamic stability of nanoalloys is known to differ from that of the bulk alloys [1]. A large degree of freedom exists in the elemental configuration within a nanoparticle (NP), and the stability of the configuration depends on the combination and composition of the constituent elements [2]. Figure 1 shows an example of predicting the stability and elemental configuration of ternary alloy under finite temperatures based on first-principles calculations combined with statistical science and machine learning. The electronic structure of constituent elements is also known to be strongly dependent on the local configuration [3]. A first-principles calculation of the model configuration of an octonary high-entropy alloy (HEA), as shown in Fig. 2(a), results in local *d*-band centers, as shown in Fig. 2(b). The *d*-band centers of surface Pt atoms (Fig. 2(c)) are drastically different from those in monometallic Pt NP (Fig. 2(d)). This indicates the emergence of unique properties in the nanoalloy that are significantly different from those of the bulk structures.

There are about 60 stable metal elements. Approximately 2,000 combinations of elements exist for binary systems, which increases up to several millions for quinary systems. When we also consider the freedom of composition, synthetic conditions, etc., the experimental exploration of such a vast material space is a daunting challenge. Therefore, the effective use of computational technologies is inevitable. Consequently, the development of a computational scheme by integrating the first-principles method, machine learning, and statistical science for the rapid screening of the thermodynamic stability and material properties is important.

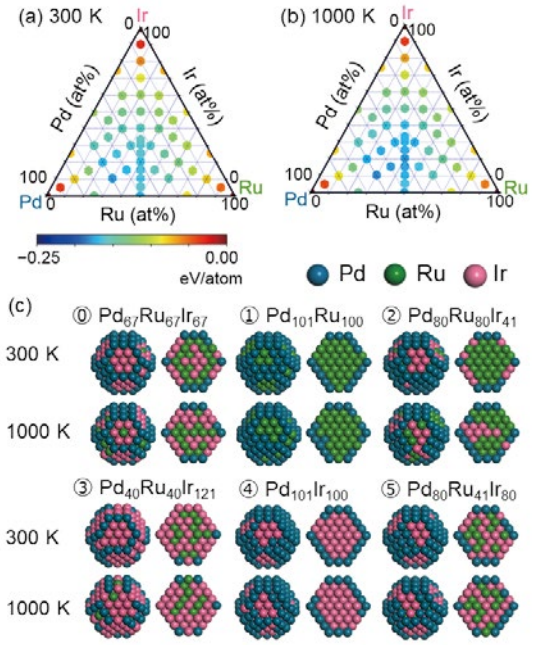

Fig. 1 Thermodynamic stability at (a) 300 and (b) 1000 K, and (c) stable PdRuIr nanoparticle (NP) configurations. Adapted with permission from [2]. Copyright 2021 The Chemical Society of Japan.

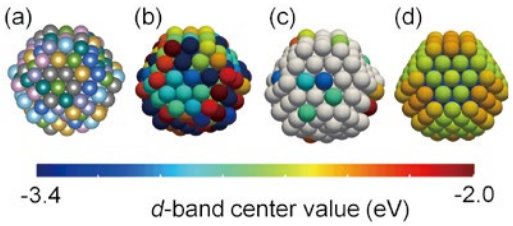

Fig. 2 (a) Density functional theory model of high-entropy alloy (HEA) NP. (b) *d*-band center map of surface atoms in HEA NP. (c) *d*-band center of the surface Pt atoms in the HEA NP. The other atoms are shown in white for visualization. (d) *d*-band center value in Pt NP. Adapted with permission from [3]. Copyright 2022 American Chemical Society.

References

[1] T. Ishimoto and M. Koyama, J. Phys. Chem. Lett. **7**, 736 (2016).
[2] Y. Nanba and M. Koyama, Bull. Chem. Soc. Jpn. **94**, 2484 (2021).
[3] D. Wu, K. Kusada, Y. Nanba, M. Koyama, T. Yamamoto, T. Toriyama, S. Matsumura, O. Seo, I. Gueye, J. Kim, L. S. R. Kumara, O. Sakata, S. Kawaguchi, Y. Kubota, and H. Kitagawa, J. Am. Chem. Soc., **144**, 3365 (2022).

Michihisa Koyama (Corresponding Author, Shinshu University)
E-mail: koyama_michihisa@shinshu-u.ac.jp
Momoji Kubo (Head of Center for Computational Materials Science)
E-mail: momoji@tohoku.ac.jp
URL: http://www.sc.imr.tohoku.ac.jp/eng/

Current Status of Collaborative Research Programs of CNSAM

Center of Neutron Science for Advanced Materials

The Center of Neutron Science for Advanced Materials is a neutron facility that focuses on research in the field of novel materials science under the Institute for Materials Research. This center manages four neutron instruments at the research reactor facility, Japanese Research Reactor (JRR)-3 and the spallation neutron source at the Japan Proton Accelerator Research Complex at the Materials and Life Science Experimental Facility. Here, we report the current status of the research program and the outcome obtained from JRR-3, where reoperations were started in 2021.

The Center of Neutron Science for Advanced Materials (CNSAM) was established in 2010 to promote novel materials science research using neutrons. CNSAM operates one diffractometer (HERMES) and two neutron spectrometers (Tohoku University Polarization Analysis Neutron Spectrometer (TOPAN) and AKANE) at the Japanese Research Reactor (JRR)-3 of the Japan Atomic Energy Agency. HERMES can determine the arrangement of atoms and spins, while their motions are examined by AKANE and TOPAN. POLANO, located at the Materials and Life Science Experimental Facility (MLF) at the Japan Proton Accelerator Research Complex, is a spectrometer designed to perform polarization analysis in higher energy regions beyond those measured using conventional triple-axis spectrometers. POLANO and TOPAN are equipped with polarized options and can disentangle nuclear and magnetic contributions. We aim to contribute to condensed matter physics and materials science using the multipurpose neutron instruments of PATH, which is a collective term for neutron instruments managed by the CNSAM.

To achieve this purpose, we established an international collaborative research program under the Institute for Materials Research from FY 2019. We provide opportunities not only for experiments with neutron beams but also for the development of neutron devices and analysis methods, and even for theoretical work using our neutron data. Proposals can be submitted under several categories, such as “Neutron experiment at MLF/JRR-3,” “Instrumental development,” “Development in analysis method,” “Structural analysis and data handling,” and “Others.” Under the category “Others,” proposals on the complementary use of neutrons and other quantum beams, such as X-ray and muon beams, are accepted. In FY 2022, we received 28 and 3 proposals from domestic and overseas researchers, respectively. Furthermore, reoperations were started at the research reactor JRR-3 in February 2021, and we received 38 proposals for the use of our neutron instrument at JRR-3 through the user program managed by the Institute for Solid State Physics, the University of Tokyo. The number of proposals is increasing annually. Moreover, the scientific results obtained using our instrument at JRR-3 are steadily being published [1-3].

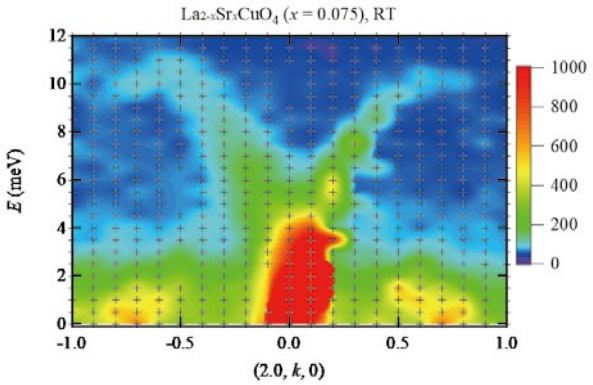

Fig. 1 Acoustic phonon branches in $La_{1.925}Sr_{0.075}CuO_4$.

After resuming operations of JRR-3, we have made efforts to improve the instrument and sample environment. Consequently, we succeeded in providing opportunities for structural analysis and investigation of spin/lattice dynamics. Figure 1 shows the inelastic neutron scattering profiles of superconducting $La_{1.925}Sr_{0.075}CuO_4$. Acoustic phonon branches around (200) Bragg position are clearly seen. Such measurements are vigorously performed by users.

References

[1] T. Taniguchi, S. Kitagawa, K. Ishida, S. Asano, K. Kudo, M. Takahama, P. Xie, T. Noji, and M. Fujita, J. Phys. Soc. Jpn, **91**, 074710 (2022).

[2] Y. Mizuguchi, Md. Riad Kasem, and Y. Ikeda, J. Phys. Soc. Jpn. **91**, 103601 (2022).

[3] Md Riad Kasem, H. Arima, Y. Ikeda, A. Yamashita, and Y. Mizuguchi, J. Phys. Mater. **5**, 045001 (2022).

Masaki Fujita (Head of Center of Neutron Science for Advanced Materials)
E-mail: fujita@tohoku.ac.jp
URL: http://nc-imr.imr.tohoku.ac.jp/index-e.html, http://qblab.imr.tohoku.ac.jp

Role of Pre-straining on Local Hydrogen Diffusivity and Hydrogen-Assisted Cracking Site in a Nitrogen-Doped Duplex Steel

International Collaboration Center

The hydrogen embrittlement behavior of nitrogen-doped ferrite/austenite duplex stainless steel was investigated in this study. Significant hydrogen embrittlement occurred, and the cracking behavior consisted of deformation twins and ferrite/austenite interfaces. Interestingly, pre-straining altered the preferential hydrogen localization and cracking sites to the ferrite grain interior. These results demonstrate the potential for the development of hydrogen-resistant high-strength steels.

The prevention of hydrogen embrittlement is an urgent issue for increasing the durability of high-strength steels for automobiles and hydrogen-energy-related infrastructures. An effective method to suppress hydrogen embrittlement is the development of new high-strength hydrogen-resistant steels. In this context, microstructure and alloy design strategies for hydrogen-resistant steels have been proposed. In particular, the introduction of austenite and addition of solute nitrogen are key to achieving high strength and superior hydrogen resistance. In this study, we characterized the hydrogen-related cracking behavior of nitrogen-doped ferrite/austenite duplex stainless steels and investigated the role of pre-straining on cracking behavior using tensile testing in conjunction with microstructural observations and a hydrogen visualization technique (Ag decoration technique).

Hydrogen charging of a nitrogen-doped duplex steel (Fe-3Mn-24Cr-1.6Mo-3.6Ni-0.4Cu-0.02C-0.27N) in an aqueous solution of 3% NaCl+3 g/L NH_4SCN at 10 A/m^2 for seven days decreased the total tensile elongation. The preferential crack initiation sites were deformation twins at the austenite and ferrite/austenite interfaces [1]. The hydrogen-induced cracking behavior was unconventional when compared to that of other ferrite/austenite duplex stainless steels without solute nitrogen.

Interestingly, 22% pre-straining of the steel achieved tensile strength of 1 GPa even with hydrogen, although the ductility decreased and the pre-strain changed the preferential crack initiation site to the ferrite interior.

Silver decoration revealed that diffusible hydrogen was preferentially located in the ferrite or grain boundaries of the undeformed steel, whereas the 22% pre-strained steel contained diffusible hydrogen in austenite. However, pre-straining suppressed the macroscopic hydrogen diffusion and local diffusion in ferrite and austenite by increasing the dislocation density. The degree of suppression of the local diffusion was more significant in ferrite than in austenite. The pre-strain effects on the cracking behavior and hydrogen diffusivity may play an important role in improving the resistance of nitrogen-doped duplex steel to hydrogen embrittlement [2].

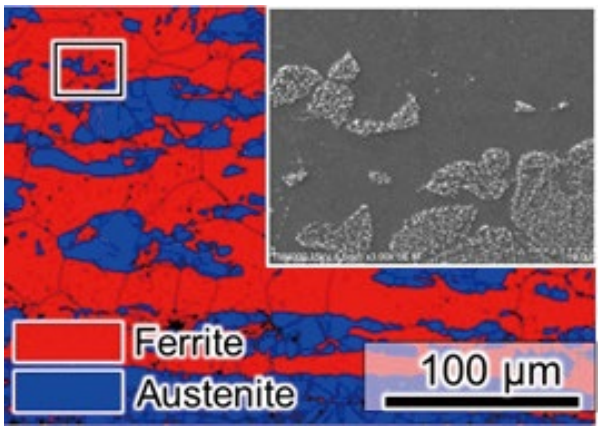

Fig. 1 Phase map and secondary electron image (inset) showing deposition of Ag particles, which corresponds to high hydrogen flux, in the hydrogen-charged duplex steel with 22% pre-strain. The location of the image shown as the inset corresponds to the area highlighted by the black square.

References

[1] M. Y. Maeda, M. Koyama, H. Nishimura, O. M. Cintho, and E. Akiyama, Int. J. Hydrog. Energy **46**, 2716 (2021).

[2] M. Y. Maeda, M. Koyama, H. Nishimura, O. M. Cintho, and E. Akiyama, Scr. Mater. **207**, 114272 (2022).

Milene Yumi Maeda (Corresponding Author, State University of Ponta Grossa)
E-mail: milenemaeda@gmail.com
Eiji Akiyama (Corresponding Author, Environmentally Robust Materials Research Laboratory)
E-mail: eiji.akiyama.d1@tohoku.ac.jp
Hiroyuki Nojiri (Head of International Collaboration Center)
E-mail: icc-imr@grp.tohoku.ac.jp
URL: http://www.icc-imr.imr.tohoku.ac.jp/

Structure of the Al_3Mn Amorphous Alloy Prepared via Magnetron Sputtering

Center for Advanced Light Source and Materials Science

The structure of an Al_3Mn amorphous alloy synthesized via magnetron sputtering was investigated using synchrotron anomalous X-ray scattering. The structural features around Mn were significantly different from those inferred by the dense random packing hard-sphere model, suggesting that the environmental structure around this metal is influenced by chemical interactions, similar to those of crystalline Al_3Mn. Our analysis also showed that the medium-range ordering structure, corresponding to a pre-peak signal, was associated with Al-Mn and Mn-Mn correlations accompanied by number density modulation and the non-Bernal-type coordination geometry [1].

A 25 μm Al_3Mn amorphous-alloy thin film was prepared on a single-crystal Si wafer via multi-target magnetron sputtering. Ordinary and anomalous X-ray scattering (AXS) measurements at the Mn K absorption edge were performed at the beamline station BL-7C, Institute of Materials Structure Science, High Energy Accelerator Research Organization, Tsukuba, Japan. An initial model of 25,000 atoms (Al: 18,750 and Mn: 6,250) with a dense random packing (DRP) structure, in a cubic hypercell with a unit size (L) of 7.546 nm, was used for the reverse Monte Carlo (RMC) simulation. Figure 1 shows the experimental and calculated (using the DRP and RMC structural models) interference functions. A pre-peak signal around Q = 16 nm^{-1}, showing the unique medium-range ordering, is well reproduced by the RMC model. This result clearly shows the advantage of AXS-RMC analysis for a detailed discussion of fine structures. The partial pair distribution functions calculated from the RMC model indicate that the pre-peak signal (approximately 0.45 nm) is associated with Mn-Mn and Mn-Al correlations.

The combination of common neighbor analysis (CNA) and Bernal polyhedral analysis (BPA) is useful for discussing atomic arrangements in the middle range ordering (MRO) region. CNA analysis clearly showed the extensive development of [333]$_{CN}$ root pairs for Mn-Mn and Al-Mn; however, a strong elemental selectivity was not identified in the common neighbors of [333]$_{CN}$, suggesting that the tetrahedral linkage structure of Mn-Al_3-Mn, a unique fragment of the Mackay-type icosahedral cluster, is not the predominant short range ordering (SRO) structure in amorphous Al_3Mn. The features of the non-Bernal polyhedra associated with the [211]$_{CN}$ of Mn-Mn and Mn-Al root pairs indicated the preference of non-Bernal polyhedra, leading to a significant fluctuation in number density. Considering that there was no significant chemical concentration among the common neighbors for [211]$_{CN}$, the number density fluctuations realized in the Al_3Mn amorphous alloys are unique geometrical short range ordering (GSROs) with no strong chemical correlations.

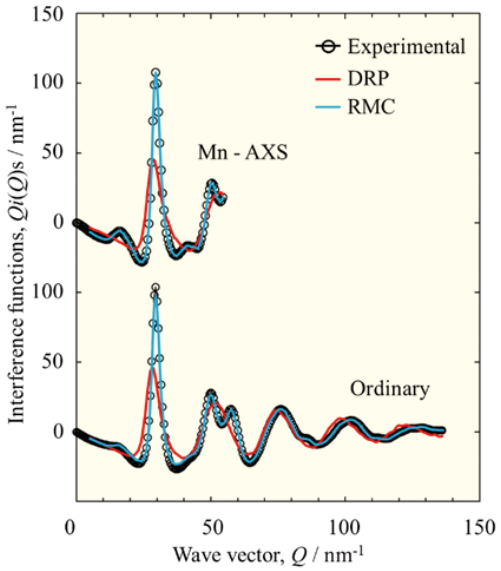

Fig. 1 Ordinary and environmental $Q(i)Q$s obtained by synchrotron AXS analysis and theoretical calculations (DRP and RMC).

These structural features can be compared to those obtained for a $Zr_{80}Pt_{20}$ amorphous alloy, where an icosahedral quasicrystal was formed by low-temperature heat treatment [2]. In this alloy, the density fluctuations were accompanied by fluctuations in elemental concentrations; that is, both the Pt-Zr_3-Pt tetrahedral linkage units, reminiscent of the Mackay cluster, and non-Bernal polyhedral regions were enriched in Pt.

References

[1] T. Kawamata and K. Sugiyama, J. Phys. Conf. Ser. **2461**, 012017 (2023).

[2] T. Kawamata, T. Muto, and K. Sugiyama, Mater. Trans. **62**, 20 (2021).

Toru Kawamata (Corresponding Author, Center for Advanced Light Source and Materials Science / Chemical Physics of Non-Crystalline Materials Research Laboratory)
E-mail: kawamata@tohoku.ac.jp
Kazumasa Sugiyama (Head of Center for Advanced Light Source and Materials Science)
URL: http://www.imr.tohoku.ac.jp/en/about/divisions-and-centers/collaboration/08.html

Uncovering Fractional Quantum Hall Effect in an InAs Two-Dimensional Electron Gas by Gate Tuning

Laboratory of Low Temperature Materials Science

InAs is a candidate material for achieving topological states with non-Abelian quasiparticles in the form of a fractional quantum Hall (FQH) insulator/superconductor hybrid. We succeeded in inducing the FQH state at filling factors of ν = 5/3, 4/3, 2/3, and 1/3 in a two-dimensional electron gas confined to an InAs/AlGaSb quantum well by tailoring the electron wave function using a dual-gate configuration.

Recently, an interface composed of a fractional quantum Hall (FQH) insulator and an *s*-wave superconductor has attracted interest as a research field for achieving the topological states of matter with non-Abelian quasiparticles. Among the various semiconductors, InAs is a promising candidate to achieve such an interface, as it is known to form a transparent contact with superconductors, such as Al. Partial observations of the FQH effect in two-dimensional electron gases have also been reported in high-quality InAs/AlGaSb quantum well (QW) structures. However, the reported FQH state was limited to the one at the Landau filling factor of ν = 4/3 ($\nu = nh/eB$, where n the electron density, h is the Planck's constant, e is the elementary charge, and B is the magnetic field). This may be caused by the asymmetric conditions of the QW, such as the difference in roughness or charged impurities at the top and low interfaces/barriers.

To investigate the correlation between the QW symmetry and the visibility of the FQH state, we prepared an InAs/AlGaSb heterostructure, as shown in Fig. 1(a), via molecular beam epitaxy, which was designed to independently control the electron density and shape of the confinement potential in the QW by using the top and back gate voltages, V_{TG} and V_{BG}, respectively. Magnetotransport (longitudinal and transverse resistance, R_{xx} and R_{xy}, respectively) measurements were performed at temperatures as low as 0.48 K and magnetic fields up to 24 T [1]. As shown in Fig. 1(b), the signatures of FQH (deep minima in R_{xx} and plateau in R_{xy} as a function of the electron density) were observed at ν = 1/3 and 2/3 when V_{TG} was swept while maintaining V_{BG} = 0 V. Moreover, as shown in Fig. 1(c), we succeeded in inducing additional FQH states at ν = 4/3 and 5/3 by applying V_{BG} to alter the distribution of the electron wave function within the QW in combination with V_{FG}. Our results indicate a significant impact of the shape of the QW confinement potential on the visibility of the FQH states and existence of asymmetric disorder, in addition to interface roughness and background impurities, which affect the FQH effect.

References

[1] S. Komatsu, H. Irie, T. Akiho, T. Nojima, T. Akazaki, and K. Muraki, Phys. Rev. B **105**, 075305 (2022).

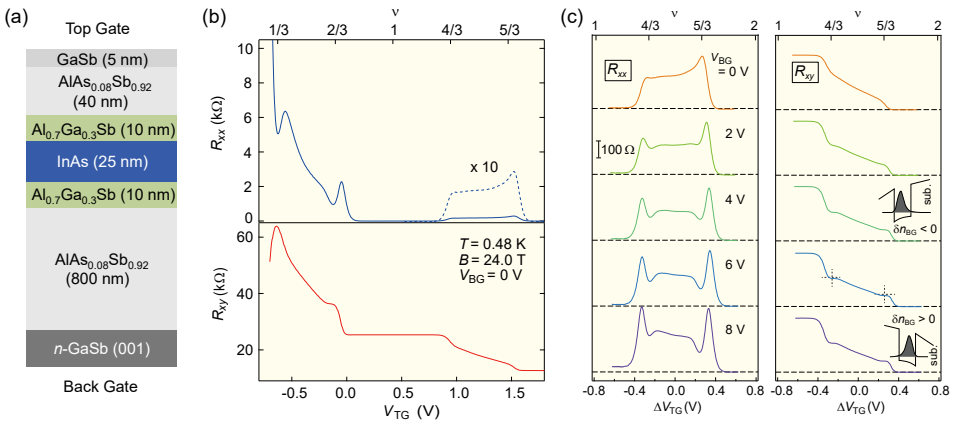

Fig. 1 (a) InAs/AlGaSb heterostructure prepared in this work, where the two-dimensional electron gas located in a 25 nm wide InAs quantum well can be controlled by both top and back gates. (b) V_{TG}-dependence of R_{xx} (upper) and R_{xy} (lower) as measured at 0.48 K and 24 T with V_{BG} = 0 V. (c) R_{xx} and R_{xy} traces for different V_{BG} values at 0.48 K and 24 T. ΔV_{TG} represents the change in V_{TG} measured from ν = 3/2 at each V_{BG} [1].

Tsutomu Nojima (Corresponding Author, Laboratory of Low Temperature Materials Science)
E-mail: t.nojima@tohoku.ac.jp
Takahiko Sasaki (Head of Laboratory of Low Temperature Materials Science)
E-mail: takahiko.sasaki.d3@tohoku.ac.jp
URL: http://ltsd.imr.tohoku.ac.jp/index-e.html

Research Facility for Analyzing the Physical and Chemical Properties of Radioactive and Nuclear Materials

Laboratory of Alpha-Ray Emitters

More than 170 species of radioisotopes and nuclear materials are available for study at the Laboratory of Alpha-Ray Emitters. This laboratory is one of the most important centers worldwide for studying the physical and chemical properties of radioactive materials such as actinide compounds. Researchers from several leading universities and institutes all over Japan visit this facility every year to prepare a variety of materials and conduct chemical and physical experiments.

The Laboratory of Alpha-Ray Emitters provides a research environment for the study of 170 radionuclides and elements, especially alpha-ray emitters such as actinides. This laboratory functions as a source for the preparation of pure crystals of actinide compounds, providing them to other universities and synchrotron particle accelerators. In the past decade, actinium-225 (Ac-225), an actinide, has been provided to other universities and research centers for research to foster inter-university collaboration. The radiation-controlled area of this laboratory includes three chemical rooms, three physical rooms, and other facilities, which are equipped with local exhaust ventilation systems, ensuring safety while handling various types of radioactive materials. Several spectrometers, including those for gamma and alpha rays, are also available.

Radioisotope ^{90}Sr ($t_{1/2}$ = 28.9 y) is a major heat-generating nuclide, similar to ^{137}Cs, which is contained in the high-level waste (HLW) produced from nuclear reactors. The removal of ^{90}Sr and ^{137}Cs from the HLW has been studied to better manage the risks of medium-term hazards. Dicyclohexano-18-crown-6 (DCH18C6) and its derivatives are suitable for Sr (II) extraction. Thus, extensive extractions using crown ethers have been developed for the treatment and disposal of HLW. Although a system containing crown ethers shows good Sr (II) extraction ability, the diluent toxicity, low flash point, and high boiling point leave room for development. Further development of Sr(II) extraction relies on the availability of risk-free and easily regenerated diluents, and the establishment of an extraction system has drawn a significant amount of attention. Fluorinated solvents have also attracted continuous interest in the separation and purification technology because of their unique properties, such as good extractability, significantly low solubility in water (generally lower than conventional organic solvents), and chemical and radioactive stability. The combination of a fluorinated solvent (hydrofluorocarbon HFC-43-based solvent) and DCH18C6 for Sr(II) solvent extraction was studied using two characteristic

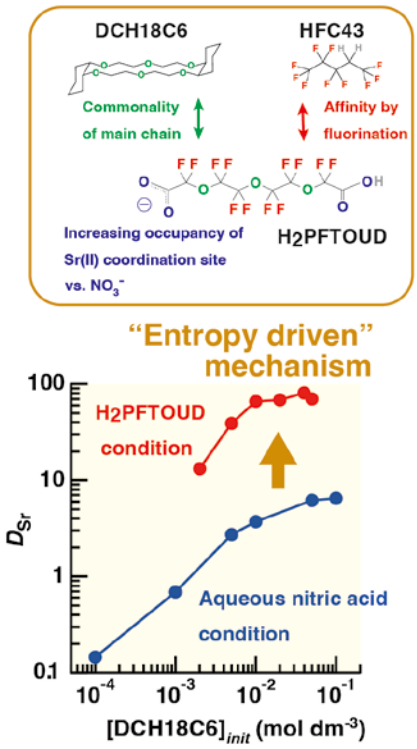

Fig. 1 Sr(II) solvent extraction system composed of dicyclohexano-18-crown-6 and hydrofluorocarbon HFC-43-based solvents and its Sr(II) extractability under different acid conditions.

acids, i.e., nitric acid, which is typically present in HLW, and perfuruoro-3-6-9-trioxaundecane-1,11-dioic acid with both hydrophilicity and affinity to fluorinated solvents [1]. The maximum distribution ratio of Sr(II) (D_{Sr}) observed for the latter acid was ~180, which was more than10 times larger than that of the former acid (Fig. 1). The combination of HFC-43-based solvents and DCH18C6 exhibits significant potential for use in extraction systems.

References

[1] K. Shirasaki, M. Nagai, M. Nakase, C. Tabata, A. Sunaga, T. Yaita, and T. Yamamura, RSC Advances **12**, 26922 (2022).

Kenji Shirasaki (Head of Laboratory of Alpha-Ray Emitters)
E-mail: kenji.shirasaki.e4@tohoku.ac.jp
URL: http://alpha.imr.tohoku.ac.jp/en.html

Multiscale Characterization of Advanced Materials Using Aberration-Corrected Analytical Transmission Electron Microscopy

Analytical Research Core for Advanced Materials

The Analytical Research Core for Advanced Materials serves as an infrastructure for researchers in IMR and outside the university, offering various elemental analytical methods and up-to-date structural characterization techniques. These include aberration-corrected microscopy, which allows three-dimensional and atomic resolution observations of a wide range of materials.

The Analytical Research Core for Advanced Materials (ARCAM) provides elemental composition data and supports Transmission Electron Microscopy (TEM) analysis of metals and inorganic materials. We also develop analytical procedures to obtain reliable analytical data. The ARCAM assays major and trace elements in consigned samples using the following methods: ICP-AES, ICP-MS, flame and graphite furnace AAS, microwave induced plasma AES, CS/ON/H analysis, XRF, ion chromatography, and conventional chemical analyses (e.g., gravimetry, titrimetry, and spectrophotometry). Additionally, we provide TEM analysis services on structural and functional materials and microdevices, enabling the evaluation of microstructures, crystal structures, and chemical compositions at the nano-/meso-scale.

ARCAM is heavily involved in the user-facility network with government support. This includes a nanotechnology platform (up to 2021fy) and an advanced research infrastructure for materials and nanotechnology in Japan (ARIM, 2021fy onward), both of which are supported by the Ministry of Education, Culture, Sports, Science and Technology of Japan. These programs provide access to our facilities for researchers in academia and industry. They can also request technical and scientific support for the Center for Integrated Nanotechnology Support (CINTS) at Tohoku University. ARCAM provides several facilities via ARIM, including a focused-ion beam apparatus and an aberration-corrected microscope that are extensively used by researchers worldwide.

Multiscale characterization is fundamental to understanding the electric properties of iron-based superconductors because superconducting behavior depends on both the crystal structure and microstructure. Here, various defects and grain boundaries play an essential role in achieving a sufficient critical current density. Dr. Shimada and his group employed these apparatuses to examine the real-space dispersion of relevant phases and grain boundary structures three-dimensionally, aiming to elucidate the origin of sensitive dependence on the structure [1].

Fig.1 TEM equipped with aberration correctors both in illumination and objective lens systems. This microscope is open to users outside the campus.

Another example employs aberration-corrected microscopy to elucidate the crystallization behavior and domain structure of recently developed fluorite-structured oxides, as exemplified by Dr. Shiraishi's group [2]. The authors demonstrated that atomically resolved images of CeO_2-HfO_2 thin films are equivalent to the direct determination of their domain structure.

The use of ARCAM and ARIM facilities is not limited to functional materials and is used to study structural alloys [3] and soft matter, such as biomaterials and organic conducting substances.

References

[1] Y. Shimada, S. Tokuta, A. Yamanaka, A. Yamamoto, and T.J. Konno, J. Alloys. Compd. **923**, 166358 (2022).

[2] T. Shiraishi, S. Choi, T. Kiguchi, and T.J. Konno, Acta Mater. **235**, 118091 (2022).

[3] Y. Shimada, Y. Ikeda, K. Yoshida, M. Sato, J. Chen, Y. Du, K. Inoue, R. Maaß, Y. Nagai, and T.J. Konno, J. Appl. Phys. **131**, 164902 (2022).

Toyohiko J. Konno (Corresponding Author, ARIM Project Unit, Analytical Research Core for Advanced Materials)
E-mail: tjkonno@tohoku.ac.jp
Eiji Akiyama (Head of Analytical Research Core for Advanced Materials)
E-mail: eiji.akiyama.d1@tohoku.ac.jp
URL: http://bunseki-core.imr.tohoku.ac.jp/top_eca_eng.html
http://www.imr.tohoku.ac.jp/en/about/divisions-and-centers/service-divisions/03.html

International Collaborative Research

IMR KINKEN Research Highlights 2023

Investigation of Charge Density Waves of $YBa_2Cu_3O_{6.67}$ in Strong Pulsed Magnetic Fields

We investigated charge density waves using pulsed magnetic fields to understand the normal states in high-T_c superconductors. Recent progress in pulsed high-magnetic-field diffraction has also been reported. The relationship between the broken symmetry states found in optical pumping and the three-dimensional charge density wave states reveals a new aspect of the normal state under very high magnetic fields.

Understanding high-*Tc* cuprates has been one of the most important topics in strongly correlated electron systems for several decades. The appearance of charge density waves (CDWs) has recently attracted considerable attention. This is a significant challenge because of the difficulty in conducting X-ray diffraction in very high magnetic fields and the small intensity of the superlattice peaks caused by the CDW.

Our strategy is to combine X-rays with significantly high instantaneous intensity and pulsed magnetic fields with ultra high peak intensity. For this purpose, we used X-ray free-electron lasers (XFELs), such as the Linac Coherent Light Source (LCLS) and Spring-8 Angstrom Compact Free-Electron Laser (SACLA), as light sources. Conversely, for the pulsed magnetic field, we developed a compact pulsed magnetic field system that is optimal for this experiment.

Figure 1 shows an image of the backscattering X-ray diffractometer installed at the SACLA XFEL. A magnetic field of up to 50 T was generated using a compact conical horizontal coil. The lowest sample temperature of 2.5 K was achieved by combining a ^{4}He reservoir tank and 4 K Gifford–McMahon cryocooler. It operates with a single short mode. During the initial cooling, approximately 20 L He gas is condensed in to the tank and then it is depressurized using a vacuum pump thorough a thin gas line. When the incoming heat is well balanced with the cooling power, the lowest temperature is maintained for more than 24 h. The combination of 50 T and 2.5 K for X-ray diffraction is unique and is only possible with our system. Moreover, pulsed high-field systems have been installed in other XFEL facilities such as LCLS and Swiss X-ray free-electron laser.

We conducted CDWs of $YBa_2Cu_3O_{6.67}$ and identified two types of CDWs [1]. More recently, we investigated the photo-pumping-induced normal state [2]. By combing these experiments, we obtained a comprehensive picture for the phase diagram of $YBa_2Cu_3O_{6.67}$

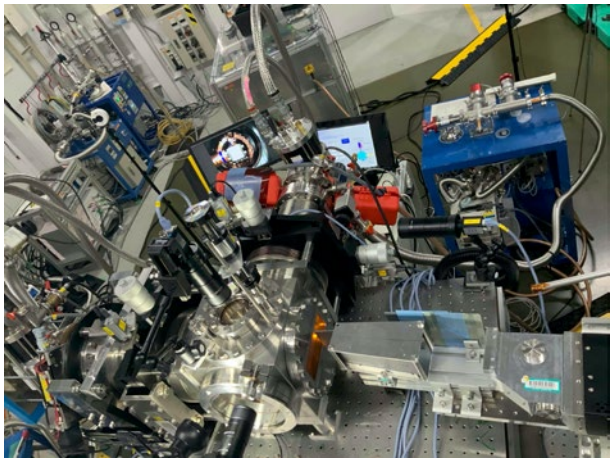

Fig. 1 Experimental setup developed by the Institute for Materials Research for high-magnetic-field X-ray diffraction using Spring-8 Angstrom Compact Free-Electron Laser.

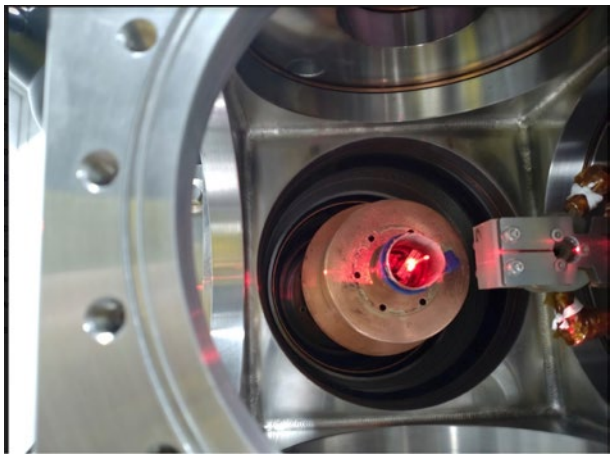

Fig. 2 Sample cryostat (center) and horizontal conical coil (right).

References

[1] S. Gerber *et al.*, Science **350**, 949 (2015).
[2] H. Jang *et al.*, Sci. Adv. **8**, eabk0832 (2022).

Hiroyuki Nojiri (Magnetism Research Laboratory)
E-mail: hiroyuki.nojiri.e8@imr.tohoku.ac.jp
URL: http://www.hfpm.imr.tohoku.ac.jp

Three-Dimensional Interconnected Nanoporous FeCo Soft Magnetic Materials Synthesized Using Liquid Metal Dealloying

Three-dimensional interconnected nanoporous (3DNP) FeCo soft magnetic materials were produced via liquid metal dealloying (LMD). The processing temperature affected the morphology and grain boundary characteristics of 3DNP FeCo materials. The LMD process shows its advantages for synthesizing nanostructured FeCo with high magnetization and low coercivity.

FeCo alloys are important soft magnetic materials because of their highest saturation of magnetization, high Curie temperature, and low losses [1]. Recently, nanostructured soft magnetic materials have been investigated in a variety of potential applications such as magnetic shielding, targeted drug delivery, and magnetic resonance imaging. Consequently, nanostructured FeCo alloys are attracting increasing attention, and several chemical synthesis techniques have been suggested, such as sol-gel method, hydrogen reduction, thermal decomposition, reductive decomposition, polyol synthesis, and liquid-phase reduction. Properties of nanostructured FeCo materials are highly dependent on the synthesis methodology. Moreover, typical synthesis methods exhibit limitations such as a long processing time, use of environmentally hazardous chemicals, and especially, the formation of undesirable impurities (e.g., oxide formation).

In this study, three-dimensional interconnected nanoporous (3DNP) FeCo materials were newly synthesized via liquid metal dealloying (LMD) [2]. Three different precursor alloys: $(FeCo)_{70}Ni_{30}$, $(FeCo)_{50}Ni_{50}$, and $(FeCo)_{30}Ni_{70}$ (in at%) were prepared from high-purity raw materials (over 99.9 at%) under a purified Ar atmosphere. The LMD process was conducted for 36 min at constant temperatures of 600, 700, and 800 °C in an Mg-10 at% Ca metallic melt. During the LMD process, nanostructured FeCo alloys were produced by the selective dissolution of solely miscible Ni atoms and self-organization of Fe and Co atoms [3, 4].

The average porosity of the 3DNP FeCo was 32.3, 48.8, or 71.7%, depending on the concentration of Ni in the precursor alloys. Moreover, the size of FeCo ligament varied from 0.75 to 3.05 μm depending on the temperature and precursor composition. Fe and Co were near equiatomic at low temperatures; however, Co atoms became more soluble in the melt at a high temperature of 800 °C. More importantly, the grain boundary area was significantly reduced when the processing temperature increased, and the fractions of high-angle grain and coincidence lattice site boundaries decreased from 73.6 to 16.3% corresponding to a decrease in temperature from 600 to 800 ℃.

Temperature and precursor composition significantly influence the final microstructure of the 3DNP FeCo materials, and magnetic properties are dependent on the microstructure. The LMD process can prevent contamination and oxidation in the Mg melt. Consequently, all samples revealed high-saturation magnetizations of approximately 220 emu/g, which is close to that of bulk FeCo (245 emu/g). The increase in the LMD temperature decreased the coercivity, which is related to the reduced grain boundary area. The LMD process exhibits advantages over other synthesis methods in terms of high-saturation magnetization and low coercivity (Fig. 1).

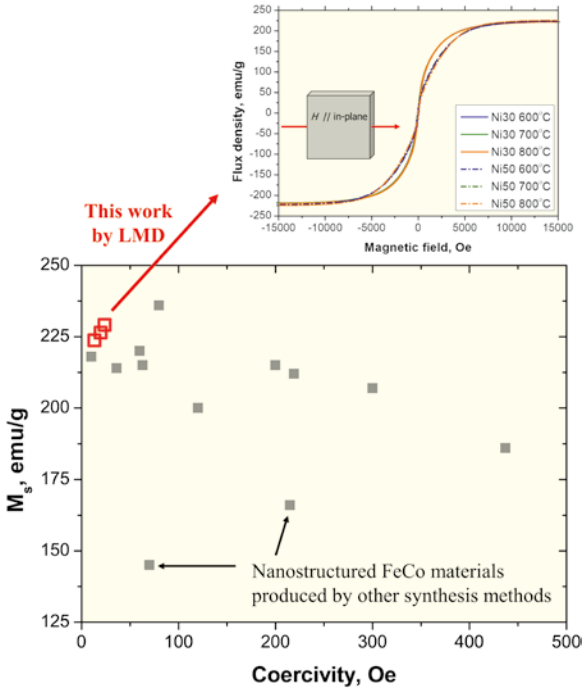

Fig. 1 Saturation magnetization and coercivity of nanostructured FeCo materials.

References

[1] R. S. Sundar and S. C. Deevi, Int. Mater. Rev. **50(3)**, 157 (2005).
[2] S.-H. Joo and H. Kato, J. Alloys Compd. **908**, 164688 (2022).
[3] T. Wada, K. Yubuta, A. Inoue, and H. Kato, Mater. Lett. **65(7)**, 1076 (2011).
[4] S.-H. Joo, T. Wada, and H. Kato, Mater. Des. **180(15)**, 107908 (2019).

Soo-Hyun Joo (Corresponding Author, Dankook University)
E-mail: jjsh83@dankook.ac.kr
Hidemi Kato (Non-Equilibrium Materials Research Laboratory)
E-mail: hidemi.kato.b7@tohoku.ac.jp
URL: http://www.nem2.imr.tohoku.ac.jp/index-e.html

Alloy Design Approach for Mitigating Gas Pores in Additive Manufacturing

Porosity in additively manufactured Co–Cr–Mo alloys with varying carbon contents were characterized by quantitative X-ray computed tomography based on the collaborative work of researchers at the National Institute of Applied Sciences of Lyon (INSA Lyon), France. Gas pores that had been entrapped in the raw powders were eliminated during the subsequent electron beam powder bed fusion process depending on the solidification behavior that varied with the carbon content. A novel alloy design approach for the reduction in gas pores, which can critically influence the performance of the alloy, in the as-built materials was proposed.

Additive manufacturing (AM) is promising not only for producing complex geometries but also improving material properties with tailored microstructures. Particularly, powder bed fusion (PBF) processes create bulk non-equilibrium microstructures by repeating rapid cooling in a confined melt volume. However, the mitigation of porosity/defects is essential in metal AM for achieving the desired properties. Generally, process-induced defects, such as lack-of-fusion, keyhole pores, and cracking, can be reduced by optimizing the process parameters. In contrast, gas pores in the raw powders often remain in the as-built materials, acting as crack nucleation sites during subsequent mechanical loading [1]. Thus, efforts have been devoted to developing high-quality powders with negligible gas pores [2]. However, eliminating powder-originated gas pores is still challenging.

In this study [3], we demonstrated that the amount of gas pores in electron beam PBF (EB-PBF) materials alters depending on the solidification behavior. A model alloy system, Co–27Cr–6Mo–(0.04–2.5)C (wt.%), which was developed for industrial applications, e.g., cutting tools for corrosive environments, was employed. Using X-ray computed tomography, we successfully captured the spherical gas pores and quantified the porosity in the raw powders and as-built materials (Fig. 1). The results clarified that the continuous addition of carbon increased the porosity of the powder, suggesting a potential effect through a significant reduction in the liquidus temperature. In contrast, the as-built alloy specimens fabricated under an identical EB-PBF condition showed a non-monotonous carbon concentration dependence on porosity. When using 0.04 and 0.22 wt.% carbon, negligible pores were captured after the EB-PBF process. The maximum porosity in the as-built state was detected at 2.0 wt.%. Further carbon addition up to 2.5 wt.% significantly decreased the porosity. The microstructural characterization indicated a transition

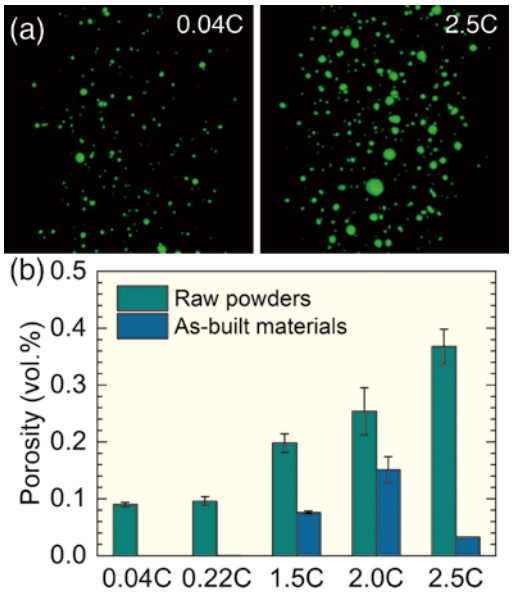

Fig. 1 (a) Three-dimensional reconstruction images of gas pores in the raw powders and (b) carbon concentration dependence of porosity.

from cellular (0.04 and 0.22 wt.% carbon) to dendritic solidification (1.5 and 2.0 wt.% carbon). A eutectic microstructure was observed at 2.5 wt.% of carbon. Therefore, we concluded that ensuring a smooth solidification front during the cellular/eutectic solidification effectively eliminates gas pores from the solidified portion, while the complicated solid–liquid interfaces entrap gas bubbles in the melt pool during dendritic solidification. The obtained findings will aid the establishment of a novel alloy design toward the mitigation of gas pores.

References

[1] X. Shui, K. Yamanaka, M. Mori, Y. Nagata, K. Kurita, and A. Chiba, Mater. Sci. Eng. A **680**, 239 (2017).

[2] Y. Cui, Y. Zhao, H. Numata, K. Yamanaka, H. Bian, K. Aoyagi, and A. Chiba, Powder Technol. **393**, 301 (2021).

[3] S. Aota, K. Yamanaka, M. Mori, N. Sasaki, J. Adrien, E. Maire, D. Fabrègue, and A. Chiba, Addit. Manuf. **59**, 103134 (2022).

Kenta Yamanaka (Deformation Processing Research Laboratory)
E-mail: kenta.yamanaka.c5@tohoku.ac.jp
URL: http://www.chibalab.imr.tohoku.ac.jp/english/index.html

Anisotropic Electronic Correlations Detected via Resistivity Measurements in the Heavy-Fermion Paramagnet UTe_2

We thoroughly investigated the anisotropy of the electrical resistivity of the heavy-fermion superconductor UTe_2 under an intense magnetic field of up to 70 T for different electrical currents and magnetic field directions, and two characteristic temperatures and anisotropic resistivity coefficients were extracted. Their characteristic behavior near the metamagnetic transition at H_m ~35 T was characterized. Anisotropic scattering processes due to magnetic fluctuations were evidenced.

The recent discovery of unconventional superconductivity in the heavy-fermion paramagnet UTe_2 opened a new route for investigating the interplay between magnetism and superconductivity. Spin-triplet superconductivity was initially proposed for this compound as a nearly ferromagnetic system. The spin-triplet superconductivity in UTe_2 is supported by the observation of a large upper critical field H_{c2} exceeding the Pauli limit and via nuclear magnetic resonance Knight shift experiments. Contrary to early expectations, ferromagnetic fluctuations have never been detected experimentally; instead, low-dimensional antiferromagnetic fluctuations with an incommensurate wave vector are detected by inelastic neutron scattering experiments. The anisotropy of magnetic fluctuations must be investigated up to high magnetic fields close to the metamagnetic transition field, H_m ~35 T.

In this work, we performed systematic resistivity measurements under a high magnetic field of up to 70 T applied along the three crystallographic directions: *a*, *b*, *c*-axes in the orthorhombic structure [1]. Figure 1(a) shows the temperature-field phase diagram determined using resistivity measurements for H || *b*-axis, corresponding to a hard magnetization axis. Field-reentrant superconductivity up to H_m ~35 T, as well as two characteristic temperatures of approximately 15 and 35 K, were detected. The electrical resistivity measurements were performed using a pulse-field magnet at different temperatures. Figure 1(b) shows the field dependence of the resistivity coefficient A, assuming Fermi liquid behavior at low temperatures. A remarkably sharp increase in the A coefficients up to H_m and an abrupt drop above H_m are clearly observed, indicating the development of magnetic fluctuations. These results are consistent with the magnetovolume effect on the first-order metamagnetic transition [2] and field-dependent Sommerfeld coefficients [3].

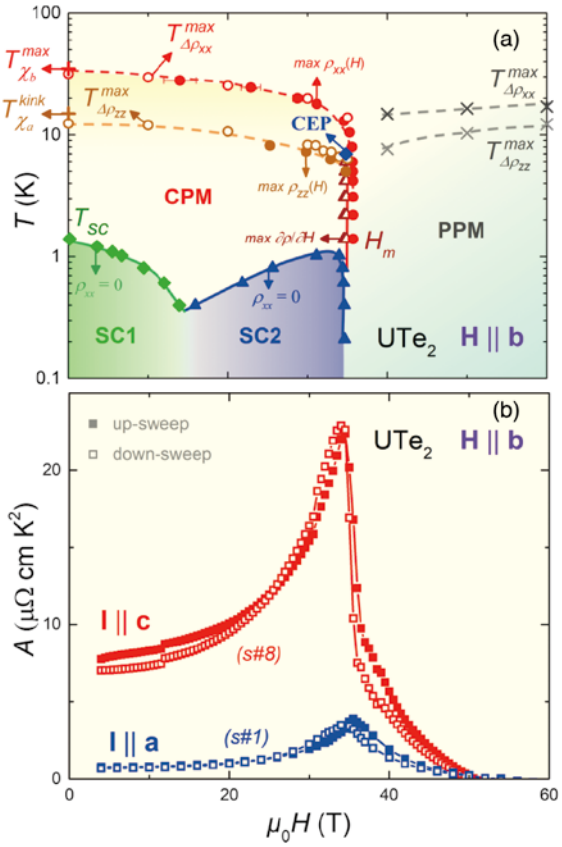

Fig.1 (a)Temperature-field phase diagram for H || *b*-axis in UTe_2. (b) Field dependence of the resistivity A coefficient.

References

[1] T. Thebault, M. Valiska, G. Lapertot, A. Pourret, D. Aoki, G. Knebel, D. Braithwaite, and W. Knafo, Phys. Rev. B **106**, 144406 (2022).

[2] A. Miyake, M. Gen, A. Ikeda, K. Miyake, Y. Shimizu, Y. J. Sato, D. Li, A. Nakamura, Y. Homma, F. Honda, J. Flouquet, M. Tokunaga, and D. Aoki, J. Phys. Soc. Jpn. **91**, 063703 (2022).

[3] A. Miyake, Y. Shimizu, Y. J. Sato, D. Li, A. Nakamura, Y. Homma, F. Honda, J. Flouquet, M. Tokunaga, and D. Aoki, J. Phys. Soc. Jpn. **90**, 103702 (2021).

Dai Aoki (Actinide Materials Science Research Laboratory)
E-mail: dai.aoki.c2@tohoku.ac.jp
URL: http://www.imr.tohoku.ac.jp/en/about/divisions-and-centers/research-division/25.html

Electronic States of Non-Centrosymmetric Chiral Crystal PtAl

International Research Center for Nuclear Materials Science

Symmetry-protected nontrivial states in topological compounds have attracted considerable attention. In this study, we investigated the electronic states of the chiral quantum material PtAl by considering the de Haas–van Alphen effect. The smallest Fermi pocket, α, possesses a nontrivial Berry phase in which a Weyl nodal fermion is formed at the Γ point.

The interplay between crystalline symmetries and band topology can lead to various exotic states in materials, which have been intensively investigated over the years. The chirality, degeneracy, and dimensionality of the crossing points distinguish the numerous topological states in materials. Nonsymmorphic symmetries can impose band crossings at high-symmetry points in the Brillouin zone and produce higher-fold fermions. Specifically, cubic systems of the space group $P2_13$ (No.198), such as Rh(Si,Ge) and (Pd,Pt)Ga, exhibit nonsymmorphic symmetry-protected multifold fermions at high-symmetry points with unconventional low-energy excitations called the spin 3/2 Rarita–Schwinger fermion.

In this study, we investigated the topological quantum properties of single crystals of the chiral material PtAl via magnetotransport measurements and the de Haas–van Alphen (dHvA) oscillations [1]. High-quality single crystals were grown using the Czochralski method in a tetra-arc furnace. The dHvA experiments were performed using the field-modulation technique at high fields of up to 12 T and temperatures as low as 1 K. Figure 1(a) shows the crystal structure of PtAl with the space group $P2_13$, which is classified as a nonsymmorphic chiral structure. Figure 1(b) shows the angular dependence of the experimental and theoretical dHvA frequencies. Three types of Fermi surface sheets were detected: α, γ, and δ. These sheets can split into two owing to band splitting in the non-centrosymmetric crystal structure. The calculated Fermi surfaces are illustrated in Fig.1(c), where the Fermi surfaces α and α' located at the Γ point occupy significantly small volumes in the Brillouin zone. The estimated spin-split energy is 567 K, which is reasonably high, suggesting the strong spin-orbit strength of PtAl. From the analysis of the Landau fan diagram, the α and α' bands were observed to possess nontrivial and trivial Berry phases of 1.16π and 011π, respectively.

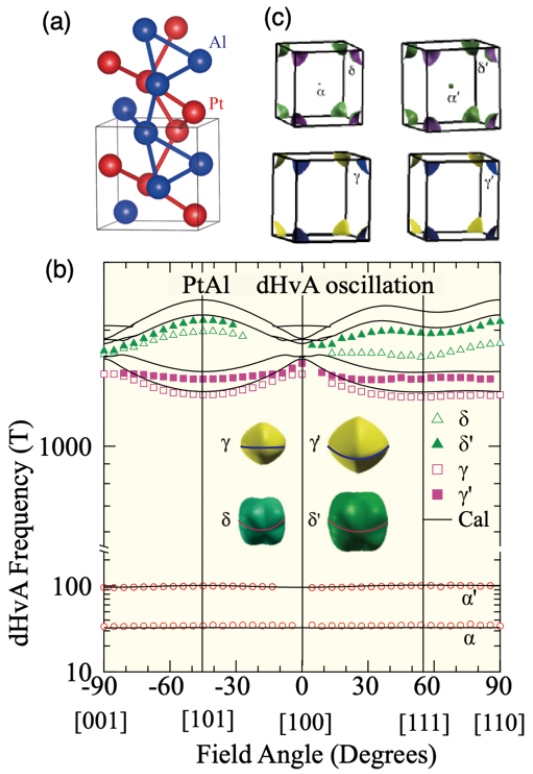

Fig. 1(a) Chiral crystal structure of PtAl with the space group $P2_13$. (b) Angular dependence of the de Haas–van Alphen frequencies of PtAl. The solid lines show the results of band calculations. (c) Calculated Fermi surfaces of PtAl.

References

[1] V. Saini, S. Sasmal, R. Kulkarni, B. Singh, A. Thamizhavel, A. Nakamura, and D. Aoki, Phys. Rev. B **106**, 125126 (2022).

Arumugam Thamizhavel (Corresponding Author, Tata Institute of Fundamental Research)
E-mail: thamizh@tifr.res.in
Yasuyoshi Nagai (Head of International Research Center for Nuclear Materials Science)
E-mail: yasuyoshi.nagai.e2@tohoku.ac.jp
URL: http://www.imr-oarai.jp/en/

Microstructure and Strength of Low-Stacking-Fault-Enegy Cu–In Alloy Wires

Cooperative Research and Development Center for Advanced Materials

Conductive spring wires for application in electrical components require high strength, high electrical conductivity, and convenient manufacturability. We observed that Cu–In solid solution alloy wires exhibited a superior combination of strength and conductivity, which was primarily achieved by grain refinement due to their low stacking fault energy and high twinnability.

Innovations in electronic devices have revealed a need for enhancing the strength and electrical conductivity of Cu-based alloy wires and sheets. Especially, the production of solid-solution-strengthened Cu alloys with an advantageous combination of strength and conductivity that is comparable to those of age-hardenable alloys for use in electrical applications is of significant importance, because the manufacturing process for the former alloys is far simpler than that for the later ones. Cu–In solid solution alloys are suitable candidates for such wire materials [1]. Herein, we systematically investigate the microstructure and properties of Cu–In alloy wires fabricated via severe drawing. Then, based on the results obtained, we discuss the strengthening mechanism of the Cu–In alloy wires.

Figure 1 shows the inverse pole figure and grain boundary distribution maps obtained via electron backscatter diffraction analysis of the Cu–1.0, 4.0, and 5.0 at.% In alloy rods with a diameter of 3.0 mm before drawing and those obtained after drawing of the wires to equivalent strains ε of 0.81 (2.0 mm) and 4.61 (0.3 mm). All the Cu–In alloys show typical equiaxial Cu solid solution grains with an average size of approximately 10 μm. During the initial stage of drawing to ε = 0.81, deformation twin boundaries were formed, which increased with increasing In content (red lines in Fig. 1(b)). This indicates that the In solute efficiently reduced the stacking fault energy of the Cu matrix. The deformation twins promote grain refinement during subsequent drawing. The Cu–5.0 at.% In alloy wire that was severely drawn to ε = 4.61 possessed ultrafine grains of approximately 100 nm in size, which was significantly smaller than those in the other alloys (Fig. 1(c)). Consequently, the Cu–5.0 at.% In alloy wire drawn to ε = 4.61 exhibited superior yield and tensile strengths of 1280 and 1340 MPa, respectively, with a conductivity of 24% of the International Annealed Copper Standard. The performance of the solution-strengthened Cu–5.0 at.% In alloy wires that was severely drawn was comparable to that of commercial age-hardenable Cu–Ti and Cu–Be alloy wires. The combination of strength and electrical conductivity of the Cu–In alloy wires will be optimized in future studies by optimizing both the alloy compositions and the deformation mechanism.

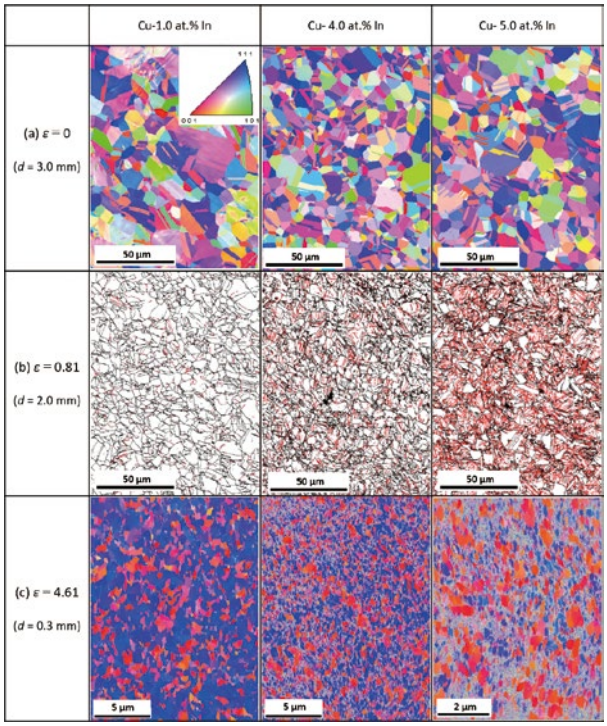

Fig. 1 Inverse pole figure and grain boundary (GB) maps obtained via electron backscatter diffraction of the cross-section of the Cu–1.0, 4.0, and 5.0 at.% In alloy rods (a) before drawing, and after wire drawing to (b) 2.0 mm (ε = 0.81), and (c) 0.3 mm (ε = 4.61). In the GB map of (b), high-angle GBs with a misorientation angle in excess of 15° are depicted using solid-back lines, while twin boundaries corresponding to an angle of 55-62.8° are indicated by red lines.

References

[1] Y. Abe, S. Semboshi, N. Masahashi, E-A. Choi, and S.Z. Han, Metall. Mater. Trans. A, **54**, 928 (2023).

Satoshi Semboshi (Corresponding Author, Cooperative Research and Development Center for Advanced Materials)
E-mail: satoshi.semboshi.c8@tohoku.ac.jp
Naoya Masahashi (Head of Cooperative Research and Development Center for Advanced Materials)
E-mail: naoya.masahashi.e6@tohoku.ac.jp
URL: http://www.crdam.imr.tohoku.ac.jp/en/index-en.html

Improved Critical Current Density Performance in High Temperature Superconducting Tapes using a Thermodynamic Approach

High Field Laboratory for Superconducting Materials

The critical current density (J_c ~ 130 MA/cm^2) and flux pinning force density (F_p ~ 3.17 TN/m^2) for nanocomposite rare-earth metal $Ba_2Cu_3O_y$ films on metallic substrates (CCs) were successfully determined at 4.2 K using both the thermodynamic route and size, incorporating large densities of incoherent nanoparticles. The J_c and F_p values obtained in our CC for the over-doped $REBa_2Cu_3O_y$ are the highest ever reported for superconductors.

The improvement of critical current density (J_c) in practical high-temperature superconductors (HTSs) such as $REBa_2Cu_3O_y$ (REBCO, where RE are rare-earth metals and Y) coated conductors (CCs) has recently gained increased attention. The nanoparticle-related flux-pinning landscape improves J_c. The higher hole-carrier density in REBCO also improves J_c because it increases the thermodynamic departing critical current, (J_d). However, it is difficult to optimize the carrier density in nanoparticle-introduced REBCO films because of the local strain induced at the interface between the nanoparticles and REBCO matrix. In this study, we optimized carrier doping in nanoparticle-introduced REBCO films by introducing incoherent $BaHfO_3$ nanoparticles in REBCO films.

Figure 1 shows the critical current density in the self-field (J_c^{sf}) and depairing current density (J_d) of several HTSs at 4.2 K. We can achieve 0.3 · J_d in $(Y_{0.77}Gd_{0.23})Ba_2Cu_3O_y$ ((Y,Gd)123) by controlling the carrier density; its variation leads to an intrinsic improvement in J_c via J_d, resulting in extremely high J_c values of 130 MA/cm^2. These values are consistent with a J_d enhancement by a factor of two for incoherent nanoparticle-doped (Y,Gd)123 coated-conductor (CC) films, indicating that this new material design can achieve high critical current densities in a wide array of superconductors. By combining the high vortex-pinning force with this thermodynamic and pinning optimization route, (Y,Gd)123 CCs reached ~3.17 TN/m^3 at 4.2 K and 18 T (Hllc) (Fig. 2), which are the highest values ever reported for superconductors.

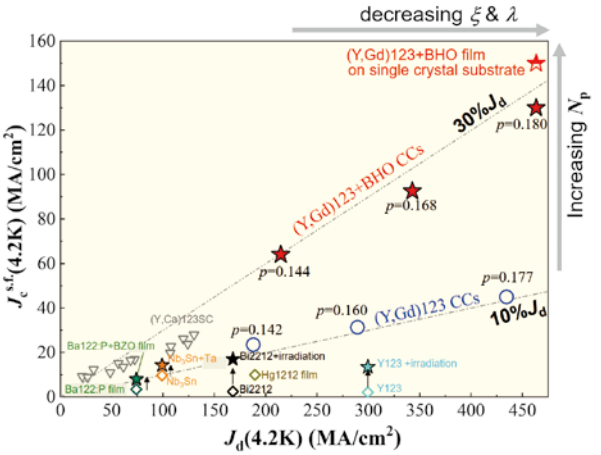

Fig. 1 Critical current density in self-field (J_c^{sf}) and depairing current density (J_d) for several HTSs at 4.2 K [1].

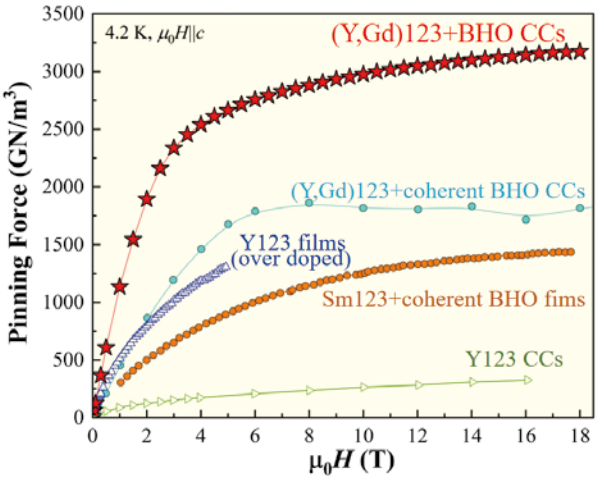

Fig. 2 Flux pinning force density F_p at 4.2 K for several HTS films for B//c [1].

References

[1] M. Miura, G. Tsuchiya, T. Harada, K. Sakuma, H. Kurokawa, N.Sekiya, Y. Kato, R. Yoshida, T. Kato, K. Nakaoka, T. Izumi, F. Nabeshima, A. Maeda, T. Okada, S. Awaji, L. Civale, and B. Maiorov, NPG Asia Materials **14**, 85 (2022).

Masashi Miura (Corresponding Author, Graduate School of Science and Technology, Seikei University)
E-mail: masashi-m@st.seikei.ac.jp
Satoshi Awaji (Head of High Field Laboratory for Superconducting Materials)
E-mail: satoshi.awaji.e8@tohoku.ac.jp
URL: http://www.hflsm.imr.tohoku.ac.jp/cgi-bin/index-e.cgi

Electronic Structures of $CH_3NH_3PbI_3/Li^+@C_{60}$ and Haeckelite Compounds

Center for Computational Materials Science

Two international collaborations using first-principles calculations were performed independently on the MASAMUNE-IMR supercomputer, which was developed by the Institute for Materials Research (IMR). One was an investigation on the effect of $Li^+@C_{60}$ on methyl-ammonium lead iodide perovskite solar cells, and the other was an investigation on the family of group III–V haeckelite compounds.

Methyl-ammonium (MA) lead iodide perovskite solar cells have attracted attention owing to their high energy conversion efficiency. However, these cells exhibit a problem of low air stability. To examine the role of using $Li^+@C_{60}$ in a dopant material in the p-type donor layer, $Li^+@C_{60}$-adsorbed tetragonal $MAPbI_3$ (001) surfaces with MAI terminations were studied using first-principles calculations [1]. The $Li^+@C_{60}$ was adsorbed above the C position with almost 100% ionization. In the $MAPbI_3/Li^+@C_{60}$ system, the highest occupied molecular orbital (HOMO) and HOMO-1 were spread out in $MAPbI_3$, while the lowest unoccupied molecular orbital (LUMO), LUMO+1, and LUMO+2 were localized in $Li^+@C_{60}$, with an energy gap of 0.6 eV. In the neutral $MAPbI_3/Li@C_{60}$ system, the singly occupied molecular orbital (SOMO) and LUMO were both localized in $Li@C_{60}$ and their energy gap of 0.125 eV was significantly small. The SOMO behaves as a hole when it loses an electron to form $Li^+@C_{60}$. The three almost degenerate LUMO levels behave as good hole conductors. Thus, we concluded that the use of $Li^+@C_{60}$ molecules instead of bare Li ions as dopant materials in $MAPbI_3$ solar cells can prevent degradation.

Eighteen III–V haeckelite compounds XY (X = B, Al, Ga, In, Tl; Y = N, P, As, Sb) were examined using first-principles calculations, and we determined that InSb is a Dirac semimetal and TlN and TlP are strong topological insulators [2]. The remaining 15 are semiconductors. The effects of tensile and compressive strains on the electronic structures were also studied. These materials exhibit diverse topological orders. Semiconducting band gaps are primarily found between the bonding and antibonding states of the mixed X(p)-Y(p) orbitals at the top of the valence band and bottom of the conduction band. The topological insulator is explained based on the degenerate p_x–p_y orbitals and their orbital energies relative to the p_z orbitals near the Fermi energy. The nontrivial band topologies of TlN and TlP were confirmed by calculating the Z_2 (1;000) index, surface states, and Wilson loop calculations. The bands split into two branches by including spin-orbit interactions. The results demonstrate that haeckelite compounds are fascinating materials with broad potential applications in optoelectronics, and possess the possibility of hosting emergent physical phenomena.

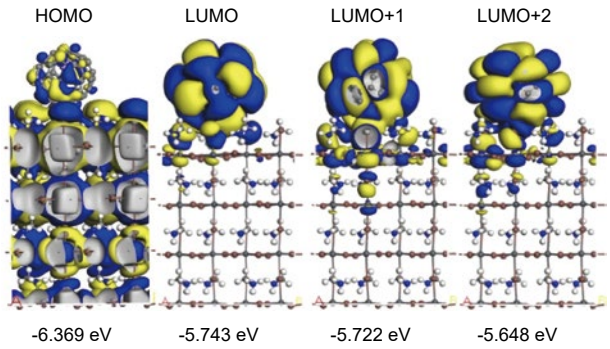

Fig.1 Molecular orbitals of $CH_3NH_3PbI_3/Li^+@C_{60}$.

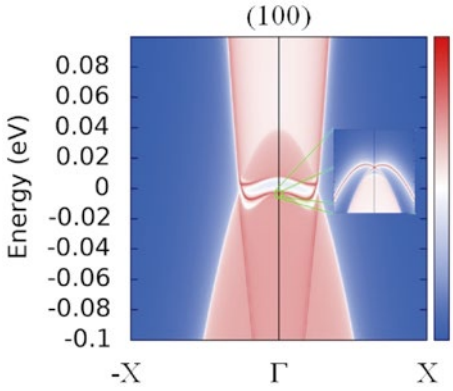

Fig.2 Energy band of TlN at the (100) surface.

References

[1] K.-H. Chew, R. Kuwahara, and K. Ohno, Mater. Adv. **3**, 290 (2022); and see the references therein.

[2] M. Khazaei, A. Ranjbar, Y.-G. Kang, Y. Liang, R. Khaledialidusti, S. Bae, H. Raebiger, V. Wang, M. J. Han, H. Mizoguchi, M. S. Bahramy, T. D. Kühne, R. V. Belosludov, K. Ohno, and H. Hosono, Adv. Functional Mater. **32**, 2110930 (2022).

Kaoru Ohno (Corresponding Author, Yokohama National University)
E-mail: ohno@ynu.ac.jp
Momoji Kubo (Head of Center for Computational Materials Science)
E-mail: momoji@tohoku.ac.jp
URL: http://www.sc.imr.tohoku.ac.jp/eng/

Interplay Among Spin, Charge, and Lattice Dynamics in Superconducting $La_{2-x}Sr_xCuO_4$

Center of Neutron Science for Advanced Materials

To clarify the origin of anomalous intensity enhancement of spin excitations in $La_{2-x}Sr_xCuO_4$ (LSCO), we examined the spin excitations in a series of LSCO compounds with x = 0, 0.075, 0.18, and 0.30, as well as in $La_{5/3}Sr_{1/3}CuO_4$. The intensity enhancement was observed only in the superconducting samples at low temperatures, suggesting an interplay between the spin, charge, and lattice dynamics.

In recent research on strongly correlated electron systems, the intertwining of electron degrees of freedom such as charge, spin, lattice, and orbital have been intensively investigated from the perspective of a new function. In particular, cuprate high-temperature superconductors are critical as model materials for doped Mott insulators, where the intertwining of electron degrees of freedom causes a variety of quantum phases. In a typical hole-doped superconducting (SC) system, i.e., $La_{2-x}Sr_xCuO_4$, the shape of magnetic excitations in the energy(ω)–momentum($\boldsymbol{Q}$) space changes to an hourglass-shaped one upon doping. Studies reported that the intensity of magnetic excitations is enhanced at particular ω and $\boldsymbol{Q}$ positions, where the phonon branches intersect. However, the origin of intensity enhancement has not been clarified.

Therefore, we performed inelastic neutron scattering measurements on $La_{2-x}Sr_xCuO_4$ with x = 0, 0.075, 0.15, and 0.30 using 4SEASONS, a time-of-flight chopper spectrometer, installed at the Materials and Life Science Experimental Facility of the Japan Proton Accelerator Research Complex.

As shown in Fig. 1, we observed the intensity enhancement in the SC samples at K ~ 0 and ω ~ 17 meV at 5 K, while such behavior was not seen in non-SC compounds at 200 K [1, 2]. No intensity enhancement was confirmed for the isostructural insulating $La_{2-x}Sr_xNiO_4$ where x = 1/3. Furthermore, we evaluated the enhanced intensity ($\langle M\rangle^2$ (μ_B^2)) in the absolute unit and clarified that $\langle M\rangle^2$ as a function of hole concentration, x, is maximized at x ~ 0.16, where the optimum superconductivity with the highest SC transition temperature appears. These results suggest an intertwin among spin, charge, and lattice dynamics and a connection between such composite dynamics and superconductivity. We considered phonons lying around 17-19 meV and determined that two phonons are associated with the out-of-plane motion of Cu or O atoms, producing a potential for trapping the charge stripes along the Cu–O bond direction. Thus, these phonons could be coupled with charges.

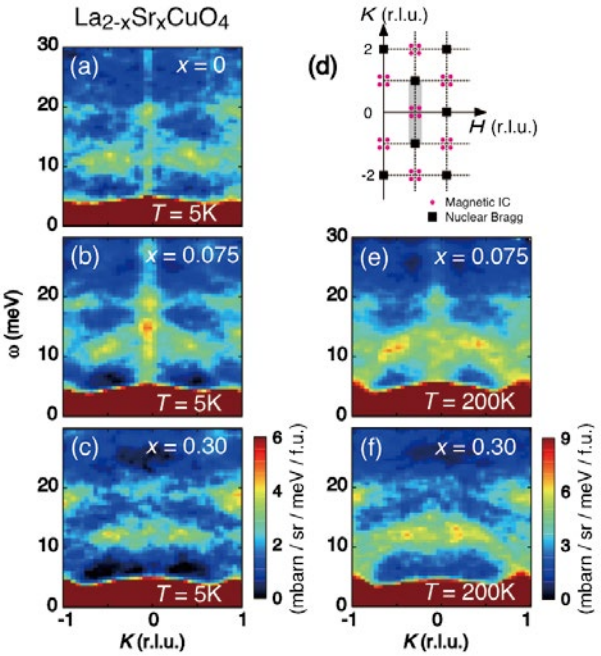

Fig. 1 Dynamical susceptibility in the ω-K plane for $La_{2-x}Sr_xCuO_4$ with (a) x = 0, (b) x = 0.075, (c) x = 0.30 at T = 5 K, (e) x = 0.075, (f) x = 0.30 at T = 200 K. The nuclear Bragg points and incommensurate magnetic positions in the H-K plane are illustrated in (d). The gray area in (d) represents the integrated area in K and range in H of the horizontal axis for intensity maps in (a)-(c), (e), and (f).

References

[1] K. Ikeuchi, S. Wakimoto, M. Fujita, T. Fukuda, R. Kajimoto, and M. Arai, Phys. Rev. B **105**, 014508 (2022).

[2] K. Ikeuchi, S. Wakimoto, M. Fujita, T. Fukuda, R. Kajimoto, and M. Arai, MLF Monthly Report **2**, (2022).

Masaki Fujita (Head of Center of Neutron Science for Advanced Materials)
E-mail: fujita@tohoku.ac.jp
URL: http://nc-imr.imr.tohoku.ac.jp/index-e.html, http://qblab.imr.tohoku.ac.jp

Flexible and Tough Superelastic Co–Cr Alloys for Biomedical Applications

Analytical Research Core for Advanced Materials

Novel body-centered cubic-type single-crystal cobalt-chromium alloys with a Young's modulus close to that of human bone, large recoverable strain of up to 17.0%, superelasticity, high wear resistance, and high corrosion resistance have been developed for potential applications in the biomedical field [1]. Scanning transmission electron microscopy observations revealed that the unique elastic and superelastic behavior of these alloys are related to nanoscale A2/B2 phase decomposition.

Metallic biomaterials are well suited as replacements and supports for damaged hard tissues because of their mechanical properties and high wear resistance. However, these biomaterials must have a low Young's modulus that is close to that of human bone; otherwise, they inevitably cause bone atrophy. Because materials with a low elastic modulus generally have poor wear resistance, simultaneously achieving both low elastic modulus and high wear resistance is difficult. The superelastic properties of shape memory alloys are suitable for biomedical applications, such as vascular stents and guidewires; however, conventional biocompatible shape memory alloys have a low recoverable strain, and an improvement is desired.

In this study, we successfully fabricated large single crystals of novel Co–Cr–Al–Si alloys that were several centimeters in size. The key property of these alloys is that their Young's modulus is significantly low, ranging from 10 to 30 GPa, which is in the range of that of human bones, as shown in Fig. 1. Furthermore, the alloy has a high wear and corrosion resistance similar to that of conventional Co–Cr alloys. It also exhibits superior hot workability. Moreover, the recoverable strain is 17.0% in <001>-oriented single crystals, which is approximately twice that of commercial Ti–Ni shape memory alloys. To clarify the factors responsible for the unique elastic and superelastic behavior of the alloy, transmission electron microscopy (TEM) and scanning TEM (STEM) observations and in situ neutron diffraction measurements obtained during tensile tests confirmed that the crystal structures of the matrix and martensite phases were *B*2 and $L1_0$ types, respectively. Therefore, STEM-energy dispersive X-ray spectroscopy mapping revealed that the matrix phase decomposed into an Al-rich B2 phase and a Cr-rich A2 phase in the order of a few nanometers, as shown in Fig. 2.

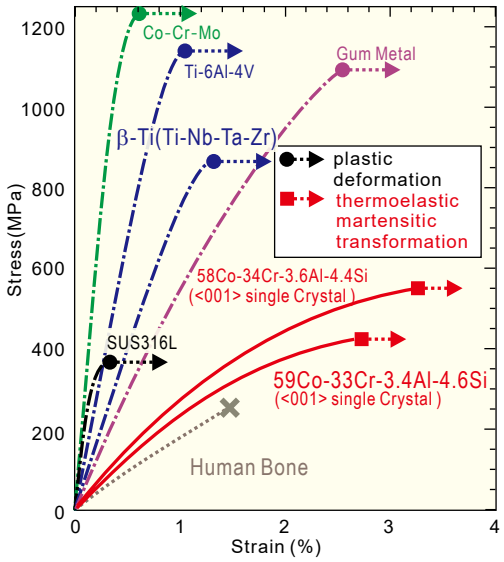

Fig. 1 Elastic properties for Co–Cr–Al–Si alloys and conventional metallic biomaterials.

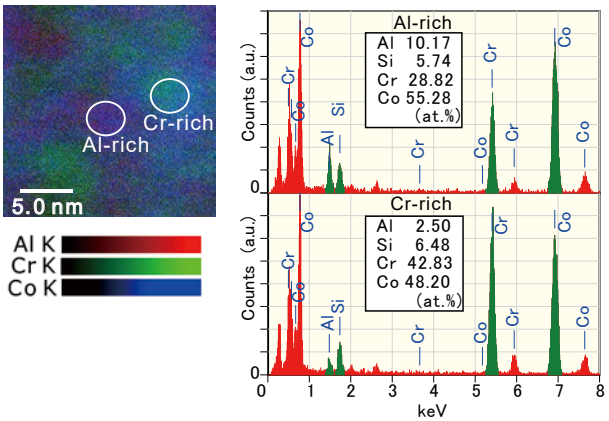

Fig. 2 Energy dispersive X-ray spectroscopy mapping and spectra extracted from the Al- and Cr-rich regions.

References

[1] T. Odaira, S. Xu, K. Hirata, X. Xu, T. Omori, K. Ueki, K. Ueda, T. Narushima, M. Nagasako, S. Harjo, T. Kawasaki, L. Bodnárová, P. Sedlák, H. Seiner, and R. Kainuma, Adv. Mater. **34**, 2202305 (2022).

Makoto Nagasako (Corresponding Author, Analytical Research Core for Advanced Materials)
E-mail: nagasako@tohoku.ac.jp
Eiji Akiyama (Head of Analytical Research Core for Advanced Materials)
E-mail: eiji.akiyama.d1@tohoku.ac.jp
URL: http://www.imr.tohoku.ac.jp/en/about/divisions-and-centers/service-divisions/03.html

Editors

Ryuta Kasada, Yoshinori Onose, Yu Kumagai,
Haruhiko Morito, Goro Miyamoto, and Yusuke Ootani

Editorial Staff

Misa Y. Tomimatsu, Aki Oikawa, and Yuko Godart

Printing

HOKUTO Corporation

Organization

Institute for Materials Research
Tohoku University
2-1-1 Katahira, Aoba-ku, Sendai 980-8577, Japan
Tel. +81-(0)22-215-2144 Fax. +81-(0)22-215-2482

URL: http://www.imr.tohoku.ac.jp/
E-mail: pro-adm.imr@grp.tohoku.ac.jp

© IMR April 2023

The latest issue and back issues of KRH are available here.

東北大学 金属材料研究所
Institute for Materials Research
Tohoku University
2-1-1 Katahira, Aoba-ku
Sendai 980-8577, Japan
http://www.imr.tohoku.ac.jp/

Research